LASER SPECTROSCOPY OF VAN DER WAALS MOLECULES

by

WALTER PETER LAPATOVICH

S.B., Massachusetts Institute of Technology

(1975)

SUBMITTED IN PARTIAL FULFILLMENT OF THE

REQUIREMENTS FOR THE DEGREE CF

DOCTOR OF PHILOSOPHY

at the

MASSACHUSETTS INSTITUTE OF TECHNOLOGY

JUNE 1980

Signature of Author:...'

Department of Physics, May 9, 1980

Certified by:.......

....

Thesis Supervisor

Accepted by:.............

....

Chairman, Departmental Committee on
Graduate Studies

LASER SPECTROSCOPY OF VAN DER WAALS MOLECULES

by

WALTER PETER LAPATOVICH

Submitted to the Department of Physics on
May 9, 1980, in partial fulfillment of the
requirements for the degree of Doctor of
Philosophy.

ABSTRACT

Stable ground state van der Waals molecules (NaNe and NaAr), bound by 1meV and 5meV respectively, are produced in a supersonic molecular beam. The molecular beam is excited by a cw tunable dye laser. As the laser is tuned in frequency the molecular laser induced fluorescence is recorded as a function of laser frequency. Both $A^2\Pi_r - X^2\Sigma^+$ and $B^2\Sigma^+ - X^2\Sigma^+$ manifold are observed in both NaNe and NaAr. The spectra are analyzed by traditional and novel techniques, described fully in the text. Values for molecular constants and potential energy parameters are deduced from the analysis and tabulated.

Supervisor: David E. Pritchard

Title: Professor of Physics

To my unselfish and loving parents,
who encouraged and supported my
pursuits, and in their demise taught
me much about life.

TABLE OF CONTENTS

6

When one tugs at a single thing

in nature, he finds it attached

to the rest of the world.

                        - John Muir

CHAPTER I

INTRODUCTION

A. SURVEY OF INTEREST AND PROBLEM STATEMENT

Collisional and radiative processes involving ground and excited state alkali and rare gas atoms have been studied extensively. Experimentally these systems are attractive because the rare gases are chemically inert and easy to handle, and the readily available alkalis have substantial vapor pressures and, most importantly, exhibit optical transitions accessible via tunable lasers. Further, theoretical interest has been high because the two atoms are well understood - the alkali being hydrogenic, and the rare gas having closed shells - in principle simplifying calculations.

Interest in rare gas alkali systems began with early optical pumping experiments on hyperfine levels in alkali metals. An inert gas, used to reduce the Doppler width, caused a shift in the frequency of the ground state hyperfine transition (ARD 58, MAR 59). Frequency shifts and broadening of optical lines in the alkali metal spectra, taken in the presence of rare gases, have been reported (YSG 75, CGL 80, GIC 69, MCF 76). Measurements of the total and differential cross section for ground and excited state sodium atoms scattering from noble gases have been performed

(DUG 79, CPK 75). Various other fine structure changing experiments (GAS 76, APP 76, PGK 77) and fluorescence depolarization studies have been conducted (EHM 75, WAP 80), where inert gases were used as alkali collision partners.

It is widely realized that the most economical theoretical description of processes like these is based on the molecular potential for the associated atomic pair, that is to say on the integral of the interatomic forces. Unfortunately, these potentials have not in general been known with sufficient accuracy to remove them as a source of considerable uncertainty in theoretical predictions of such processes. Consequently, many of these experiments have not served as a check of theories of the relevant interatomic processes, but rather as inadequate measurements of the potential. This has often led to incorrect deductions about the potentials because it is difficult to judge the sensitivity of the measurements to variations of different parts of the potential.

The worst consequence of the lack of accurate potentials is that it has not been possible to subject some theories of interatomic processes (particularly those of line broadening) to sharp confrontation with experiment. In other cases qualitative understanding of a new physical processes has been slowed by controversy over the

potentials; for example recognition that rapid oscillations in the Na* - Na differential cross section, arising from rotation - electronic induced Σ - Π interference took five years (MPR 79).

The definitive way to establish the molecular potentials is to perform spectroscopic studies on the molecular states arising from the alkali-rare gas interaction. Because the van der Waals binding is weak, these states support few bound levels. Spectra obtained is analyzed and converted into RKR potentials or model potentials which reproduce the experimental observations. In both NaNe and NaAr such high resolution spectroscopy experiments have been performed (LAG 80, ALP 77, SAL 77) which yield information on portions of the potentials with errors less than 1 cm^{-1}. This is a welcome reduction from the 100% (MPV 78) to 1000% discrepancies (PAS 74, BAY 69) of just a few years ago.

Some knowledge of the interatomic potentials, and the fact that spectroscopy can be performed on these systems, foments further interest in these van der Waals molecules. For example, because of the deep well predicted in the NaHe excited state and completely repulsive ground state (HMV 79), one should be able to see free-bound absorption in this system as observed recently in Sr_2 (BEL 80). Also, because of the generally repulsive character of the ground state,

12

alkali-rare gas systems may hold promise as excimer laser systems (TMB 76). These investigations will be left for furture work.

B. SCOPE OF THIS WORK

This work is essentially a synopsis of the latest developments in the NaNe system, and a description and analysis of new work done on the NaAr system.

In Chapter II, the physical origin of the van der Waals binding is outlined from classical and quantum mechanical viewpoints. The alkali-rare gas system is presented as a diatomic molecule, and some molecular theory and nomenclature is introduced.

Chapter III describes the experimental apparatus and technique employed to make stable ground state molecules. Experimental details of the laser and frequency reference system operating parameters, and data collection techniques are discussed in detail.

Chapter IV contains a comparison of the spectral features observed in NaNe and NaAr including a description of the bands and line lists. The rotational and long range analyses are treated thoroughly. Fitting of the data to a model Hamiltonian is discussed.

In Chapter V, the deduced molecular constants are tabu-

lated. A comparison between available theoretical and
experimental van der Waals coefficients (strength of force)
is given. A comparison of molecular potentials, theoretical
and experimental, is presented.

CHAPTER II

THEORY

A. SIGNIFICANCE OF THE VAN DER WAALS FORCES

Van der Waals, London, or dispersion forces are respon-
sible for a host of interesting physical phenomena. The
deviation from ideal gas behavior for noble gases, for exam-
ple, arises because the gas molecules are not isolated hard
spheres, but pliable molecules which can exhibit long range
influences upon one another. In the virial expansion

$$(2.1) \quad p = N_o kT \left[\frac{n}{N_o} + \left(\frac{n}{N_o}\right)^2 b_2(T) + \left(\frac{n}{N_o}\right)^3 b_3(T) + \ldots \right]$$

p = pressure

N_o = Avogadro's number

T = temperature [$^\circ$K]

n = density

b_i = expansion coefficients

the expansion coefficients are defined by the so called
cluster integrals b_2, b_3, etc. (PAT 72).

$$(2.2) \quad b_2(T) = -2\pi N_o \int_0^\infty \left[\exp\left(-\frac{V(R)}{kT} - 1 \right) \right] R^2 dR$$

$V(R)$ = intermolecular potential

R = intermolecular distance

Evaluation of the first of these integrals (Eq.2.2) requires detailed knowledge about the long range intermolecular potential, V(R).

Cluster formation is the precursor of macroscopic condensation and solidification - processes initially dominated by van der Waals attraction, at least in rare gases (PAU 64). These long range forces also play an important role in the adsorption of neutral molecules onto surfaces (MAK 69).

However, these many body precesses are quite complicated, and much can be learned about long range forces by examining simpler systems. Diatomic molecules bound by van der Waals interaction offer such simplicity.

B. THE NATURE OF THE VAN DER WAALS BOND

The van der Waals bonding between two neutral atoms arises because the atoms are polarizable (see Table II.1). The electron cloud surrounding the nucleus of an atom is distorted in the presence of an applied electric field. This distortion is equivalent to a charge separation or polarization of the atom, see Fig.b.1. The electric field may be constant or varying in time.

In the case of an alkali-rare gas diatomic, the alkali atom has only one valence electron which orbits a closed core. The electron is localized somewhere in space at every
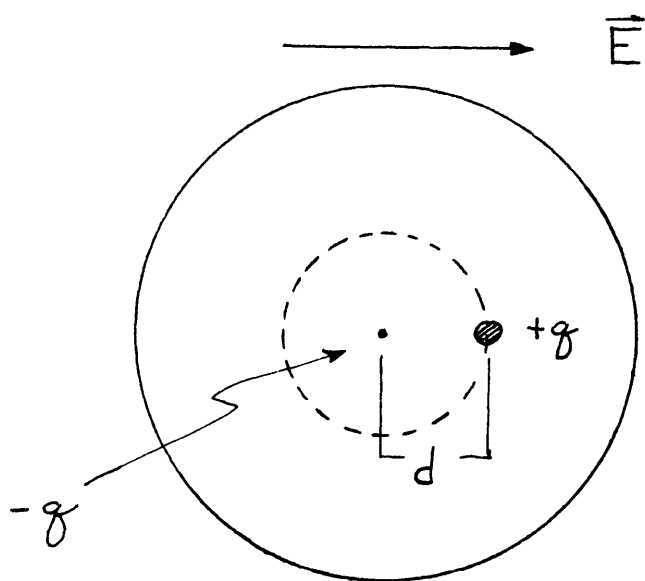
Figure b.1. Polarization of an atom in an applied field.
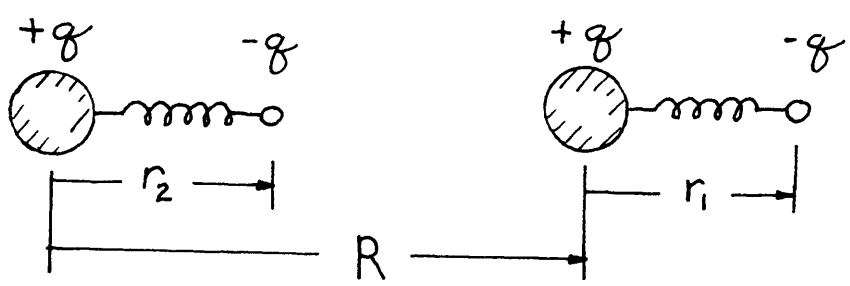
Figure b.2. Two interacting oscillators.

17

instant, giving the alkali an instantaneous dipole moment.
(The moment changes direction from instant to instant, hence
averaging over time yields no net dipole moment, as
expected). This fluctuating dipole moment produces a field
which polarizes the rare gas atom, inducing in it some fluc-
tuating moment as well. The fluctuating dipole moments, if
properly correlated in phase, give rise to an overall lower-
ing of the system energy, i.e. bonding of the alkali and
rare gas (in this case Na with Ne or Ar).

A simple, classical calculation demonstrating this
bonding is carried out in detail in Appendix A. The
interaction lowers the energyof the system as

$$(2.3) \qquad V(R) = - \frac{\alpha_1 \alpha_2 \hbar \omega_0}{R^6}$$

where $\alpha_1 = \alpha_2 = \alpha$, the polarizability, in this calculation
for identical atoms, R is the internuclear separation, ω_0 is
the resonant frequency of the bound electrons in this model,
and $\hbar$ is Planck's constant. While the physical picture
presented is simple, it yields some interesting features:
the interaction is predicted to vary as R^{-6} - a hallmark of
van der Waals attraction, and V(R) varies as the product of
the atomic polarizabilities (here as α^2 for idential atoms).

Quantum mechanical calculations of the dispersion

energy of two ground state atoms have done in detail (MAK 69, SCH 55, PRI 78) and are summarized here.

Two non-interacting atoms separated by a large distance, $R \to \infty$, each have a Hamiltonian of the form,

$$(2.4) \qquad H_A = - \frac{\hbar^2}{2m} \sum_i \nabla_i^2 - Z_A e^2 \sum_i \frac{1}{r_i} + e^2 \sum_{i>j} \frac{1}{r_{ij}}$$

and a set of unperturbed wave functions $|A\rangle$. Here the motion of the nuclei is neglected and the labels A, a and G, g refers to the alkali and rare gas respectively. As the two atoms are moved closer together (R decreases) the Hamiltonian for the system becomes

$$(2.5) \qquad H = H_o + V(R)$$

where H_o is a sum of terms like Eq.(2.4), and $V(R)$ is the perturbation or interaction potential due to the mutually induced multipoles in the atoms. If only dipole-dipole interactions (dominant in alkali-rare gas systems) are considered, and at least one atom is in an S state, $V(R)$ may be written (MAK 69),

$$(2.6) \qquad V(R) = \frac{e^2}{R^3} \sum_{ij} (x_i x_j + y_i y_j - 2 z_i z_j)$$

19

Here x_i, etc are electron coordinates realtive to the nucleus.

Because the alkali atom is monovalent only that one electron is considered, $i = A$, the core being tightly bound. Similarly, because it is difficult to excite any of the electrons in the rare gas, only one electron is considered, $j = G$, whose excitation energy is very nearly equal to the ionization energy, $E_{oG} \approx I_G$. The van der Waals operator is written as

$$(2.7) \qquad V(R) = \frac{e^2}{R^3} (x_A x_G + y_A y_G - 2 z_A z_G)$$

Where for example x_A, y_Z, z_A are the alkali electron coordinates measured relative to the alkali nucleus. Similarly x_G, y_G, z_G are measured relative to the rare gas nucleus.

The wave functions for the interacting system are constructed from wave functions of the separated atoms, viz. $|A\rangle$ and $|G\rangle$,

$$(2.8) \qquad |AG\rangle = |A\rangle |G\rangle$$

with the ground state being $|\emptyset\emptyset\rangle$. This product basis need not be antisymmeterized to account for electron exchange because R is taken to be sufficiently large so that electron

clouds have negligible overlap.

The dispersion energy is calculated using standard perturbation theory (SCH 55). The first order energy correction is zero, because the operator, Eq.(3.7), connects states of different parity,

$$(2.9) \quad E^{(1)} = \langle \emptyset\emptyset|V|\emptyset\emptyset\rangle \propto \langle\emptyset|x_A|\emptyset\rangle\langle\emptyset|x_G|\emptyset\rangle + \ldots$$

$$\therefore E^{(1)} = \langle\emptyset\emptyset|V|\emptyset\emptyset\rangle = \emptyset$$

The first non vanishing contribution comes from second order perturbation theory

$$(2.1\emptyset) \quad E^{(2)} = - \sum_{AG} \frac{|\langle GA|V|\emptyset\emptyset\rangle|^2}{E_{oA} + E_{oG}} \neq \emptyset$$

the subscripts oA(oG), eg E_{oA}, indicate the energy difference between the ground ($\emptyset$) and first excited states in the (A) alkali, or (G) rare gas. Inserting the operator V(R) into Eq. (2.1$\emptyset$) yields,

$$(2.11) \quad E^{(2)} = - \frac{3\hbar^4 e^4}{2m^2 R^6} \sum_{AG} \frac{f_{oA} f_{oG}}{E_{oA} E_{oG} (E_{oA} + E_{oG})}$$

where use is made of the oscillator strengths (HIN 67).

21

$$(2.12) \qquad f_{oA} = \frac{2m}{3\hbar^2} E_{oA} \; |<A| \sum_i \vec{r}_i |\emptyset>|^2 \; \cong \; \frac{2m}{\hbar^2} E_{oA} |<A|x_i|\emptyset>|^2$$

Substitution of the oscillator strength in terms of the polarizabilities $\left[f_{oA} = \frac{m}{e^2\hbar^2} \alpha_A E_{oA}^2 \right]$ (MAK 69) into Eq.(2.11) gives

$$(2.13) \qquad E^{(2)} = - \frac{3}{2R^6} \frac{E_{oA}I_G}{E_{oA}+I_G} \alpha_A \alpha_G$$

where the ionization energy has replaced the excitation energy for the rare gas. This result demonstrates the same R^{-6} behavior and dependence on the polarizabilities as derived classically (Eq.2.3). Here the atoms are not identical.

The van der Waals potential energy $V(R) \equiv E^{(2)}$, is often written $V(R) = - C_6/R^6$ implying,

$$(2.14) \qquad C_6 = \frac{3}{2} \alpha_A \alpha_G \frac{E_{oA}I_G}{E_{oA}+I_G}$$

These C_6 coefficients have been calculated for ground state atom interactions (excited state calculations for non symmetric electron distributions being much more difficult, TAT 77, PRS 77), and in particular for the NaNe and NaAr systems. A comparison of these calculated coefficients, estimates based on Eq.(2.14) and Table II-1, and values deduced

from a long range (large R) analysis of the data (see Appendix F and LER 73) is presented in Table IV.7 (Results and Analysis - Chapter IV.)

It must be noted that in the above derivation all higher multipole interactions (dipole-quadrupole, quadrupole-quadrupole, etc.) have been neglected. These interactions are non-negligible for small R, and can be significant for $R \simeq 5\text{Å}$. Including these effects, the "long range" potential is of the form,

$$(2.15) \qquad V(R) = -\frac{C_6}{R^6} - \frac{C_8}{R^8} - \frac{C_{10}}{R^{10}} - \dots$$

The C_8/R^8 and C_{10}/R^{10} terms decrease rapidly as R increases leaving C_6/R^6 as the dominant term. For the case of alkali-rare gases the ratio of C_8/C_6 is given by (MAK 69).

$$(2.16) \qquad \frac{C_8}{C_6} = \frac{15}{4R^2} \left[\frac{I_G \alpha_G (I_G + E_{oA})}{f_G (E_{oA} + 2I_G) e^2} + \frac{E_{oA} \alpha_A (E_{oA} + I_G)}{f_A (2E_{oA} + I_G) e^2} \right]$$

The ratio C_8/C_6 as a function of R has been calculated according to Eq. (2.16), and is displayed graphically in Fig.b.3. The contribution C_{10} is always smaller than C_8 in these systems and is neglected. When the alkali is in an excited state, it is not obvious that the C_8, and C_{10}, terms are small. While no good estimates of C_8 exist for alkali

23
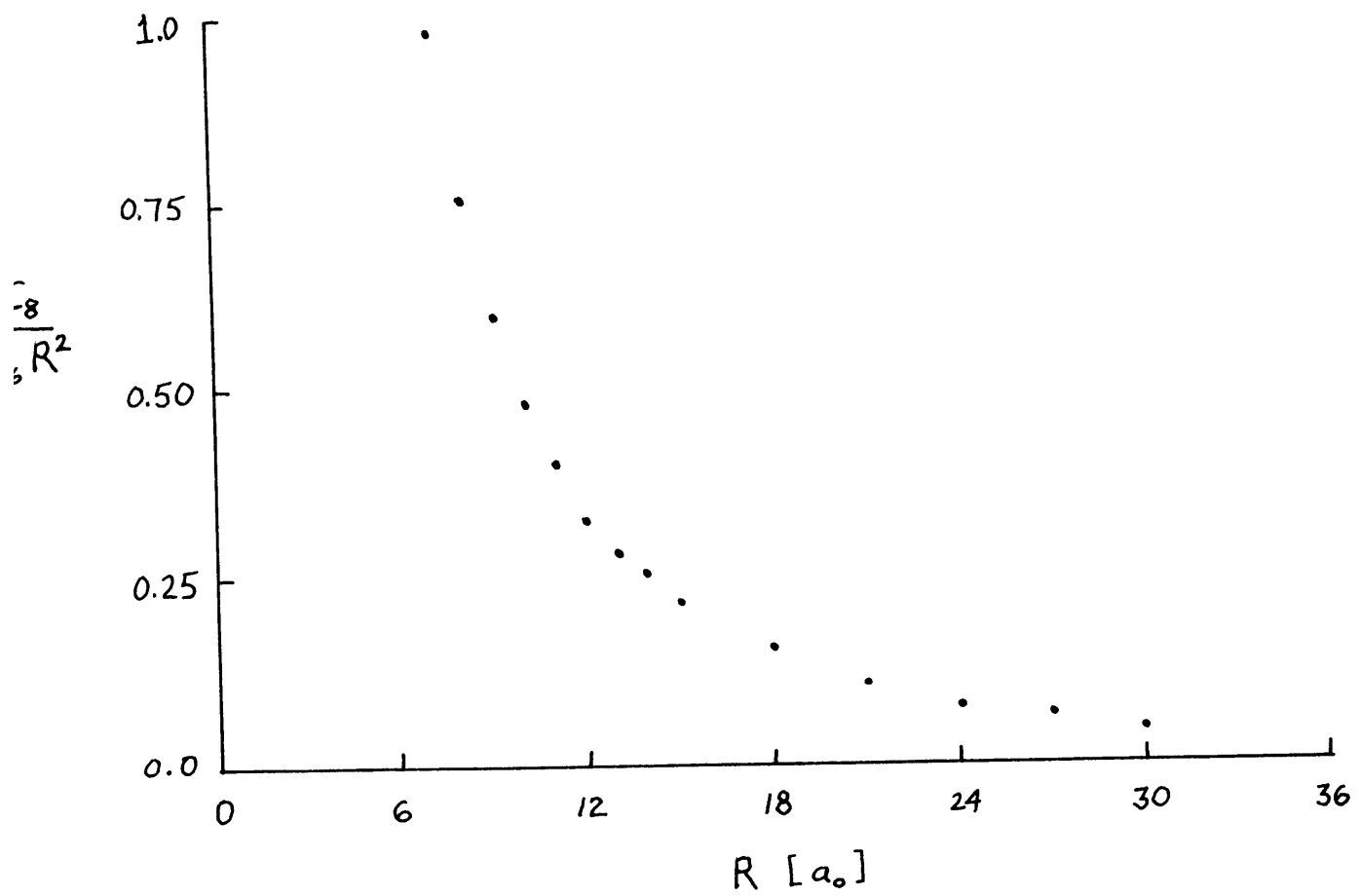
Figure b.3. Graph of C_8/C_6 for NaAr, NaNe.

atoms in the 3P state, calculations for C_8 and C_{10} have been done for alkali-rare gas systems with the alkali in nS states (PRS 77). For Na in the 4S state the ratio, $C_8/C_6R^2 \simeq 2.8$, for R = 10 a_o for both Ne and Ar. Hence we can expect C_8 terms to make some contribution in the present case with Na in the 3P state. The C_{10} terms which have been calculated have uncertainties equal to or larger than the calculated values.

C. NaNe AND NaAr AS DIATOMIC MOLECULES

The Hamiltonian for a diatomic molecule is separable in the Born Oppenheimer approximation (HER 50, HOU 70) and may be written as,

$$(2.17) \qquad H = H_{ev} + H_r + H_{s.o.}$$

H_{ev} is the electronic-vibration part which contains the electronic energy, and the vibrational kinetic and potential energy of the nuclei. Because the nuclei move more slowly than the electrons, they are confined to vibrate within the effective potential, V(R), caused by the electronic motion (B-0 approximation). This potential generally exhibits a minimum and a steep repulsive inner wall (small R) due to electron cloud overlap and nuclear repulsive Coulomb forces

25

(Fig.b.4). In the limit of large R, V(R) is just he long range potential of Eq.(2.15).

$H_{s.o.}$ is the spin orbit operator responsible for atomic fine structure and molecular multiplets, and H_r is the rotational Hamiltonian responsible for rotational fine structure (branches) within each vibrational band.

The theory of diatomic molecules will not be discussed in detail here since it is thoroughly treated in the literature (HER 50, HOU 70, HAR 72, STE 74). The Hamiltonian, Eq.(2.17), is discussed in more detail in Appendix B. However, to understand what follows, it is important to realize that the individual terms in the molecular Hamiltonian give rise to an energy hierarchy, where in general,

$$E_{electronic} > E_{vibrational} \gtrsim E_{spinorbit} \gtrsim E_{rotational}$$

Hyperfine interactions have been omitted because they are small.

For weakly bound van der Waals molecules, prediction of the electronic states from the separated atoms is very simple. The ground state atoms, $^2S(Na)$ and $^1S(Ne)$ or $^1S(Ar)$, give rise to the ground $X^2\Sigma^+$ state (Fig.b.4). This state is rather isolated from other electronic states; consequently,

26
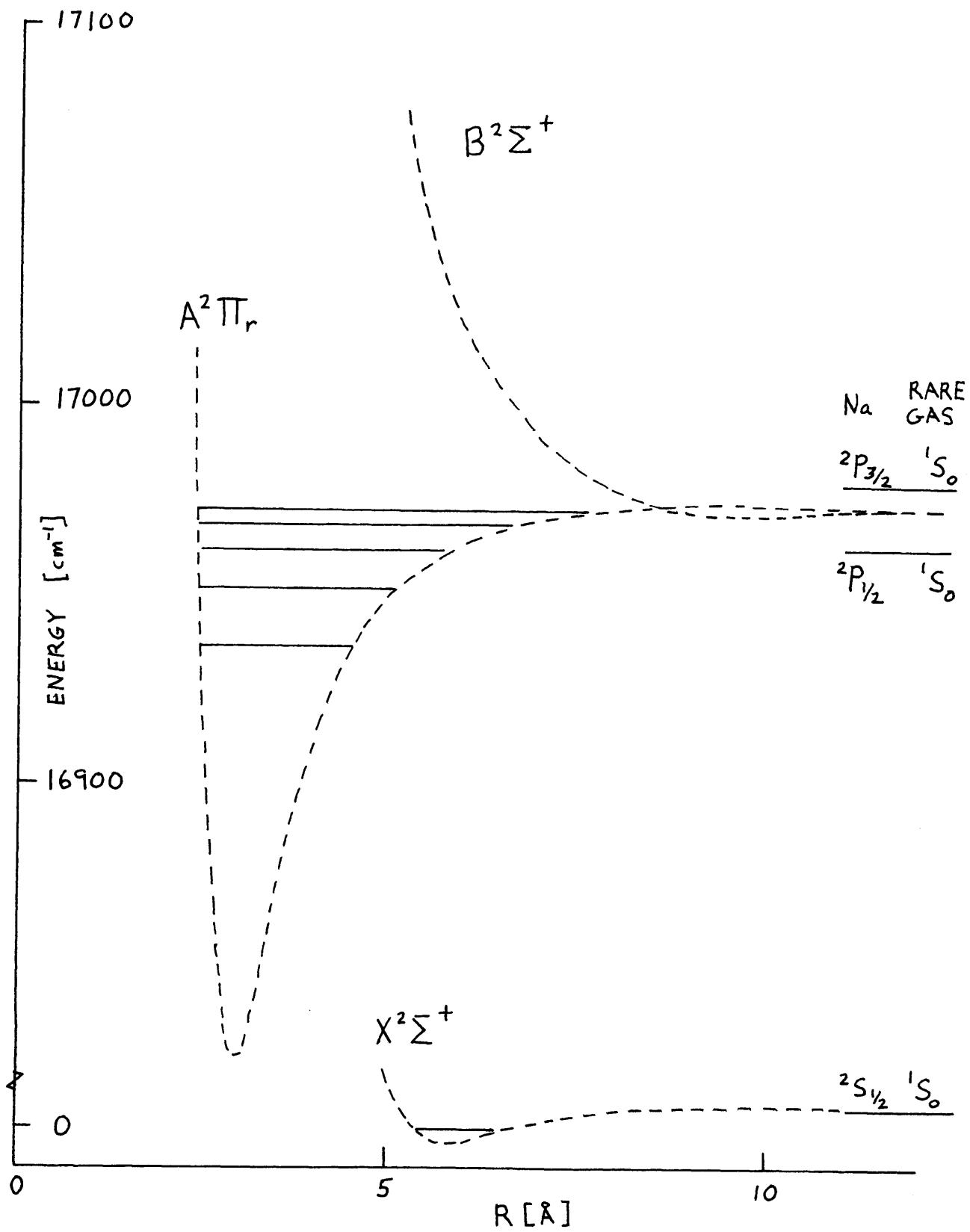
Figure b.4. Correlation of atomic and molecular states.

the spin-rotation interaction, γ, is small.

The atomic hyperfine structure of the sodium atom is carried over to the molecular ground state and couples the nuclear spin $\vec{I}$ to the electron spin $\vec{S}$ to give

$$\vec{G} = \vec{I} + \vec{S}$$

This coupling results in a hyperfine splitting of 1.773 GHz. The resultant vector $\vec{G}$ couples to nuclear rotation $\vec{N} = \vec{J} - \vec{S}$ by the spin-rotation interaction to give the total momentum $\vec{F}$ as

$$\vec{F} = \vec{G} + \vec{N}$$

This coupling is weak and will not cause any further splitting. This particular coupling scheme is denoted as Hund's case b_{β} and has been described in detail elsewhere (DUN 72, FRF 52, TOS 55).

The hyperfine splitting is independent of the rotational quantum number. Since only one hyperfine component need be considered for measurement, and since the hyperfine splitting in the excited state is undetectable within the experimental resolution, and since the ground state spin-rotation interaction is small, the ground state angular

28

momentum coupling may be considered as

$$\vec{J} = \vec{S} + \vec{N}$$

This description is known as Hund's case (b) (HER 50).

From the separated atomic states 3^2P(Na) and ^1S(Ne), two molecular states, $A^2\Pi_r$ and $B^2\Sigma^+$ are formed (Fig.b.4). The $A^2\Pi_r$ states are split by the spin-orbit interaction into $A^2\Pi_{3/2}$ and $A^2\Pi_{1/2}$ multiplets. At large internuclear separation, the multiplets dissociate

$A^2\Pi_{3/2} \rightarrow Ne(^1S_0) + Na(3^2P_{3/2})$ and

$A^2\Pi_{1/2} \rightarrow Ne(^1S_0) + Na(3^2P_{1/2})$. The Π state is formed in the regular configuration, $A^2\Pi_r$, that is the $\Pi_{1/2}$ component lies below the $\Pi_{3/2}$ component. The Π states arise from a linear combination of atomic p orbitals, $|\ell=1, m_\ell = \pm 1, s = 1/2; m_s = \pm 1/2\rangle$, whereas the $B^2\Sigma^+$ state arises from $|\ell = 1, m_\ell = 0, s = 1/2, m_s = \pm 1/2\rangle$. NaNe and NaAr are analyzed using a Hund's case (a) basis, in which both $\vec{L}$ and $\vec{S}$ couple independently to the internuclear axis, with projections Λ, Σ and $\Omega = \Lambda + \Sigma$, being good quantum numbers (HER 50). The expectation value of the spin-orbit operator in the molecular basis $|\Lambda\Sigma S\rangle$ is

$$\langle \Lambda\Sigma S | A\vec{L}\cdot\vec{S} | \Lambda\Sigma S \rangle = A\Lambda\Sigma$$

Since the interaction of the Na and Ne atoms is weak, we expect the atomic orbitals to be largely undistorted in the molecule. The linear combination of atomic orbitals constituting the molecular state is trivial, and we make the identification $|\Lambda=\pm 1, \Sigma=\pm 1/2, S=1/2\rangle = |\ell=1, m_\ell=\pm 1, s=\pm 1/2, m_s=\pm 1/2\rangle$. So in the atomic case

$$\langle \ell m_\ell s m_s | a \vec{\ell} \cdot \vec{s} | \ell m_\ell s m_s \rangle = \lambda \sigma \langle \Pi 3P_{Na} | a | \Pi 3P_{Na} \rangle$$

(λ and σ are projections of the atomic orbital and spin angular momenta on the internuclear axis). Therefore we expect $A = \langle a \rangle = 2/3 \xi(r) = 11.46$ cm^{-1} in the case (a) limit [$\xi(r)$] is the atomic radial spin-orbit integral (COS 35). For high vibrational levels a more atomic like coupling is expected as the spin orbit splitting approaches the Na $3^2P_{3/2} - 3^2P_{1/2}$ interval (17.1963 cm^{-1}).

D. PREDICTIONS OF SPECTRAL FEATURES

The transitions of interest in the van der Waals molecules involve a change of electronic, vibrational, and rotational energy. They are designated "rovibronic" and lie in the optical frequency regime near the atomic sodium D_1 and D_2 lines. This proximity occurs because the electronic excitation corresponds to excitation of the atomic sodium,

$3^2P_{3/2} - 3^2S_{1/2}$ or $3^2P_{1/2} - 3^2S_{1/2}$, whereas the vibrational bands result from energy changes in the molecule which are much smaller than the electronic change in energy, viz. ~ 10 cm^{-1}: $17,000$ cm^{-1}. Consequently, the vibrational bands appear to be clustered within roughly the excited state dissociation energy of the molecule (a few hundred cm^{-1}) of the atomic resonance lines.

Because of the negligible spin-rotation splitting in the ground state, each spin multiplet, $A^2\Pi_{1/2} - X^2\Sigma^+$ or $A^2\Pi_{3/2} - X^2\Sigma^+$, vibrational band consists of four branches. These are labelled in the notation of Kopp and Hougen (KOH 67) and Brown et al. (BRO 75) as R^e, $R^f + Q^{fe}$, $Q^{ef} + P^e$, and P^f (see Fig.b.5). Levels with half integral rotational quantum numbers are designated 'e' levels if their parity (with respect to reflection of all coordinates in a plane containing the internuclear axis) is $+(-1)^{J-0.5}$, and 'f' levels if their parity is $-(-1)^{J-0.5}$. The R^e (R^f) transitions are $\Delta J = J'-J'' = +1$ transitions between levels e - e (f - f). Q^{fe} and Q^{ef} are $\Delta J = 0$ transitions between opposite parity levels. The notation $R^f + Q^{fe}$ indicates that these branches overlap and will be unresolved, although often one branch is expected to dominate in intensity. The $B^2\Sigma^+ - X^2\Sigma^+$ vibrational bands also exhibit four rotational branches (see Fig.b.6). Both $A^2\Pi_{1/2}$

Figure b.5. $A^2\Pi_r - X^2\Sigma^+$
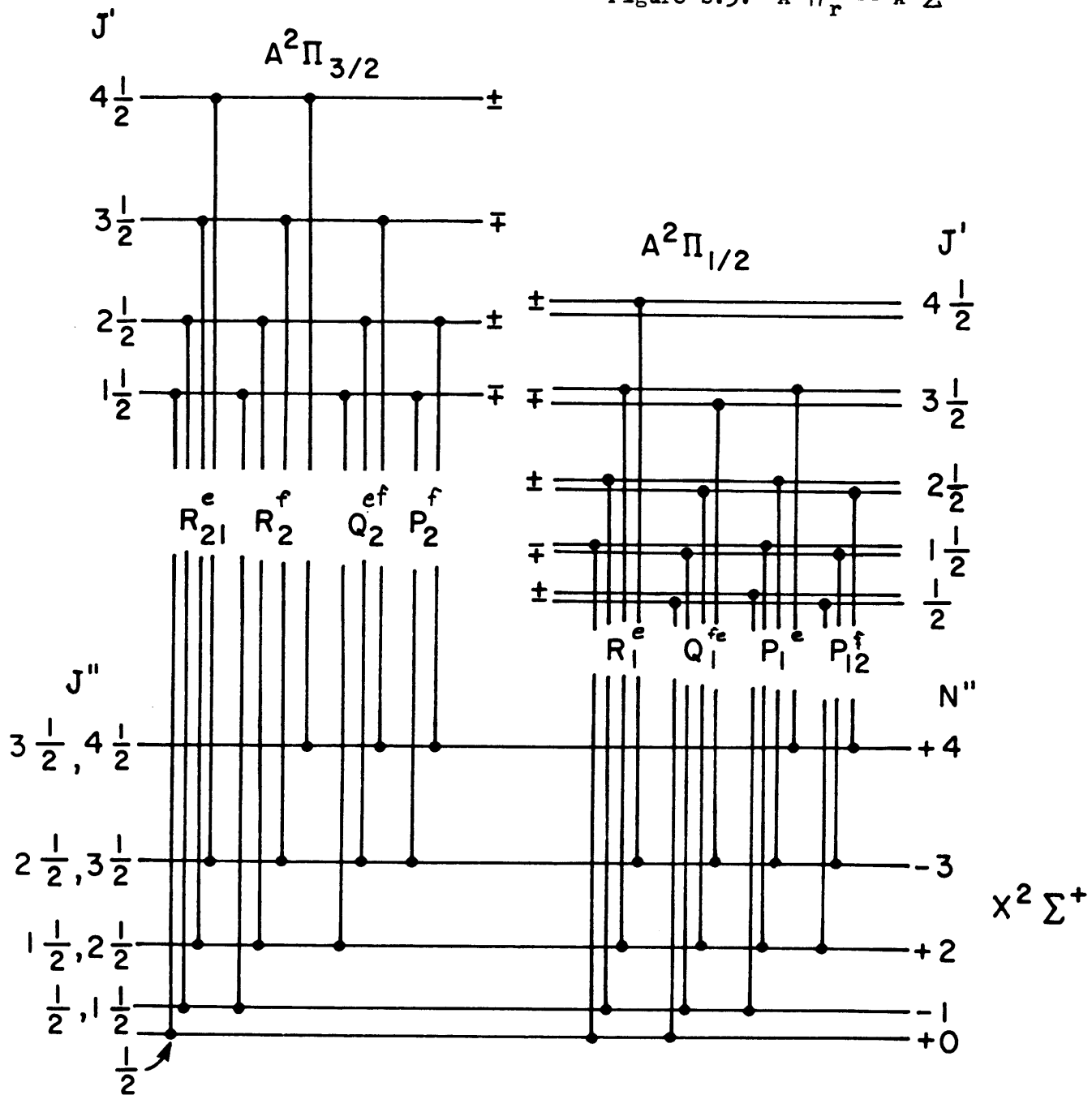
Figure b.6. $B^2\Sigma^+ - X^2\Sigma^+$
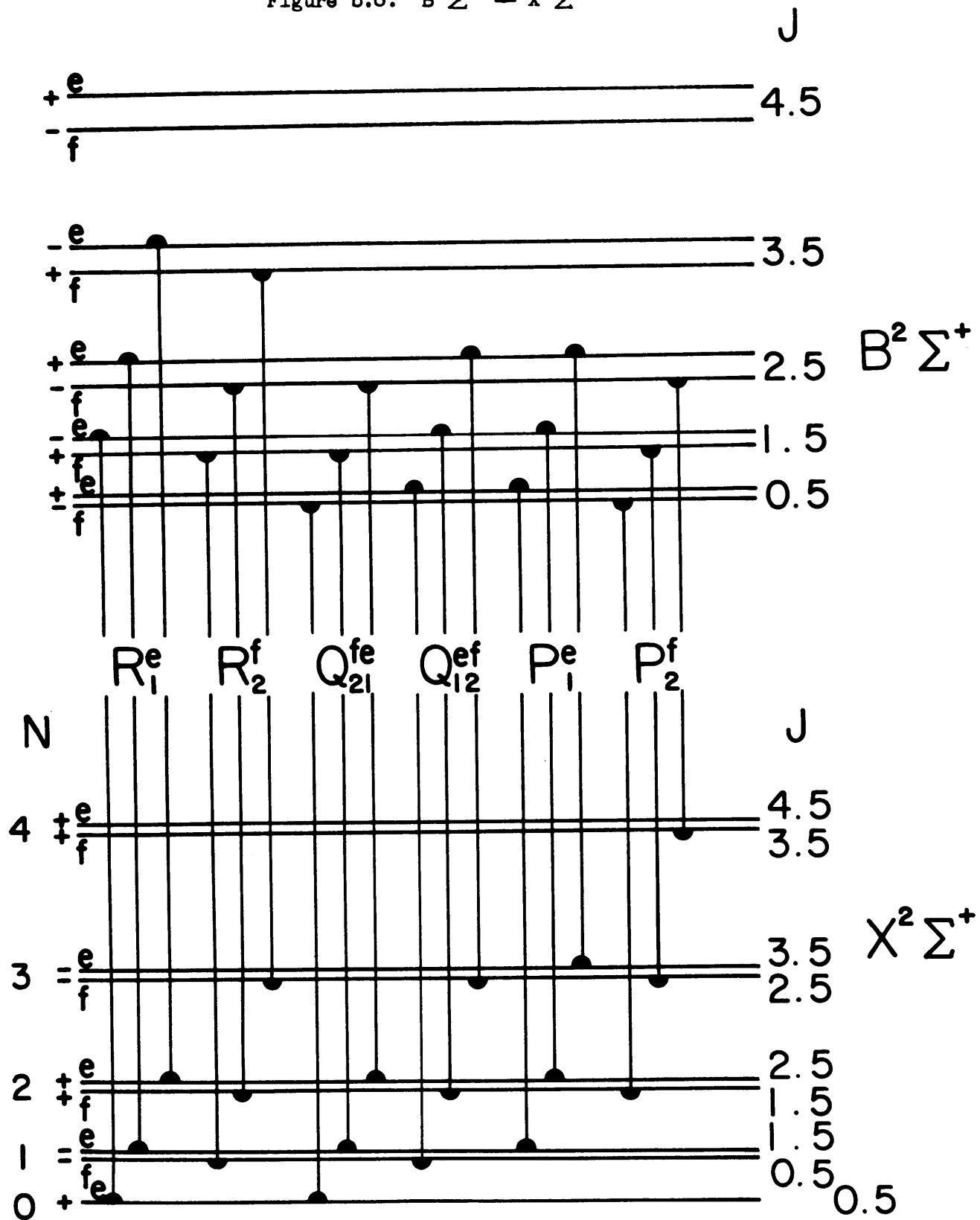
- $X^2\Sigma^+$ and $B^2\Sigma^+$ - $X^2\Sigma^+$ are distinguishable from

$A^2\Pi_{3/2}$ - $X^2\Sigma^+$ by the presence of three extra lines:

$Q^{fe}(\emptyset.5)$, $Q^{ef}(\emptyset.5)$, and $P^f(1.5)$.

Figure b.7 is a computer generated plot for

$A^2\Pi_{3/2}$ - $X^2\Sigma^+(14,\emptyset)$ in NaAr. The molecular constants have

been estimated, and the relative intensities calculated

according to Earls (EAR 35). This plot is intended only to

illustrate the four branches discussed above and to show the

patterns which develop in a vibronic band. These patterns

serve as a useful guide in the analysis of the spectra.

Figure b.7. Calculated spectrum.

$$Na\,Ar$$
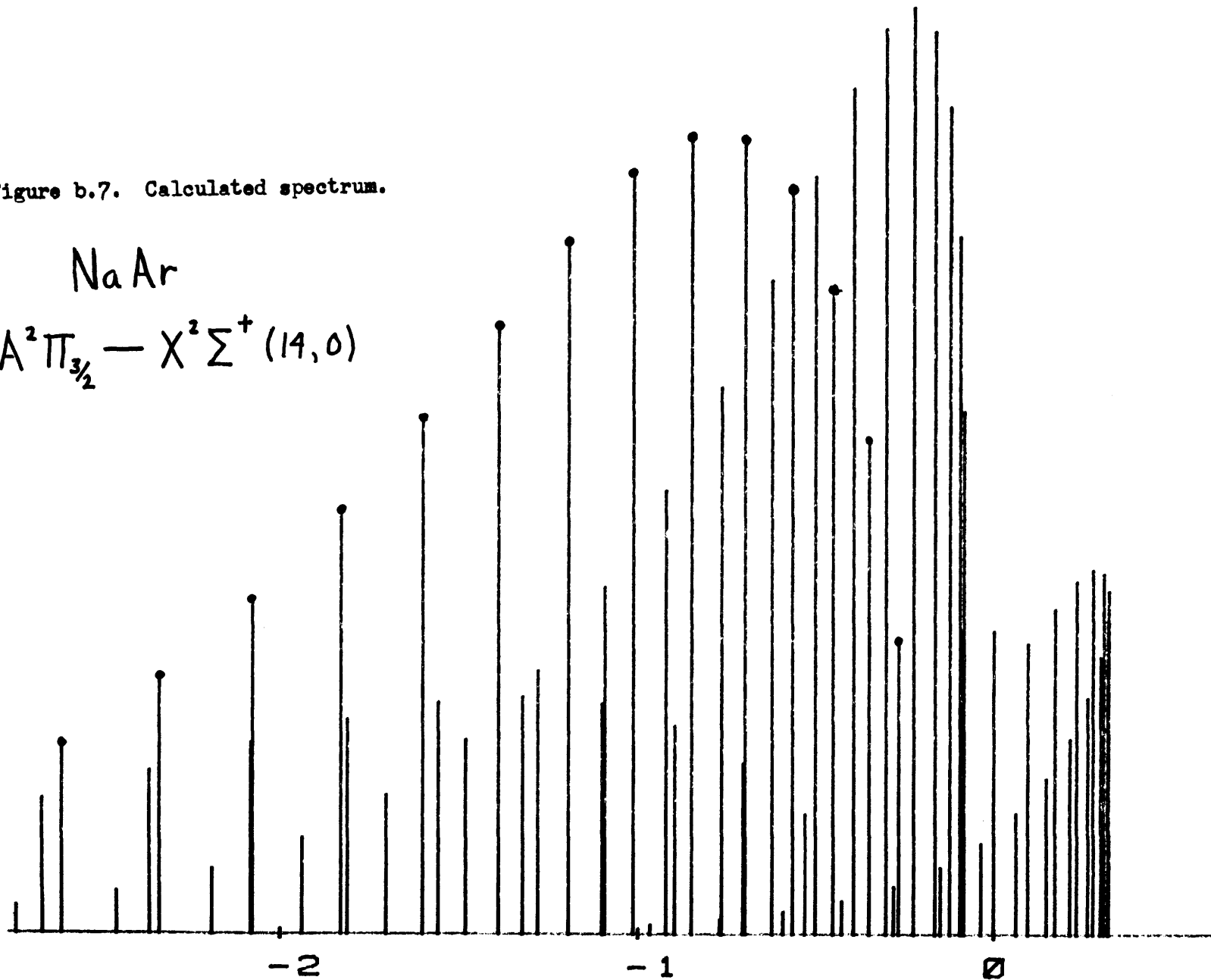
$$A^2\Pi_{3/2} - X^2\Sigma^+ (14,0)$$

(IN CM-1)

$$B'' = 0.04440 \qquad B' = 0.03640 \qquad T_r = 5\,K$$

CHAPTER III

EXPERIMENTAL

A. THE MOLECULAR BEAM TECHNIQUE

The molecular beam method is attractive for studying van der Waals molecules because it permits the formation of stable ground state molecules. The ground state binding energy of these molecules is so small ($\sim$8K) for NaNe and $\sim$50K for NaAr that conventional techniques, cells for example, are not viable. Collisions of buffer gas atoms with any van der Waals molecules which might form in a cell at room temperature ($\sim$300K) would disintegrate the species of interest. Further, cooling a mixture of alkali and rare gas in a conventional cell to a few degrees Kelvin is not an acceptable technique, as both gas and alkali would condense onto the cell's walls, leaving nothing to react in the gas phase. Molecular beams provide a solution to the formation problem in a rapidly moving (AAF 66, FED 66) highly directional (LEO 64, RVS 71) gas phase system with substantial cooling in all degrees of freedom (AAF 65, ANF 65, BPP 71) conducive to the formation of weakly bound molecules (SAF 77, ALP 77, SWL 75, KFW 78).

The molecular beam is produced by entraining small amounts of sodium vapor in a high pressure, rare gas helium
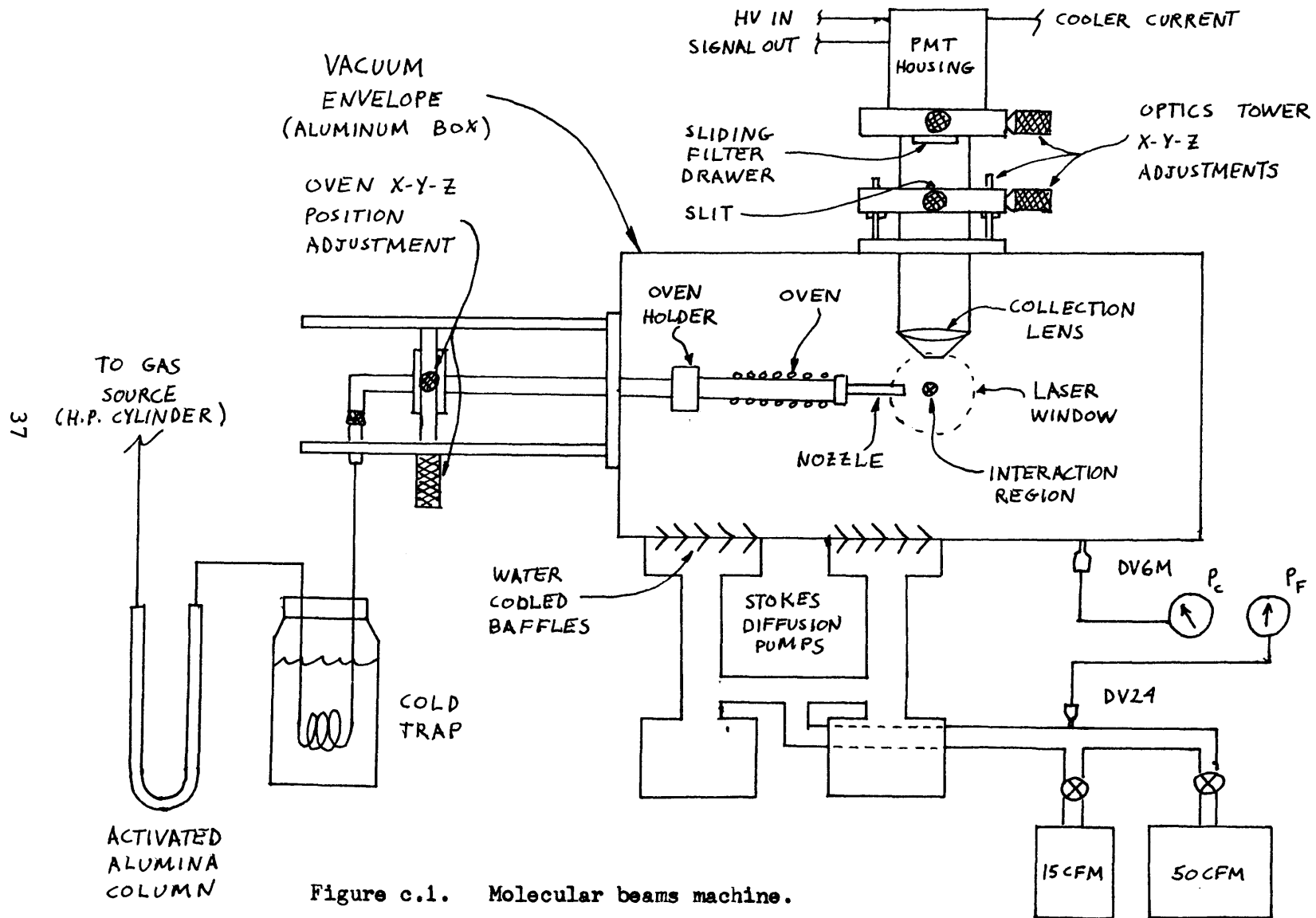
Figure c.1.   Molecular beams machine.

37

INTENSITY AND FREQUENCY CONTROL SYSTEM

AR-ION LASER

DYE LASER

FREQUENCY REFERENCE SYSTEM

CHART RECORDER

Y

OPTICAL BAFFLES

BAFFLE (SLIT)

PHOTOMULTIPLIER

MOLECULAR BEAM (OUT OF PAGE)
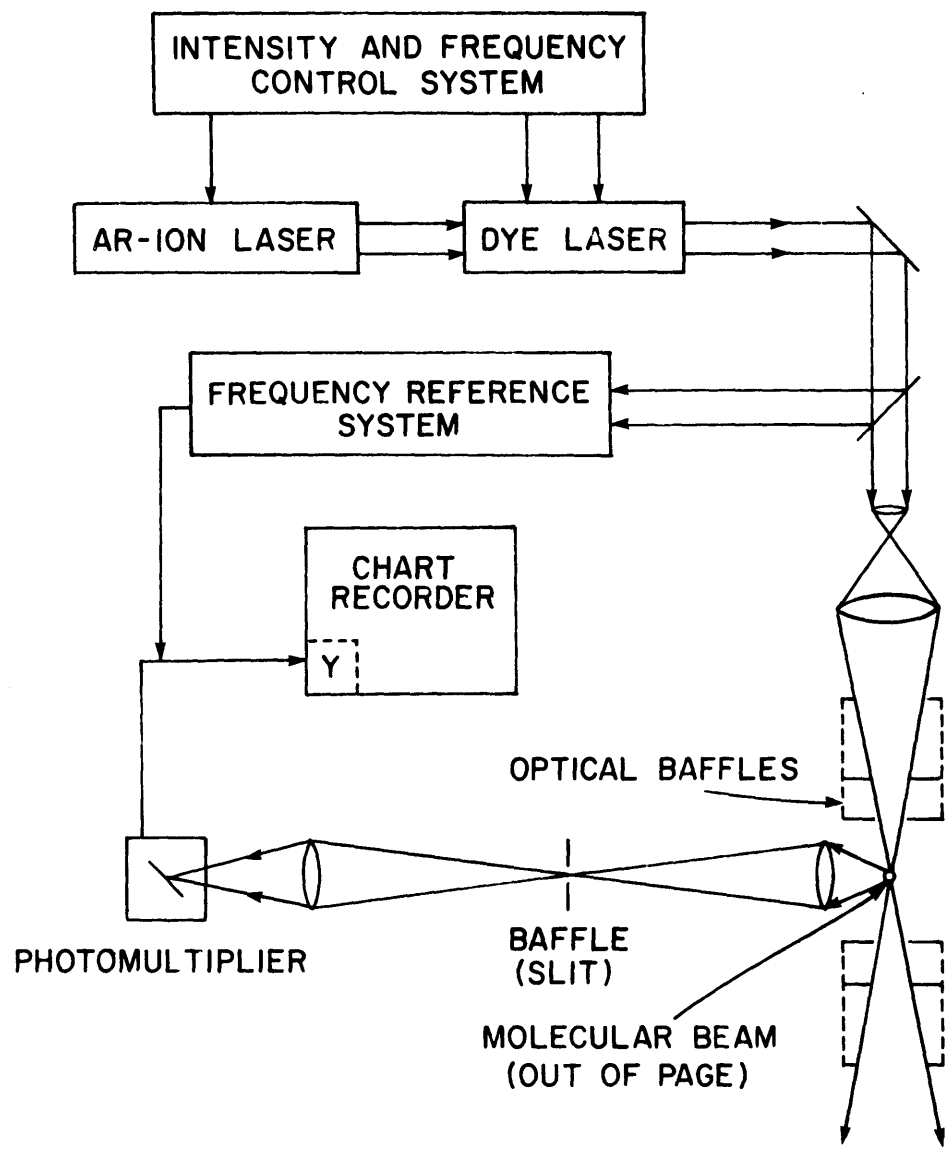
Figure c.2. Schematic of laser system.

38

blend and allowing the mixture to expand adiabatically through a small nozzle into a vacuum (CAM 7Ø). The vacuum is maintained by two Stokes 4" "Ring Jet" booster pumps backed by a 5ØCFM and a 15CFM forepump connected in parallel (see Fig. C.1 and C.2).

As the gas expands into the vacuum chamber the density decreases giving rise to three regions in the beam core (see Fig. C.3). Near the nozzle, where the density is highest, tertiary collisions are dominant allowing alkali and rare gas atoms to bond and form van der Waals molecules. Further downstream binary collisions are dominant and cool the molecules. Finally, as the density drops still lower, no further cooling occurs and the molecules enter a zone of free flow. This is the region (a few mm from the nozzle) where the laser beam probes the molecular beam.

The entire core of the expansion is isolated from collisions with background gas atoms by a shock wave (BIH 63, CAM 66 and see Fig. C.3). This screens the van der Waals molecules from collision much like the water emerging from a fire hose prevents a ping pong ball from penetrating into the core of the flow. This isolating effect, and probing the molecular beam in the free flow region, eliminates collisional broadening of spectral lines.

Cooling in these expansions limits the population to
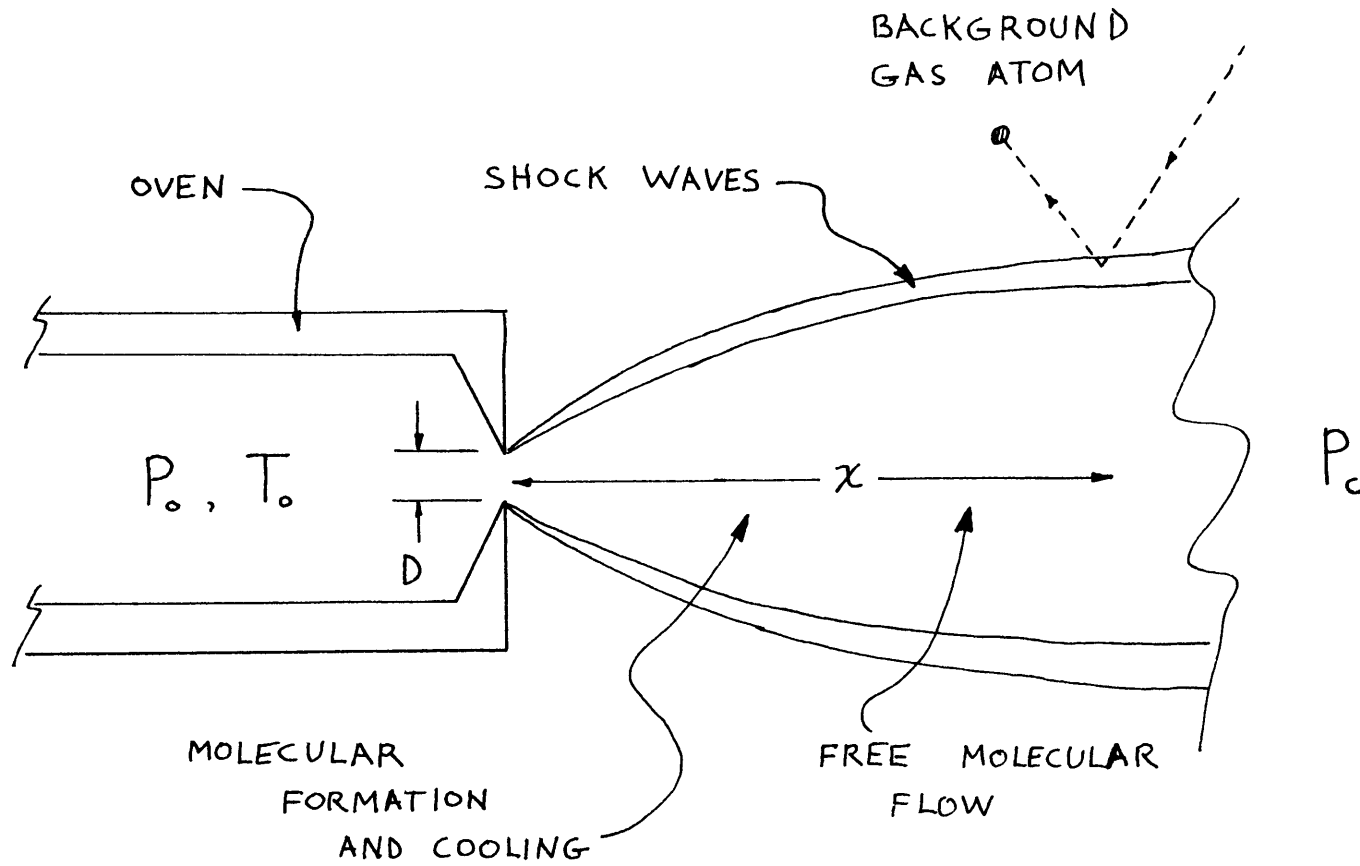
Figure c.3. Supersonic expansion into vacuum.

low vibration rotation states in the ground electronic state, simplifying the absorption spectra. The cooling process has been studied extensively (VAW 59, CAM 66, AAF 65, GAF 74, SWL 75). The various degrees of freedom (rotational, vibrational, translational) cool, via collisions, until a terminal temperature, T_t, is achieved,

$$(3-1) \qquad \frac{T_t}{T_o} = [1 + (\gamma-1)M^2/2]^{-1}$$

where T_t is the translational temperature (defined by 1/e points in the velocity distribution), T_o is the oven temperature, $\gamma = C_p/C_v$, the ratio of specific heats, and M is the Mach number in the expansion. The degrees of freedom cool at different rates depending on their energy transfer cross sections. The rotational degree cools fastest so that a laser probing the beam at a fixed distance away from the nozzle reveals $T_{trans} < T_{rotation} < T_{vibration}$. In these experiments, we have observed rotational temperatures, T_r, (as determined from the J distribution) of $T_r \simeq 1.7K$ in NaNe and $T_r \simeq 2.9K$ in NaAr for Mach numbers of ~ 30. From the Na_2 spectra serendipitiously acquired at the same time, a rotational temperature $T_r \simeq 19(4)K$ is deduced as well as a vibrational temperature $T_v \simeq 140(7)K$ for the dimers.

The molecular beam is an optically thin source of van

der Waals molecules. A traditional absorption experiment on such a source has inherently poor signal to noise since the absorption is measured relative to a largely unattenuated d.c. background. However, by measuring the absorption in the molecular source, indirectly, via the laser induced fluorescence, substantial improvements in signal to noise are realized (see Fig. C.4).

In these experiments the supersonic molecular beam intersects a tunable dye laser beam at 90°. The molecular fluorescence which occurs as the laser is tuned in frequency is collected perpendicular to both laser and molecular beams. Since the laser beam is highly directional, this collection geometry limits the background laser light to that which is scattered from the source nozzle (~ 100 counts). The molecular fluorescence is emitted isotropically so only a small fraction ($\sim 8\%$) is collected in this scheme.

Sub-Doppler spectroscopy can be performed in a molecular beam because the beam is essentially collisionless, and almost monoenergetic ($\sim 7\%$ velocity spread BIH 63). A first order Doppler free region is attained by passing a converging laser beam approximately 5 mm in front of the nozzle and focussing it several mm beyond the axis of the molecular beam. The rays of the laser beam are perpendicular to

FLUORESCENCE DETECTOR

I_2

LENS

LASER BEAM

I_0, ν

I_1

OPTICALLY RARE
MOLECULAR SOURCE

ABSORPTION
DETECTOR

I_1

ν

I_2

ν
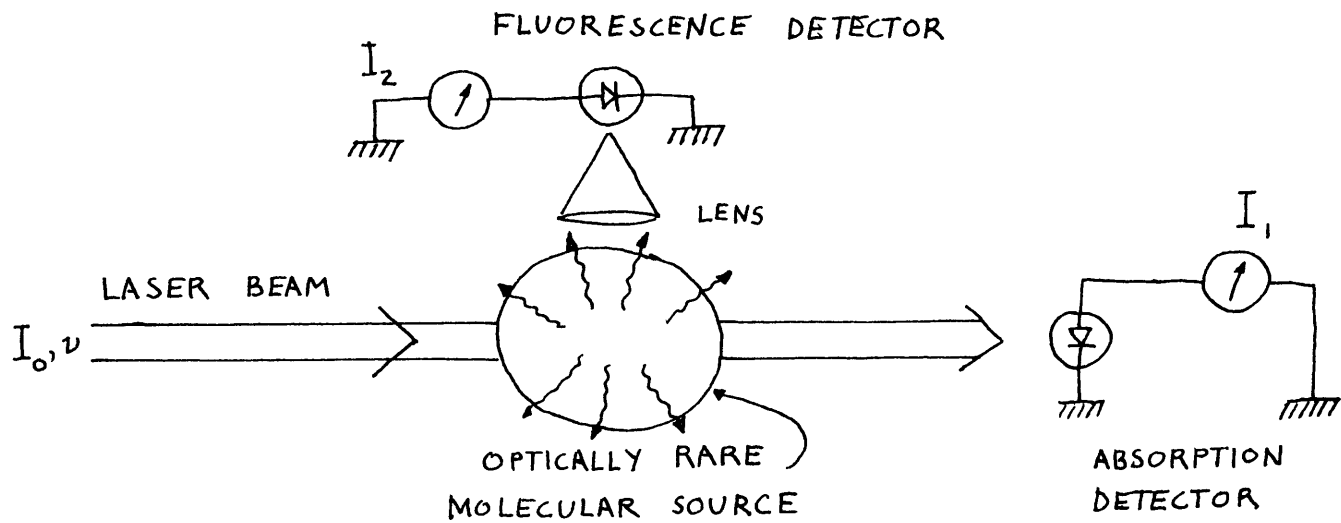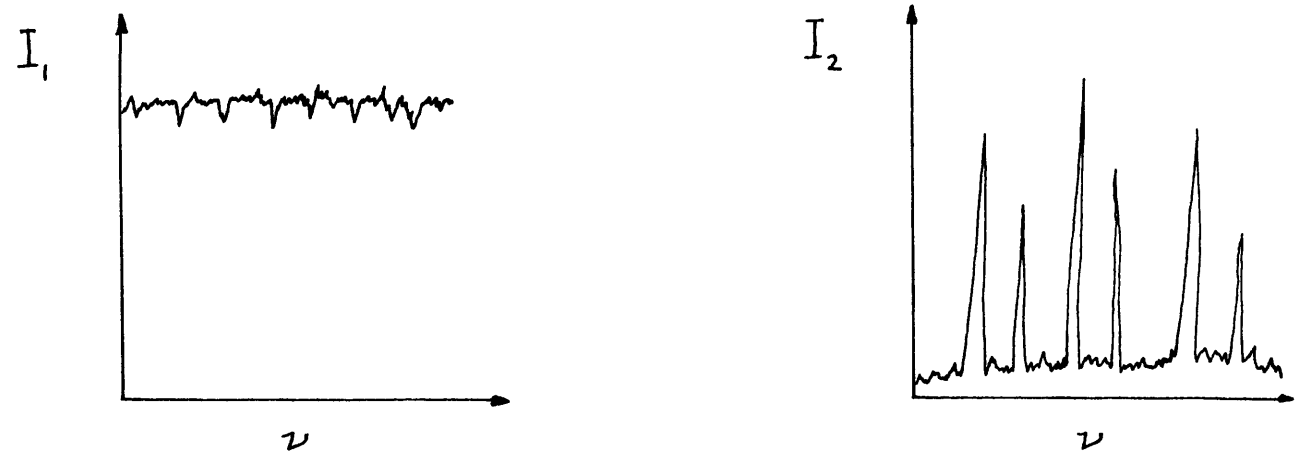
Figure c.4. Absorption versus laser induced fluorescence.

LASER
FOCUS
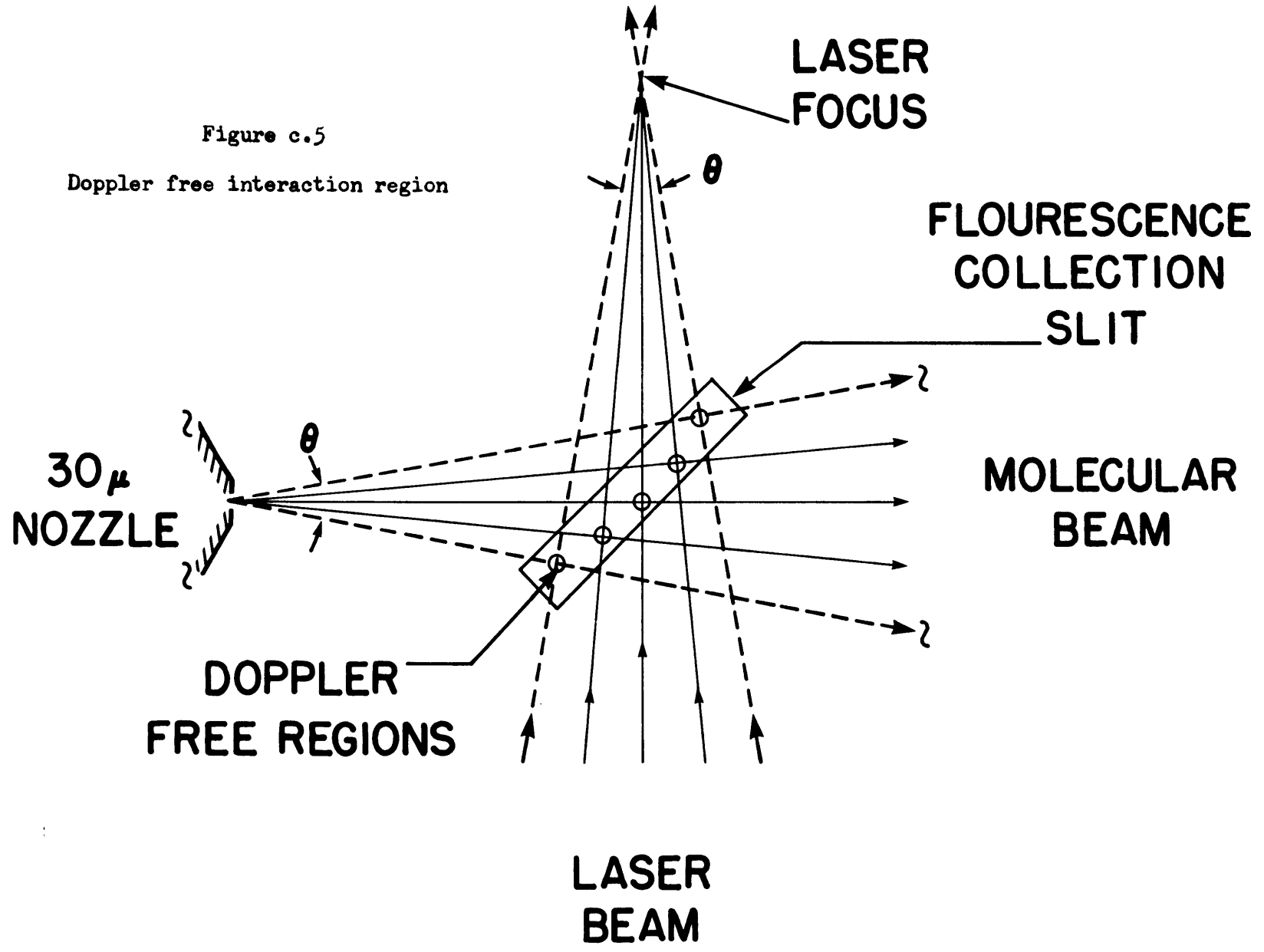
Figure c.5

Doppler free interaction region

FLOURESCENCE
COLLECTION
SLIT

θ

44

θ

30 μ
NOZZLE

MOLECULAR
BEAM

DOPPLER
FREE REGIONS

LASER
BEAM

particular trajectories of molecules within the molecular beam - eliminating the first order Doppler effect. A small rectangular baffle restricts the collection optics to gathering light chiefly from this interaction region (Fig. C.5). The position of the laser beam focus determines the orientation of the Doppler free area relative to the molecular beam axis. Spectra taken with this arrangement exhibit linewidths of 250 MHz as compared to the Doppler width of 1400 MHz for atoms in thermal equilibrium with the oven ($\sim$400°C).

B. OVEN TECHNOLOGY

The oven or molecular source is subject to stringent design considerations. It must be heated to give appreciable alkali vapor pressure (NES 63) it must maintain structural integrity at pressures in excess of 100 atmospheres while hot; it must resist corrosion from the alkali; and it must be easily serviceable.

The Na oven is a cigar shaped tube of 17-4-PH hardened stainless steel which is threaded on one end and is pressure sealed on the other end with a 316 S.S. Swagelok compression fitting and a copper "0" ring (Fig. C.6). The threaded end of the oven screws into a gas inlet port where a Teflon "0" ring forms a high pressure seal (Fig. C.7). The 17-4-PH

S.S. SHEATHED
HEATING ELEMENTS

Cu FOIL

MACHINED
303 S.S.
NOZZLE

STAINLESS
STEEL MESH

17-4-PH S.S.
OVEN

Cu HEATER
BLOCK

Cu "O" RING

316 S.S.
FITTING
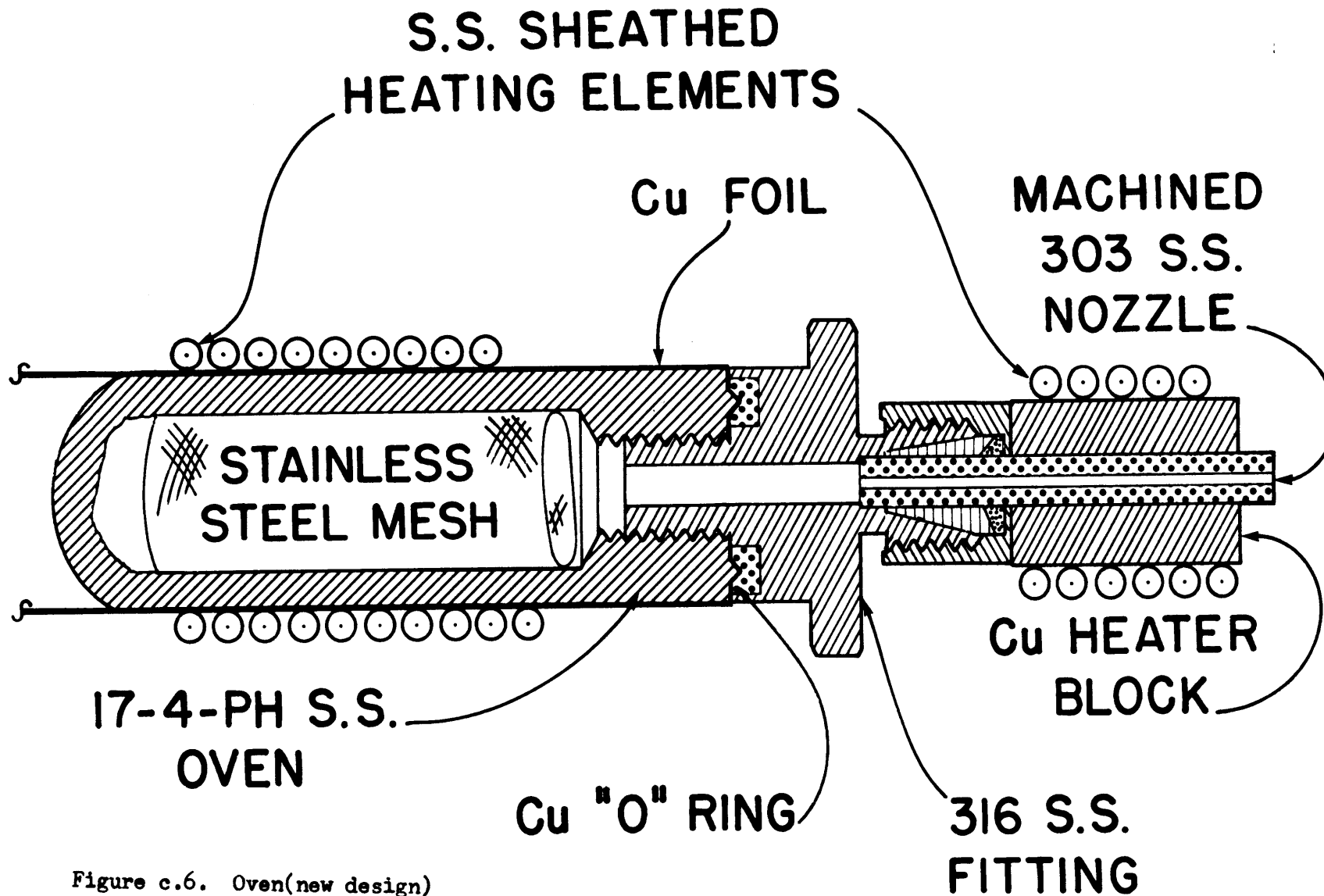
Figure c.6. Oven(new design)

46

SWAGELOK
1/8" - 1/8
MALE NPT

S.S. PLUG TURNED TO
FIT I.D. OF TUBE AND
ACCEPT SWAGELOK

OVEN
HOLDER
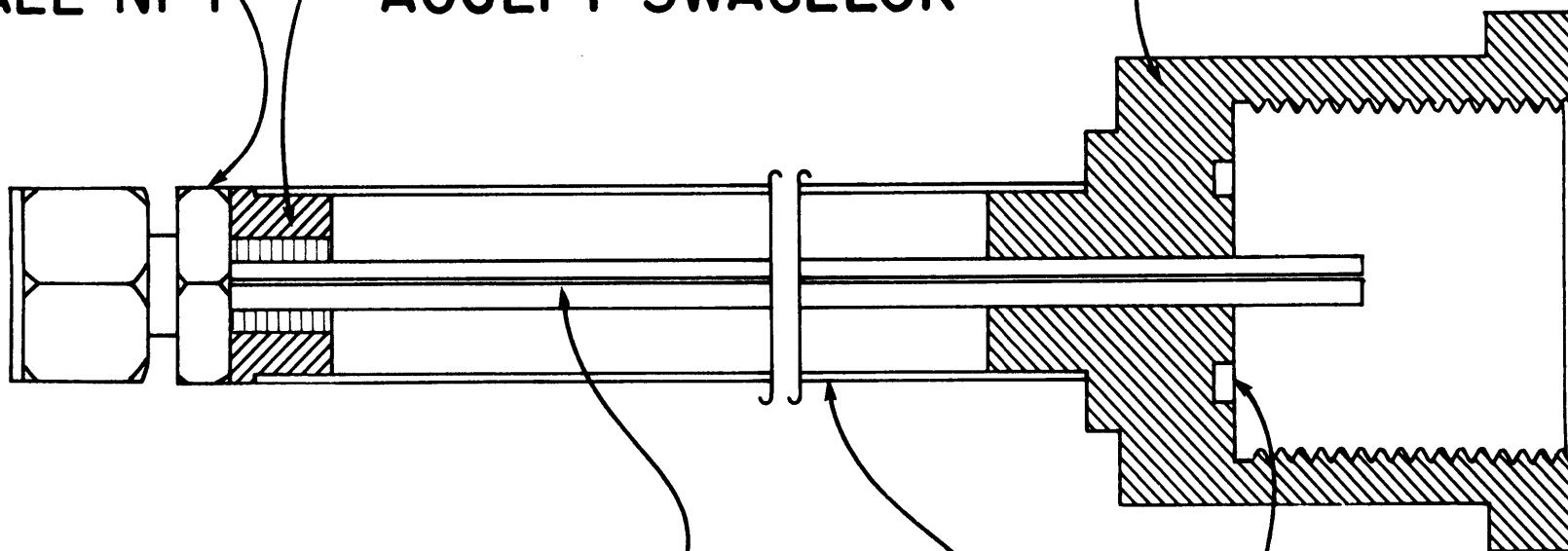
GAS (H.P.) TUBING

1/2" O.D. S.S. SUPPORT TUBING

"O" RING
GROOVE

Figure c.7. Oven holder

steel was chosen because it has a high yield strength at elevated temperatures and has good corrosion resistance to alkalis. The oven contains a 304 stainless steel boat holding approximately 1 gm. of sodium metal. Commercially available stainless steel sheathed heaters (ARI, Industries, Inc., Franklin Park, Ill.) wrapped around the oven elevate its temperature to 350-450°C giving the sodium a vapor pressure of 0.1 torr. A tungsten wire mesh is placed between the sodium ampoule and the nozzle to provide nucleation sites for droplet formation and impurity precipitation. This prevents liquid alkali or dirt from reaching and clogging the nozzle.

The nozzle, through which the alkali-gas mixture expands, is attached to the oven using a swagelok 1/8" nut and ferrules. A small copper block, shrouded with another heater, encompasses the nozzle, keeping it hotter ($\sim$25°C) than the oven to prevent alkali condensation. This method of attaching nozzles is far superior to the technique of pressure sealing described previously (LAM 80). Changing clogged nozzles can be done in minutes.

The nozzles themselves are of several configurations (see Fig. C.8) but can be characterized as brazed or integral. The brazed nozzles are made by silver brazing a modified molybdenum disk (electron microscope collimating

Figure c.8. Types of nozzles.

TYPE 1

0.080"   0.125"

FLAT BRAZE

1.125"

0.022"

MOLYBDENUM
APERTURE

BRAZE

TYPE 2

RECESSED
NOZZLE

35 μm HOLE
(TYPICAL)

1.0"

TYPE 3

DRILLED
NOZZLE

INTEGRAL
CONSTRUCTION

49
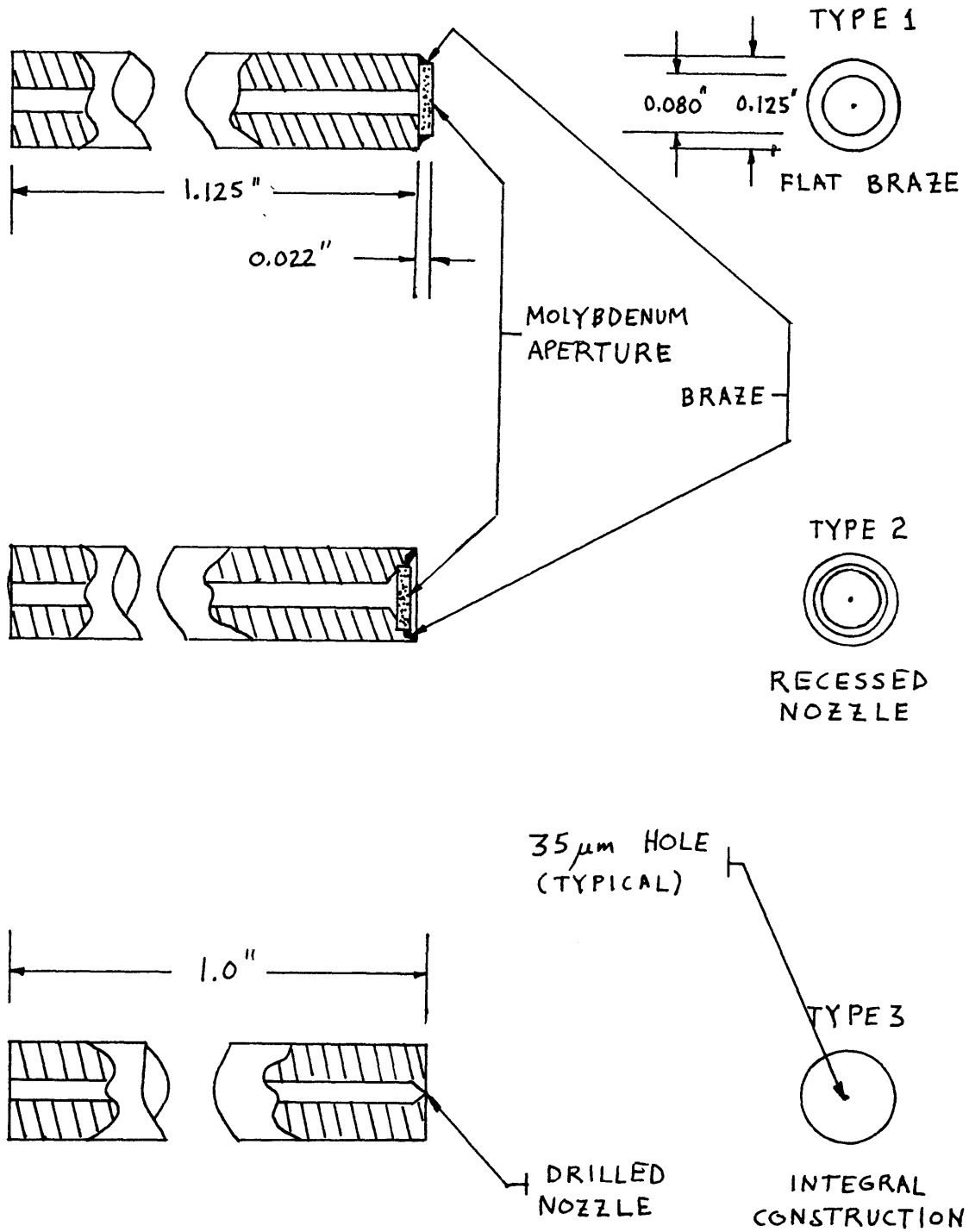
aperature – Ted Pella Co., Tustin, Ca., see also Appendix D)
to a short, thin (0.317 cm) 304 stainless steel tube. The
molybdenum disk contains a 30μ hole which is the nozzle.
The integral nozzles are made by drilling, in several steps,
into a single rod of 303 stainless steel. The integral noz-
zles are superior in that they do not fail under operating
conditions as the brazed nozzles often do because of inclu-
sions in and softening of the braze. Using the integrally
constructed nozzle our molecular beam works well about 90%
of the time. The primary disadvantage of these nozzles is
the erosion of the 303 S.S. by the alkali and the consequent
enlarging of the nozzle diameter. Average lifetimes for
such nozzles is three to four days of continual use, after
which the nozzle has eroded so that the throughput of gas
cannot be accomodated by our pumping system.

Chromel-alumel thermocouples are used to monitor the
oven's temperature near the sodium ampoule, the tungsten
mesh, and the nozzle. The whole oven and heater assembly is
shrouded with three layers of stainless steel foil which
serve as radiation shields. The entire assembly is mounted
on a x-y-z translator to facilitate alignment with the laser
beam and collection optics.

It should be mentioned that cleanliness when loading
and handling the oven is imperative if clogs are to be

avoided. The ovens and internal pieces are cleaned first in an acid bath ($HF+HNO_3$) to remove all oxides and residue from previous experiments. All pieces are then polished with stainless steel wool to remove burrs and loosened scale. The pieces are then put in a total degreasing bath of trichloroethlyene and agitated in an ultrasonic cleaner for a period of one hour. Everything is rinsed with acetone, and then ethyl alcohol. The pieces are then put in a final dilute solution of sodium hydroxide and agitated in the ultrasonic cleaner for another hour. On removing, everything is thoroughly rinsed with distilled water and baked to remove all moisture. All pieces are sealed in air tight containers until they are loaded with alkali and assembled.

Loading is done in a glove box purged with a continuous stream of helium gas flowing past a steel beaker of liquid nitrogen (to condense water vapor). The alkali is ultra pure (99.9% MSA Research, Evans City, Pa.) cut with a clean steel knife and packed into the ampoule with clean forceps. Polyethylene gloves are worn on the inside of the glove box.

Clogged nozzles sometimes can be opened while on the oven by carefully probing the hole with a thin, 0.003 cm, tungsten wire held in jewler's forceps. A good jeweler's loupe is necessary to prevent eye strain. Sometimes a drop of distilled water or methanol, applied while probing with

the wire, assists in unclogging the aperture. Acids are not to be used as they attack the molybdenum and 303 S.S. rapidly. If the clog cannot be dislodged the nozzle is removed and agitated in an ultrasonic cleaner in a solution of 50% water and 50% menthanol. Liquid inside the nozzle is removed using compressed gas and a hypodermic syringe, or canned freon.

C. LASER AND FREQUENCY REFERENCE

The tunable dye laser is a modified Spectra Physics 580, pumped by a Spectra Physics 179 cw Argon-ion laser. The original dye laser used a dye cell configuration in which the methanol and Rhodamine 6G mixture flowed between two anti-reflection coated glass plates. Maximum output power was achieved by focussing the pump laser beam near the surface of one of these glass cell windows. Frequently the cell window coating would burn due to localized heating caused by the sharply focussed pump laser beam. These catastrophes forced conversion of the 580 from the dye cell to a dye jet configuration in which the gain medium is Rhodamine 6G dissolved in ethylene glycol and passed as a free liquid jet through the laser cavity.

The method for scanning the laser's three tuning elements (prism, intra-cavity etalon, piezoelectric driven cav-

ity input mirror) is as follows. The sweep is initiated by applying a sawtooth voltage to a piezoelectric drive on the cavity. This displaces the cavity mirror linearly in time with the maximum excursion corresponding to an integral number of half-wavelengths. Flyback occurs on the falling edge of the sawtooth when the cavity PZT snaps back to its initial position, causing a cavity mode hop with no change in laser frequency. The intracavity etalon (FSR=200 GHz) is square wave modulated at 2 kHz, 50 mV, and a d.c. error voltage produced by phase detecting the laser intensity provides the input to an integrator. The resulting voltage ramp, applied to the etalon piezoelectric drive, keeps the etalon transmission centered on the scanning laser frequency. The a.c. servo loop gain is attenuated at high frequencies so that the etalon does not follow the rapid cavity flyback. In this way, single mode operation for frequency excursions greatly exceeding the free spectral range of the cavity is achieved (AHB 77). The third tuning element, the output prism, is used to select an etalon transmission peak, and is scanned in proportion to the etalon. The dye laser is intensity stabilized by controlling the pump laser intensity (2.5W all lines). Scan rates of .05 to 20 GHz/sec are possible.

Several glass microscope slides pick off portions of

the dye laser output beam and direct them into various optical elements on the laser table: a scanning Fabry-Perot spectrum analyzer (to examine the quality of the laser mode as it scans), the frequency reference system, and a sodium cell (visual observation of the atomic resonances). The laser beam passes through a holder containing neutral density filters to attenuate the laser light. This holder is positioned at an angle of $\sim 30°$ to reduce etalon effects of the reflecting neutral density filters. Finally, the laser beam enters the vacuum chamber through a tubular arm filled with annular baffles which reduce scattered light and define a minimum convergence angle for the laser beam of $\sim 3°$. The focussing is done with a biconvex lens, ~ 64 cm from the interaction region.

The frequency reference system consists of two Fabry Perot etalons with free spectral ranges (FSR) of $0.52964(16)$ cm^{-1} and $0.06330(10)$ cm^{-1}. Light transmitted through these etalons is detected by photodiodes and processed so that two combs of frequency reference marks (one from each etalon) may be displayed with the spectrum (AHB 77). These marks permit the frequency of any point on the trace to be determined simply by counting the number of etalon modes (marks) from the atomic sodium D-lines. Having two sets of frequency reference marks allows unambiguous overlapping of

individual traces so that the entire spectrum may be assimilated easily from the raw data. The etalons used are constructed from invar and are temperature stabilized to $0.01°C$.

The etalons are calibrated during each run by taking spectra of the atomic D-lines. Dividing the known D-line separation by the non-integral number of fringes measured yields the FSR for each etalon. Measurement of local temperature and barometric pressure are taken during each run to account for changes in the etalon's FSR. The FSR of the etalons changes only over long periods (seasonally) and remains constant over the time scale of an experiment, eg.:

$$FSR = 0.063352(10) \qquad 8-24-79$$
$$FSR = 0.063338(9) \qquad 7-19-79$$
$$FSR = 0.063330(10) \qquad 7-25-79$$

The errors quoted here are calculated from the total differential of the FSR: $FSR = \Delta/\chi$ where
$dF = - (\Delta/\chi^2)d\chi + (d\Delta/\chi)$. Here Δ is the fine structure splitting $\Delta = 17.1963(28)$ cm^{-1} and $\chi \approx 280$ markers.

This system allows us to assign the frequency of the observed lines to an accuracy of 0.003 cm^{-1} relative to the known atomic transition.

55

D. DETECTION

An f/1.4 camera lens with a focal length of 5 cm collects the molecular fluorescence perpendicular to both the molecular and laser beams. This collected light is then focussed onto the photocathode of a cooled RCA C31034 photomultiplier tube (Products for Research housing Model TE-104-RF). A cutoff filter (transmission below 6400Å) is permanently interposed between the lens and photocathode to eliminate background radiation due to primarily to oven heaters. A sliding drawer in the collection optics permits temporary insertion of other filters between lens and PMT during experimental runs (LAM 80).

The signal from the photomultiplier passes to a photon discriminator (Mechtronics 511) then into a diode pump (frequency to voltage converter - see Appendix C) which integrates the fast photon pulses. The count rate is monitored directly on a Hewlett Packard model 5321B scalar fed from an additional output on the photon discriminator. The analog signal generated by the diode pump passes into a Keithley electrometer (model 601). The output of the electrometer provides a convenient full scale (variable sensitivity) fluorescence signal for one channel of a two pen time base recorder (Ominiscribe model B-5216-5). The second channel is fed directly from the frequency reference

electronics, providing a fluorescence versus frequency recording (since the chart runs at a constant rate).

E.   EXPERIMENTAL TECHNIQUES AND DETAILS

The gas mixtures used in these experiments are helium and noble gas. A large concentration of helium has been shown to prevent undesirable rare gas dimer condensation in the molecular beam (FED 66, RSV 71). Optimal mixtures for producing NaNe were 40-50% Ne and 60-50% He, in contrast to the (70% Ne - 30% He) mixture ("first run" Ne) reported earlier (ALP 77). In the case of NaAr, a mixture of 3% Ar (grade 0.5) with 97% He provided maximum van der Waals molecular formation in agreement with previous work (SAF 77). The gas mixtures, in both cases, are purified by a pre-baked, activated alumina column before passing through a cold trap to remove all condensables. Liquid nitrogen (77K) is used in the cold trap when a He-Ne mixture is being used, however dry ice and isopropyl alcohol (195K) must be used for He-Ar mixtures since Ar solidifies at temperatures below 150.7K with pressures in excess of 48 atmospheres.

The NaNe and NaAr lines are discriminated from the Na_2 spectra by their intensity variation with gas pressure and by their hyperfine structure. An increase in neon pressure supressed the Na_2 lines and enhanced the van der Waals sig-

nal. Most van der Waals lines are observed to consist of

two components split by the sodium ground state hyperfine

splitting of 1.773 GHz, with approximately the expected 5:3

intensity ratio. Lines whose hyperfine companions overlap

other lines can be identified as NaNe or NaAr by comparing

them with Na_2 spectra taken at lower gas pressures. Spectra

taken on different days are compared with respect to signal

to noise, linewidth, intensity regularity, oven stability,

etc., ensuring that the data which were analyzed were the

best available.

Those molecular bands in the strong wings of the atomic

D-lines [NaNe: $A^2\Pi_{1/2} - X^2\Sigma^+(5,\emptyset)$] or directly overlapping

the atomic resonances [NaAr: $A^2\Pi_{3/2} - X^2\Sigma^+ (12,\emptyset)$] are

observed by inserting neodynium doped filters (Schott BG-36)

in the collection optics through a sliding drawer. These

filters absorb strongly in the region 57$\emptyset\emptyset$-5925Å but only

∿15% in the region 5925-75$\emptyset\emptyset$Å. When the laser is tuned near

the atomic resonance lines, the light excites both the

near-resonant atomic transitions and molecular transitions.

The atoms re-radiate this yellow light whereas the molecules

re-radiate into all the vibrational levels of the ground

electronic state, red degrading the fluorescence relative to

the excitation frequency. The resonantly scattered atomic

radiation is attenuated by the filters while the molecular

fluorescence is largely transmitted. With this technique we are able to collect molecular spectra to within 0.06 cm^{-1} of the atomic lines (Fig. C.9, C.10, C.11).

Once van der Waals signal is seen, an iterative "peaking" procedure is followed to achieve best signal. The x-y-z position of the oven and optical tower is optimized, as well as the gas pressure and slit orientation.

Our best data were obtained at a chamber pressure of 0.1 torr and a pressure of ≥ 100 atm. in the oven; the Na reservoir temperature was 390°C with the nozzle slightly hotter at 420°C to prevent sodium vapor from condensing the clogging the aperture. The cw single mode dye laser power was ~ 10 mW (with roughly 2.5W all lines pump power). The laser linewidth was measured to be ~ 100 MHz using a Spectra Physics 2 GHz free spectral range spectrum analyzer. Operating the photomultiplier at 1500 VDC we recorded maximum counting rates of $10^5 s^{-1}$ (NaNe signal) and $10^6 s^{-1}$ (NaAr signal) with a measured background of $< 10^3 s^{-1}$. The dark counts were $\sim 20 s^{-1}$. Typical linewidths on the trace were 300 MHz compared to the Doppler width of 1400 MHz for molecules in thermal equilibrium with the oven. Each trace was 5 cm^{-1} long, taken at a rate of 1 or .5 GHZs^{-1}.

Figure c.9
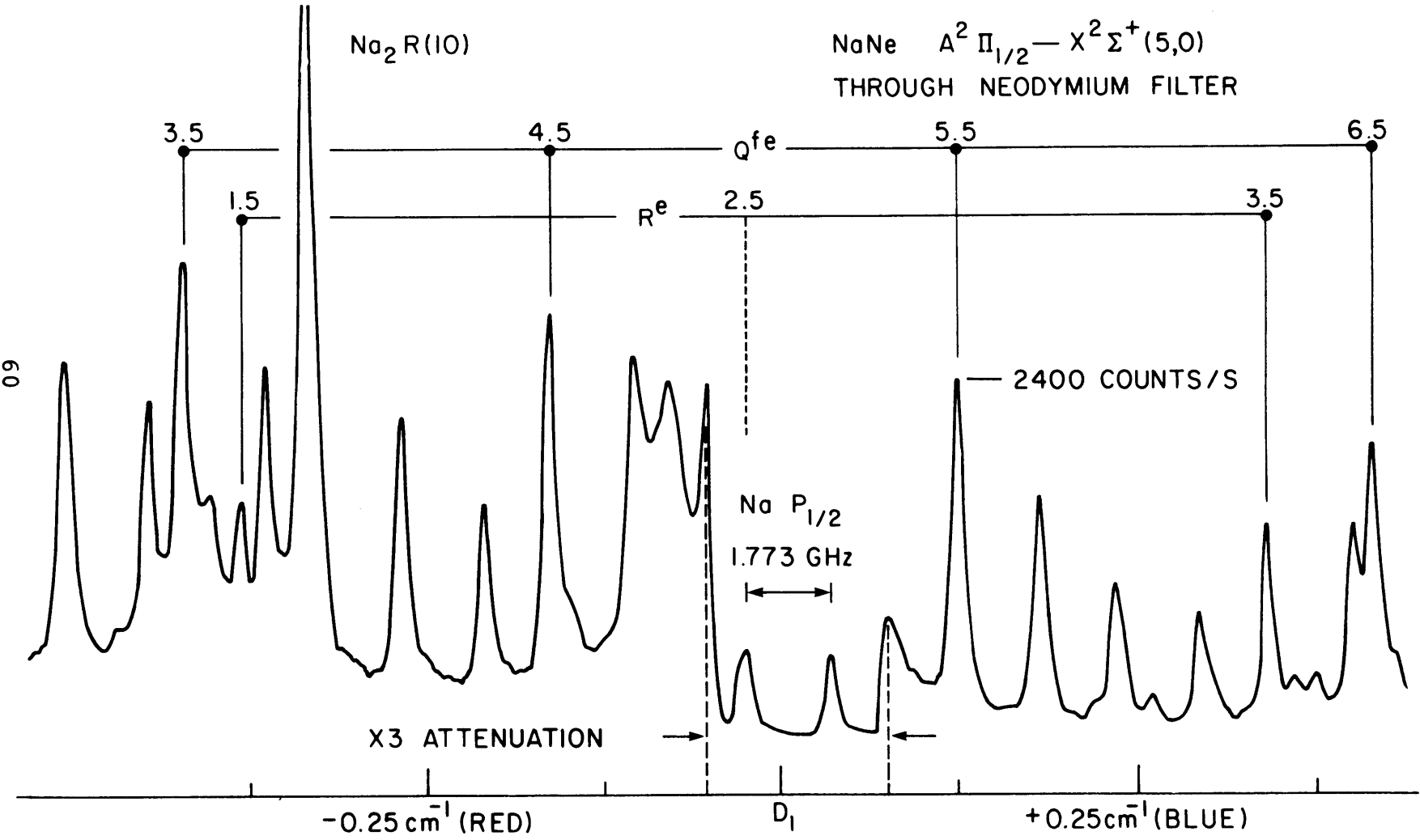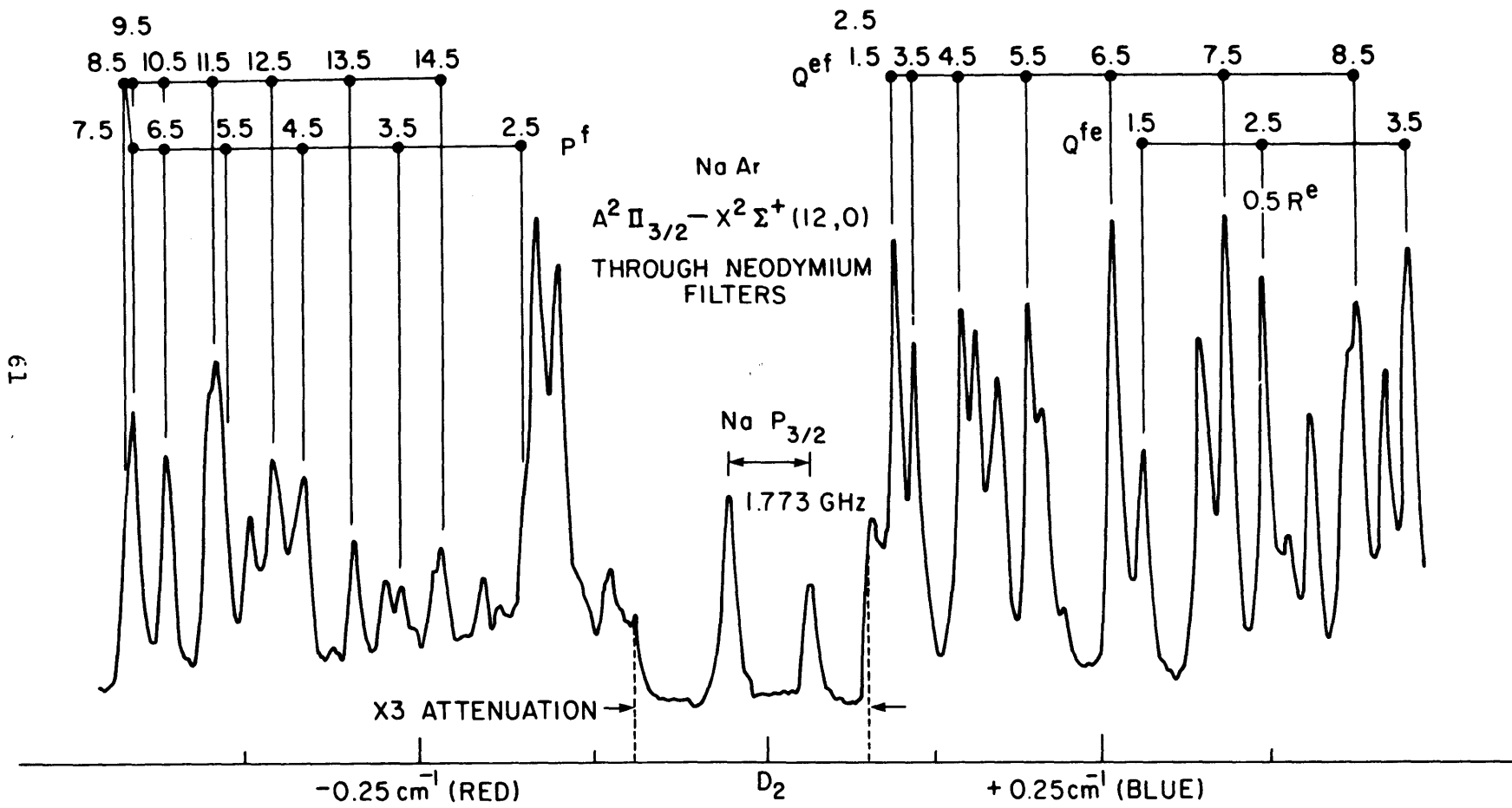
Figure c.10

Figure c.11

$NaAr \quad A^2\Pi_{3/2} - X^2\Sigma^+ (12,0)$

X3 ATTENUATOR REMOVED
FROM LASER BEAM TO
SHOW STRONG ATOMIC
RESONANCE

$Na \quad ^2P_{3/2} - ^2S_{1/2}$

$0.06333(10)\ cm^{-1}$
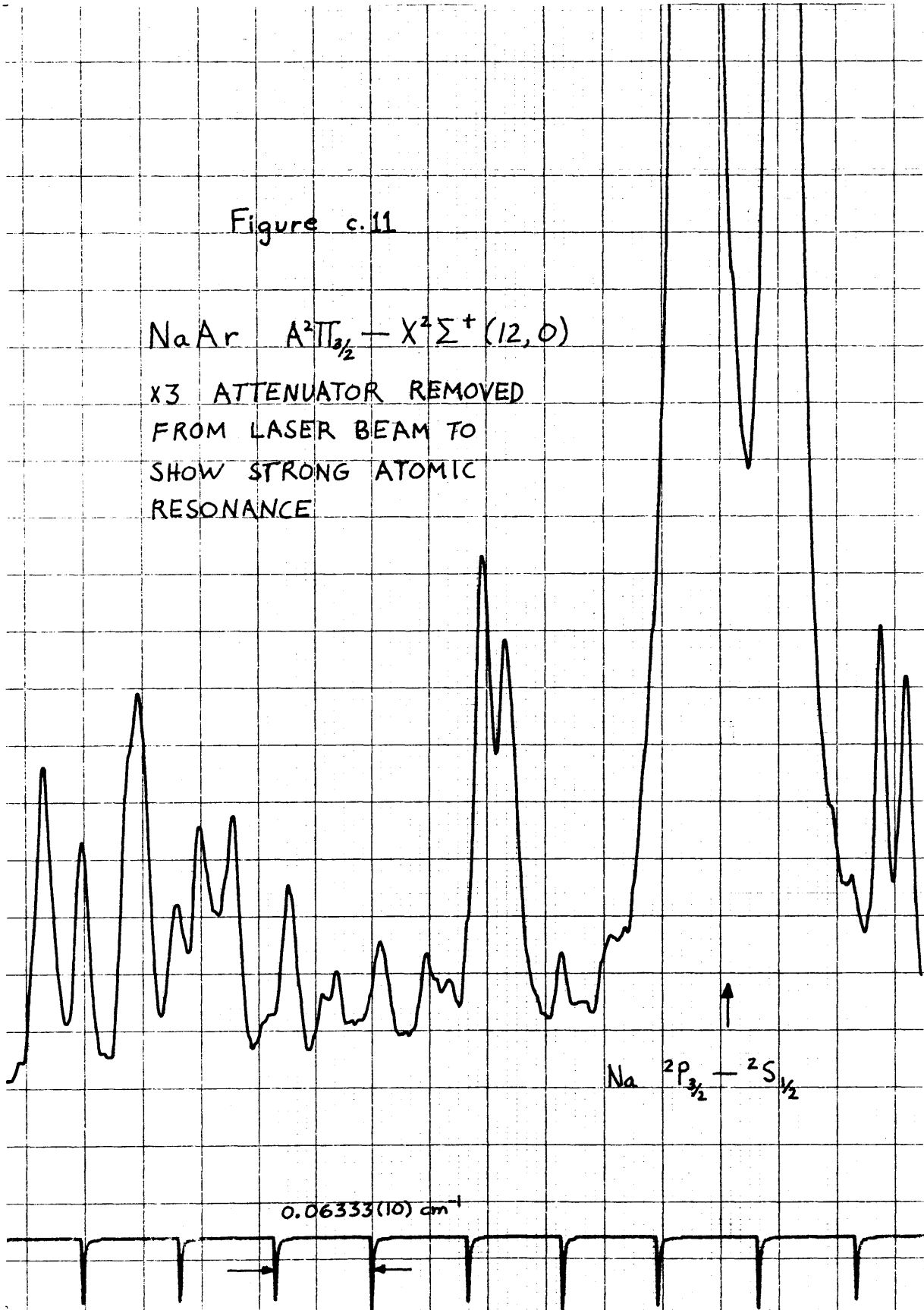
CHAPTER IV

RESULTS AND ANALYSIS

A. ROTATIONAL ANALYSIS

This analysis is conducted using traditional techniques
(HER 50). The $X^2\Sigma^+$ rotational energy level spacings are
deduced from an assignment of the most obvious band for NaNe
and calculated for NaAr using previously determined ground
state parameters (SAF 77, TRK 79). These energy level spac-
ings are known as ground state combination differences and
provide us with a pattern which is used as a tool to assign
rotational quantum numbers to lines in other rovibronic
bands. These combination differences depend only on the
ground state and are unaffected by perturbations in the
excited states, so the discerned pattern can be used to
analyze all observed bands. Only one set of ground state
level spacings was required for NaNe because all analyzed
bands were found to emanate from the v" = 0 vibrational
level, however, in NaAr level spacings for v" = 0, 1 and 2
were required since bands originating from all these levels
are observed.

Band origins, ν_{vo}, effective rotational constants, B_v,
and Λ-doubling parameters were deduced from each band
assignment. Deperturbed constants are obtained from a fit

to a model Hamiltonian which is discussed briefly in Appendix B, and in more detail in the references (GOT 79, GLP 80).

It is convenient to assign the rotational lines by the quantum number, $\vec{J} = \vec{N} + \vec{S}$. For energy levels of the $X^2\Sigma^+$ state with the same N, $e(F_1)$ levels have $J'' = N + 1/2$, and $f(F_2)$ levels $J'' = N - 1/2$. The absolute numbering of the branches is determined by the agreement of the combination differences $\Delta_1 F''(J)$ and $\Delta_2 F''(J)$ of the ground $X^2\Sigma^+$ state. The second combination differences

$$(4.1) \qquad \Delta_2 F_e''(J) = R^e(J-1) - P^e(J+1) = T_e''(J-1) - T_e''(J+1)$$

$$(4.2) \qquad \Delta_2 F_f''(J) = R^f(J-1) - P^f(J+1) = T_f''(J-1) - T_f''(J+1)$$

are equal (for the same J', but different v') even in the presence of Λ-doubling of the upper state [interaction between $B^2\Sigma^+$ with $A^2\Pi_r$ produces Λ-doubling, (HER 50, HOU 70)]. The ground state term energies, $T''_{e,f}$, are indicated as explicit functions of parity and J''. Because of the negligible spin rotation splitting in the ground state ($\gamma'' \approx 0$), $R^f(J+1)$ is superimposed on $Q^{fe}(J)$, and $\Delta_2 F''_f(J)$ equals $\Delta_2 F''_e(J+1)$. The first combination differences are given by

64

$(4.3a)$ $\qquad \Delta_1 F''_e(J) = R^e(J) - R^f(J)$

$$= P^e(J) - P^f(J)$$

$(4.3b)$ $\qquad \Delta_1 F''_e(J) = T''_f(J) - T''_e(J)$

$(4.4a)$ $\qquad \Delta_1 F''_f(J) = R^e(J) - Q^{fe}(J+1)$

$$= Q^{ef}(J-1) - P^f(J)$$

$(4.4b)$ $\qquad \Delta_1 F''_f(J) = T''_e(J+1) - T''_e(J)$

Here $R^f(J)$ is superimposed on $Q^{fe}(J+1)$ and $P^e(J)$ is superimposed on $Q^{ef}(J-1)$. The combination difference $\Delta_1 F''_e(J)$ equals $\Delta_1 F''_f(J-1)$. The Λ-type doubling of the $A^2\Pi_{3/2}$ state is small and the relations given above are applicable. For the $A^2\Pi_{1/2}$ state, the Λ-doubling is large, which results in a systematically increasing combination defect so the equations (4.3) and (4.4) are not even approximately correct. Instead

(4.5) $\qquad R^e(J) - R^f(J) \quad = T''_f(J) - T''_e(J) + \delta$

(4.6) $\qquad Q^{ef}(J-1) - P^f(J) = T''_f(J) - T_e(J) + \delta$

65

where δ is the splitting of the $A^2\Pi_{1/2}$ levels. This splitting increases linearly with J' and can be parameterized as

$$(4.7a) \qquad \delta = - (p + 2q)(J + 0.5)$$

where the J here refers to the same J as equations (4.5) and (4.6), and $(p + 2q)$ are the Λ-doubling parameters (see Appendix B). The $A^2\Pi_{1/2}$ component is also identified by its first rotational lines $Q^{fe}(0.5)$, $Q^{ef}(1.5) + P^e(1.5)$, and $P^f(1.5)$, which do not exist for $A^2\Pi_{3/2} - X^2\Sigma^+$.

Table IV.1 shows the results of the method described above. It lists the first combination differences $\Delta_1 F''(J)$ and the second combination difference $\Delta_2 F''(J)$ for $A^2\Pi_{3/2} - X^2\Sigma^+$ (12,0) in NaAr.

Λ-doubling constants $(p + 2q)$ are derived from the first combination difference, or by an equivalent technique – adding ground state rotational term values to the observed transitions and then subtracting the resultant excited state term energies, T'_e and T'_f.

$$(4.7b) \qquad (p + 2q) = - (T'_e - T'_f)/x$$

where $x = J + 0.5$.

Rotational constants, B^e and B^f, are extracted from the

TABLE IV.1. Sample first and second combination differences for $A^2\Pi_{3/2} - X^2\Sigma^+(12,0)$ in NaAr. The first combination differences show no difference between e and f parity for the same J – indicating an absence of Λ-doubling as expected.

J	$\Delta_2 F''(J)$	$\Delta_2 F''(J)$	$\Delta_1 F''_e(J)$	$\Delta_1 F''_f(J)$
.05				
1.5	0.262(6)		0.084(5)	
2.5	0.437(6)	0.448(7)	0.175(6)	
3.5	0.623(5)	0.620(6)	0.266(5)	0.270(7)
4.5	0.798(5)	0.794(6)	0.358(5)	0.358(6)
5.5	0.973(4)	0.969(7)	0.441(5)	0.437(6)
6.5	1.148(6)	1.151(6)	0.530(6)	0.530(7)
7.5	1.324(5)	1.325(7)	0.619(5)	0.620(6)
8.5	1.496(4)	1.496(7)	0.705(5)	0.706(7)
9.5	1.668(6)	1.670(7)	0.794(6)	0.793(7)
10.5	1.839(5)	1.838(7)	0.879(5)	0.880(7)
11.5	2.017(7)	2.006(6)	0.970(7)	0.965(6)
12.5		2.180(4)		1.046(6)
13.5		2.346(5)		1.132(5)
14.5		2.510(5)		1.219(6)
15.5				1.303(5)

excited state term energies as well,

$$(4.7c) \qquad B^{e(f)} = (T'_{e(f)}(J) - T'_{e(f)}(J+1))/2x$$

The B^e and B^f are averaged to give the rotational constant, B'.

B. DESCRIPTION OF BANDS OBSERVED

The excitation spectrum recorded for these van der Waals molecules is a mixture of $A^2\Pi_r - X^2\Sigma^+$, $B^2\Sigma^+ - X^2\Sigma^+$, some Na_2 $A^1\Sigma_u^+ - X^1\Sigma_g^+$, and the Na D lines. Since all of the spectral features of NaNe and NaAr occur near the atomic D lines, frequencies of the molecular lines are reported relative to this natural fiduciary as well as in absolute wavenumbers for general utility (see Table IV.2 and IV.3). All NaNe $A^2\Pi_r - X^2\Sigma^+$ bands observed are blue degraded (lines with high J at higher frequency) and do not have pronounced band heads. The $B^2\Sigma^+ - X^2\Sigma^+$ bands observed in both NaNe and NaAr are red degraded because $B' < B''$. All of the $A^2\Pi_{3/2} - X^2\Sigma^+$ bands in NaAr are blue degraded, as are most of the $A^2\Pi_{1/2} - X^2\Sigma^+$. Two bands, $A^2\Pi_{1/2}(16,0)$ and $A^2\Pi_{1/2}(17,0)$ are red degraded. NaAr has a rich spectrum to the red of the D_1 line, which has been analyzed previously (SAF 77). Only the newly observed spectral features of

TABLE IV.2. Rotationless band origins of NaNe and NaAr. NaNe isotopic bands are idicated with an asterisk. NaAr data marked with a dagger($\dagger$) are the newly observed bands. Other NaAr data are taken from the literature (SAF 77). For discussion of errors see text.

TRANSITION	NaNe		NaAr	
	BAND	$\nu_o \,[\mathrm{cm}^{-1}]$	BAND	$\nu_o \,[\mathrm{cm}^{-1}]$
$A^2\Pi_{1/2} - X^2\Sigma^+$	(3,0)	16929.873	(7,0)	16847.923
	(4*,0)	16943.885	(8,1)	16867.813
	(4,0)	16945.247	(8,0)	16879.033
	(5,0)	16955.169	(9,0)	16905.443
	(6,0)	16958.158	(10,0)	16927.563
			(11,0)	16945.823
			(16,0)$\dagger$	16986.453
			(17,0)$\dagger$	16990.163
$A^2\Pi_{3/2} - X^2\Sigma^+$	(3,0)	16941.987	(7,1)	16851.446
	(4,0)	16957.276	(7,0)	16862.700
	(5*,0)	16966.412	(8,0)	16893.313
	(5,0)	16967.473	(9,0)	16919.303
	(6,0)	16973.796	(10,0)	16941.064
			(11,0)$\dagger$	16959.062
			(13,2)$\dagger$	16962.337
			(12,0)$\dagger$	16973.640
$B^2\Sigma^+ - X^2\Sigma^+$	(b,0)	16976.069	(0,0)$\dagger$	16988.555
	(b+1,0)	16977.522	(b,0)$\dagger$	17007.173

TABLE IV.3 NaAr band origins (relative to atomic resonance lines) and experimentally determined constants. The rotational constants, B', and Λ-doubling constants, (p + 2q), are determined from a traditional analysis. Data fit to the model Hamiltonian are indicated

NaAr Transition	Band origin relative to atomic line indicated	Experimentally determined		Fit to the Data		
		$B'[cm^{-1}]$	$(p+2q)[cm^{-1}]$	$B'[cm^{-1}]$ $\times\ 10$	$(p+2q)[cm^{-1}]$	$D[cm^{-1}]$
$A^2\Pi_{1/2}-X^2\Sigma^+$	D_1					
(16,0)	30.270(8)	0.0210(68)	-0.0224(73)			
(17,0)	33.980(5)	0.0162(29)	-0.0103(22)			
$A^2\Pi_{3/2}-X^2\Sigma^+$	D_2					
(11,0)	-14.317(4)	0.0583(10)	-0.0002(8)	0.58993(62)	0.0	$-3.2(\pm2.1)\times10^{-6}$
(13,2)	-11.042(5)	0.0452(24)	-0.0002(24)			
(12,0)	0.261(3)	0.0520(8)	-0.0003(5)	0.52914(49)	0.0	$1.86(2)\times10^{-6}$
$B^2\Sigma^+-X^2\Sigma^+$	D_2					
(0,0)	15.176(7)	0.0197(37)	+0.0150(20)			
(0,b)	33.794(6)	0.0143(38)	+0.0389(38)			

NaAr, blue of the D_1 line, are reported in this section.

Neon has two stable isotopes: ^{20}Ne and ^{22}Ne, with abundance 90.92% and 8.82% respectively, while sodium has only one stable isotope, ^{23}Na. Two bands between the D_1 and D_2 lines are attributed to Na^{20}Ne and Na^{22}Ne:

$A^2\Pi_{3/2} - X^2\Sigma^+(5,0)$ at 5.903(2) and 6.967(2) cm^{-1} red of D_2 line respectively. The Na^{22}Ne band is an order of magnitude weaker relative to the corresponding Na^{20}Ne band consistent with the isotopic abundances. The Na^{20}Ne $A^2\Pi_{3/2} - X^2\Sigma^+(5,0)$ is the most intense band observed in the $A^2\Pi_r - X^2\Sigma^+$ system ($\sim 3 \times 10^5$ counts). It is not overlapped by any Na$_2$ bands, and it exhibits line broadening at high J [as does $A^2\Pi_{3/2} - X^2\Sigma^+(4,0)$] which is attributed to rotational predissociation to the $A^2\Pi_{1/2}$ continuum (GLP 80).

Four bands to the red of the atomic Na lines are attributed to the Na^{20}Ne molecule; namely $A^2\Pi_{1/2} - X^2\Sigma^+(3,0)$, (4,0), and (5,0) at 26.310(2), 10.936(5), 1.014(5) cm^{-1} red of D_1 line respectively, and $A^2\Pi_{3/2} - X^2\Sigma^+(3,0)$ at 31.392(2) cm^{-1} red of D_2 line. The correct vibrational numbering of the bands was established by an isotopic analysis which is described in Appendix D and verified by an alternate technique in section C.

Argon has only one naturally occurring isotope, so no NaAr isotopic bands are observed. The NaAr spectrum between

71

the D lines is exceptionally dense - 45 lines per wavenumber. One moderately intense band ($\sim 10^5$ counts) $A^2\Pi_{3/2} - X^2\Sigma^+(13,2)$ 11.042(5) cm^{-1} red of the D_2 lines, has been assigned here. Other bands are present in this region as evidenced by individual NaAr lines which are distinguished by their hyperfine components. No assignment is available for the remaining lines, however both $A^2\Pi_{3/2} - X^2\Sigma^+(12,0)$ and (13,0) are predicted to occur in this region.

NaNe $A^2\Pi_{3/2} - X^2\Sigma^+$ (6,0) occurs at 0.417(5) cm^{-1} blue of the D_2 line. Here R^e and $R^f + Q^{fe}$ branches could only be tentatively assigned because the intensity is low and because $Q^{ef} + P^e$ and P^f are hidden under the D_2 line.

Two transitions to a bound NaNe $B^2\Sigma^+$ state are observed: $B^2\Sigma^+ - X^2\Sigma^+(b,0)$ and $B^2\Sigma^+ - X^2\Sigma^+$ (b + 1, 0) at 2.690(3) and 4.143(3) cm^{-1} blue of the D_2 line respectively. The vibrational numbering of the levels in $B^2\Sigma^+$ is uncertain and will be discussed in the Long Range Analysis section. Four branches are identified: R^e, $R^f + Q^{fe}$, $Q^{ef} + P^e$, and P^f. A pure $^2\Sigma^+ - {}^2\Sigma^+$ is expected to have strong P and R branches and weak Q branches. The strong Q branches arise from spin-orbit mixing with the $^2\Pi_{1/2}$ state, and the observed band might be described more accurately as $|3/2,1/2\rangle - X^2\Sigma$. The notation $|j_\alpha,\Omega\rangle$ identifies the "good"

Figure d.1

NaAr $A^2\Pi_{3/2} - X^2\Sigma^+(11,0)$

73

ENERGY [cm⁻¹]
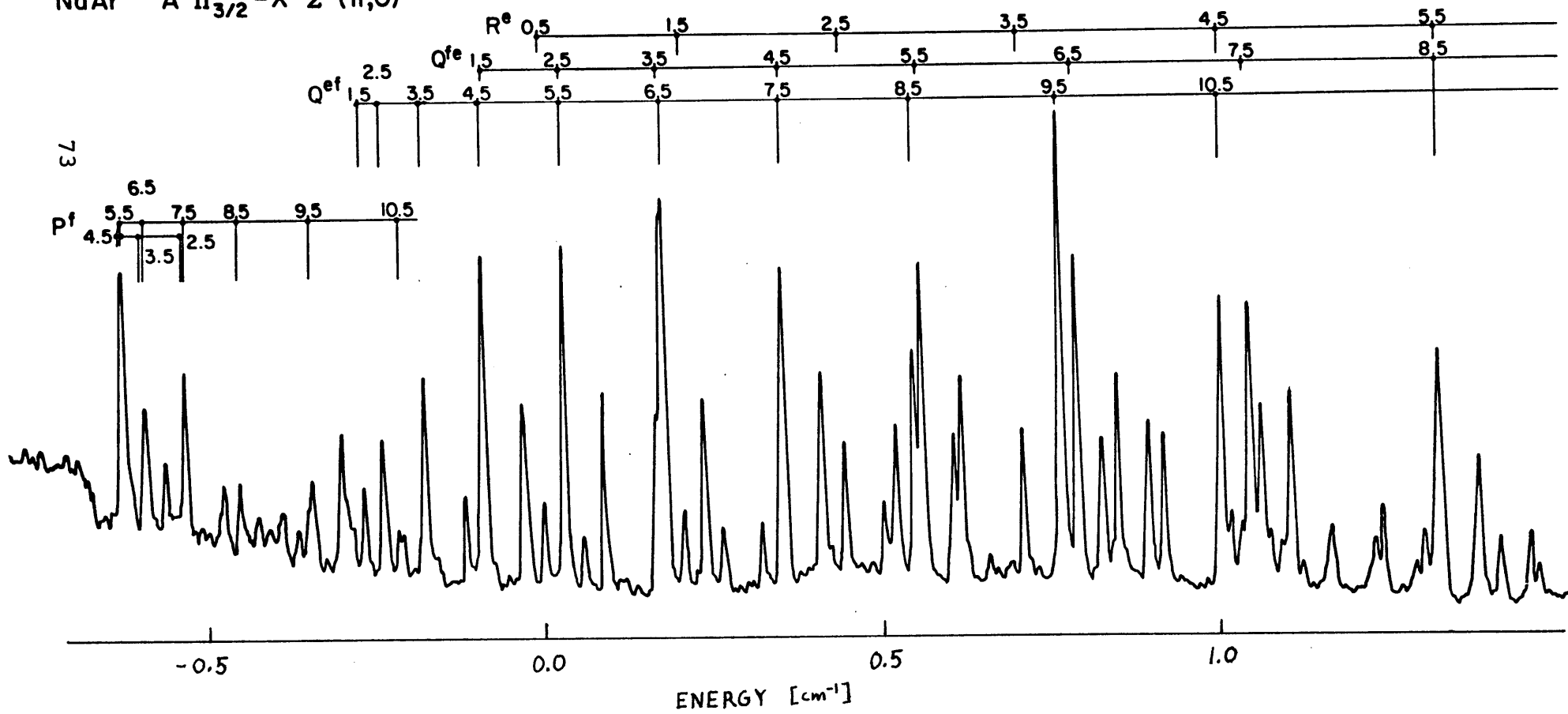
quantum numbers in Hund's case (c) – separated atom limit – coupling (HER 50).

In NaAr two $B^2\Sigma^+$ – $X^2\Sigma$ bands have been analyzed, namely the $(0,0)$ and $(b,0)$ at 15.176(7) and 33.794(6) cm^{-1} blue of the D_2 line, respectively. The $(0,0)$ band is intense ($\sim 1.2 \times 10^4$ counts) compared to the $(b,0)$ band ($\sim 3.5 \times 10^3$ counts) and all other features blue of the D_2 resonance. This is expected as the $B^2\Sigma^+$ – $X^2\Sigma^+(0,0)$ Franck Condon factor should be largest. The vibrational numbering, b, of the second analyzed band is uncertain. Three weak NaAr bands ($< 10^3$ counts) are seen between the $(0,0)$ and $(b,0)$ bands at approximately 20.1, 22.4 and 31.3 cm^{-1} blue of the D_2 line. However, very intense overlapping Na_2 bands and the paucity of lines in general make analysis of these bands doubtful.

In both molecules these $B^2\Sigma^+$ – $X^2\Sigma^+$ bands cannot be assigned as $A^2\Pi_{3/2}$ – $X^2\Sigma^+$ because the rotational constants and band origins observed are different from those predicted for the latter. In the case of NaAr, vanishingly small ($< 10^{-6}$) Franck Condon factors (see Appendix E) for $A^2\Pi_{3/2}$ – $X^2\Sigma^+(v',0)$, $v' > 13$, further strengthen the $B^2\Sigma^+$ – $X^2\Sigma^+$ assignments.

As the vibrational spacing gets smaller than the rotational energy (high v'), mutual perturbation of the $^2\Pi_r$ components was observed in NaNe. The mutual perturbation is

TABLE IV.4a.   NaAr Line Lists

$$A^2\Pi_{3/2} - X^2\Sigma^+(12,0)$$

J"	R^e	Q^{fe}	Q^{ef}	P^f
0.5	73.739(4)			
1.5	73.914(4)	73.665(3)	73.477(4)	
2.5	74.110(4)	73.739(4)	73.477(4)	73.207(6)
3.5	74.320(4)	73.844(3)	73.487(3)	73.119(4)
4.5	74.542(3)	73.962(3)	73.523(3)	73.050(5)
5.5	74.782(5)	74.101(3)	73.571(3)	72.993(6)
6.5	75.036(3)	74.252(3)	73.633(4)	72.951(5)
7.5	75.302(3)	74.417(4)	73.714(4)	72.921(6)
8.5	75.582(4)	74.597(4)	73.807(3)	72.921(6)
9.5	75.870(3)	74.788(5)	73.915(4)	72.927(6)
10.5	76.180(6)	74.991(4)	74.031(4)	72.950(5)
11.5		75.210(3)	74.163(4)	72.985(5)
12.5		75.431(3)	74.304(5)	73.031(3)
13.5		75.659(3)	74.452(3)	73.085(4)

TABLE IV.4b. $A^2\Pi_{3/2} - X^2\Sigma^+(11,0)$

J"	R^e	Q^{fe}	Q^{ef}	P^f
0.5	59.173(3)			
1.5	59.381(3)	59.090(4)	58.911(3)	
2.5	59.620(3)	59.205(4)	58.940(4)	58.646(4)
3.5	59.880(3)	59.350(4)	59.000(3)	58.585(4)
4.5	60.177(3)	59.522(4)	59.087(4)	58.551(5)
5.5	60.496(4)	59.732(3)	59.209(4)	58.562(5)
6.5		59.961(3)	59.353(4)	58.591(4)
7.5		60.216(3)	59.526(4)	58.649(4)
8.5		60.500(4)	59.720(3)	58.727(3)
9.5		60.819(3)	59.938(4)	58.835(4)
10.5			60.191(4)	

TABLE IV.4c $\quad A^2\Pi_{3/2} - X^2\Sigma^+(13,2)$

J"	R^e	Q^{fe}	Q^{ef}	P^f
0.5	62.427(3)			
1.5	62.584(3)	62.354(4)	62.203(4)	
2.5	62.751(6)	62.440(4)	62.215(3)	61.991(4)
3.5	62.914(4)	62.532(3)	62.234(3)	61.932(3)
4.5	63.108(6)	62.619(4)	62.261(4)	61.869(4)
5.5	63.334(3)	62.751(6)	62.294(6)	61.815(5)
6.5	63.579(5)	62.852(3)	62.383(5)	61.806(6)
7.5	63.843(4)	63.042(4)	62.483(5)	61.771(3)
8.5	64.127(3)	63.269(4)	62.610(4)	61.815(5)
9.5	64.429(3)	63.475(4)	62.751(6)	61.882(5)
10.5		63.720(4)	62.914(4)	61.961(5)
11.5				62.049(5)
12.5				

TABLE IV.4d $A^2\Pi_{1/2} - X^2\Sigma^+(16,0)$

J''	R^e	Q^{fe}	Q^{ef}	P^f
0.5	86.554(5)			
1.5	86.580(4)	86.404(4)	86.289(5)	
2.5	86.472(4)	86.289(5)	86.140(3)	85.957(8)
3.5	86.404(4)	86.153(4)	85.853(4)	85.667(5)
4.5	86.299(5)	85.957(8)	85.602(4)	85.361(6)
5.5	86.200(3)	85.739(4)	85.335(5)	84.998(5)
6.5	86.069(7)	85.492(3)	85.060(5)	84.596(6)
7.5	85.889(7)	85.219(6)	84.732(6)	84.187(5)
8.5	85.658(5)	84.903(6)	84.399(4)	83.709(5)
9.5				
10.5				

TABLE IV.4e $A^2\Pi_{1/2} - X^2\Sigma^+(17,0)$

J"	R^e	Q^{fe}	Q^{ef}	P^f
0.5	90.221(6)	90.179(4)	90.113(6)	
1.5	90.227(6)	90.120(6)	89.949(5)	89.902(6)
2.5	90.179(4)	90.024(3)	89.780(3)	89.666(6)
3.5	90.072(3)	89.877(6)	89.558(3)	89.402(4)
4.5	89.902(6)	89.666(6)	89.270(3)	89.075(3)
5.5	89.666(6)	89.402(4)	88.929(6)	88.694(6)
6.5	89.349(3)	89.062(3)	88.505(4)	88.246(6)
7.5	88.955(6)	88.694(6)	88.021(3)	87.732(6)
8.5	88.473(4)		87.453(3)	87.191(6)
9.5			86.793(3)	

TABLE IV.4f $B^2\Sigma^+ - X^2\Sigma^+(0,0)$
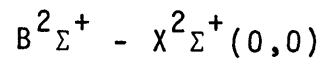
J"	R^e	Q^{fe}	Q^{ef}	P^f
0.5	88..638(6)	88.576(6)	88.498(5)	
1.5	88.638(6)	88.576(6)	88.369(3)	88.308(4)
2.5	88.585(4)	88.498(4)	88.189(6)	88.126(6)
3.5	88.484(5)	88.379(3)	87.958(6)	87.869(6)
4.5	88.332(6)	88.203(3)	87.683(3)	87.576(5)
5.5	88.126(6)	87.979(3)	87.353(3)	87.226(6)
6.5	87.858(6)	87.708(3)	86.970(5)	86.827(6)
7.5	87.563(5)	87.394(3)	86.538(6)	86.404(6)
8.5	87.219(6)	86.970(5)	86.055(6)	85.913(3)
9.5	86.827(6)	86.481(4)	85.542(5)	85.318(5)
10.5	86.383(6)			84.644(5)
11.5	85.889(6)			
12.5	85.361(6)			

TABLE IV.4g $\qquad$ B$^2\Sigma^+$ - X$^2\Sigma^+$(b,0)

J"	R^e	Q^{fe}	Q^{ef}	P^f
0.5	7007.193(5)	7007.187(5)	7007.131(6)	
1.5	7007.131(6)	7007.165(5)	7006.923(6)	7006.904(5)
2.5	7007.029(5)	7007.076(3)	7006.684(3)	7006.719(5)
3.5	7006.874(4)	7006.931(5)	7006.407(3)	7006.443(5)
4.5	7006.654(3)	7006.737(6)	7006.069(3)	7006.128(4)
5.5	7006.367(3)	7006.452(5)	7005.672(3)	7005.740(3)
6.5	7006.019(4)	7006.109(3)	7005.218(6)	7005.308(8)
7.5	7005.608(5)	7005.703(3)	7004.686(8)	7004.774(4)

related to the off-diagonal matrix elements of the rotational operator $B(r)$ taken between vibronic states of the $\Pi_{1/2}$ and $\Pi_{3/2}$ components, $\langle v_1'\Pi_{1/2}|B(r)|v_2'\Pi_{3/2}\rangle$. This type of interaction has been seen previously by Lefebvre-Brion, et al. in the $X^2\Pi$ state of NSe (JPL 73) and is observed in NaNe: $A^2\Pi_{1/2} - X^2\Sigma^+(6,0)$ perturbs $A^2\Pi_{3/2} - X^2\Sigma^+(4,0)$ near J' = 4.5. While this was the only crossing actually observed, line shifts and intensity anomalies suggest a similar perturbation between $A^2\Pi_{1/2} - X^2\Sigma^+$ (4,0) and $A^2\Pi_{3/2} - X^2\Sigma^+(3,0)$ at J' = 10.5. These overlapping bands have different relative intensities and account for the densest spectrum in the NaNe $A^2\Pi_r - X^2\Sigma^+$ system (~ 17 lines/cm^{-1}).

In NaAr the $A^2\Pi_{1/2} - X^2\Sigma^+(16,0)$ and (17,0) bands (at 30.270(8) and 33.980(5) cm^{-1} blue of the D_2 line) are anomalously intense ($\sim 10^3$ counts), considering the Franck Condon factor for these transitions is $\sim 10^{-7}$. However, since these two states interact strongly with the $B^2\Sigma^+$ state (the $B^2\Sigma^+$, b' = 0 level being very close) these $A^2\Pi$ states may borrow oscillator strength from the $B^2\Sigma^+$ state and will be seen especially if the $B^2\Sigma^+ - X^2\Sigma^+(0,0)$ band is strong. This band, as mentioned above, is the most intense spectral feature blue of the D_2 resonance line.

The $B^2\Sigma^+$, b' = 0 level is sandwiched, in fact, between the $A^2\Pi_{1/2}$ v' = 16 and 17 levels (see Fig.d.2). The
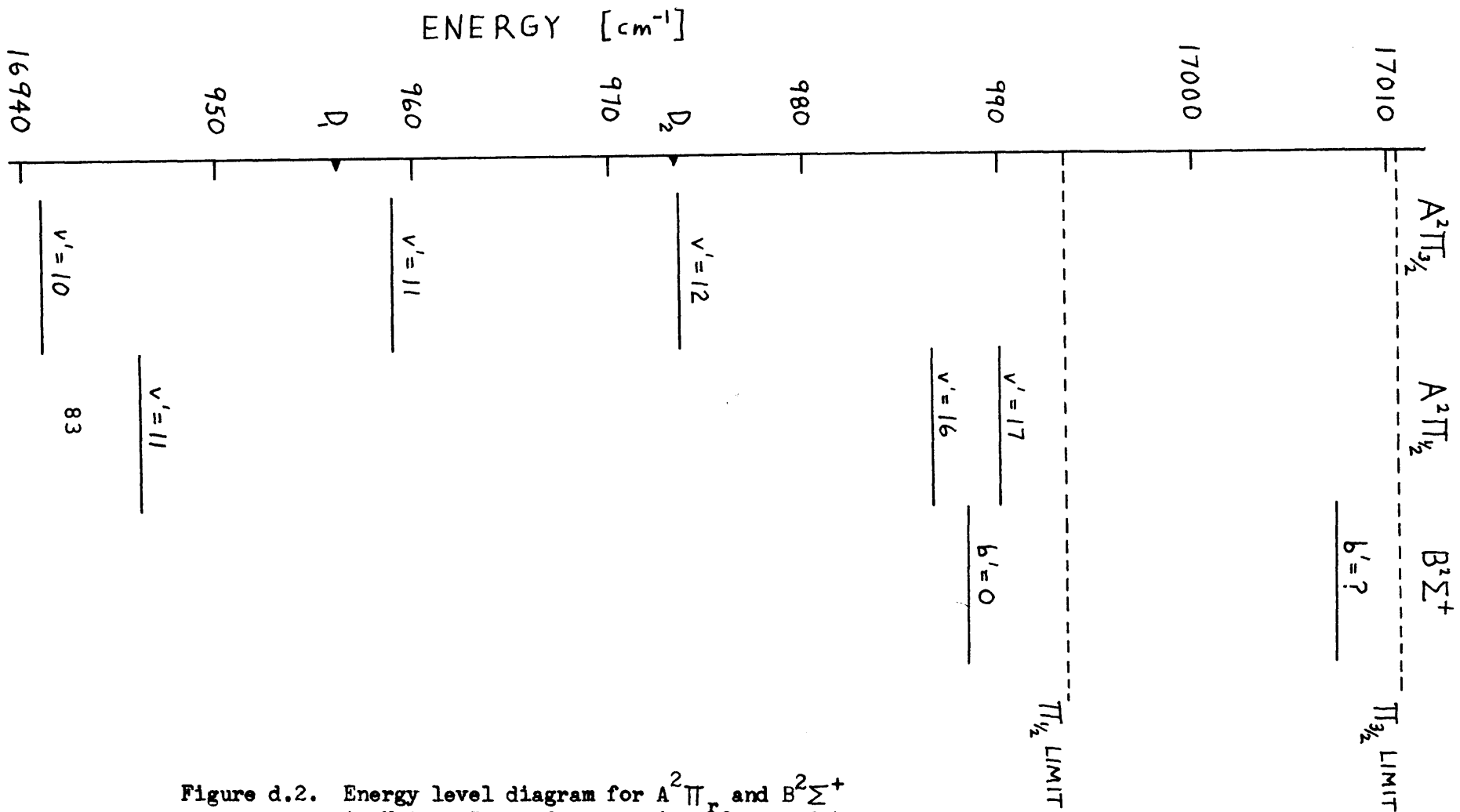
Figure d.2. Energy level diagram for $A^2\Pi_r$ and $B^2\Sigma^+$ in NaAr. Zero of energy is referenced to $v''=0$ level in the ground state.

Λ-doubling (splitting of e and f levels) normally present in the $\Pi_{1/2}$ state is usually ascribed to perturbations from $B^2\Sigma^+$ states lying <u>above</u> the $\Pi_{1/2}$ states. The perturbation is second order and varies inversely as the energy separation between $\Pi_{1/2}$ and Σ levels, growing larger with increasing v' as observed (LAM 80, SAF 77). With the Σ level between v' = 16 and 17, one expects the magnitude of the Λ-doubling constant to decrease from level v' = 16 to v' = 17, and this is observed (see Table IV.3).

Several lines remain unassigned in the NaNe spectra. In particular, a group of lines ⌄13.4 cm^{-1} red of the D_2 line appears to be a red degraded band with a small rotational constant. This band is red shifted by <7.5 cm^{-1} from the band origin of the strongest NaNe feature: $A^2\Pi_{3/2}$ - $X^2\Sigma^+$(5,0). The observed shift (greater than the ground state vibrational spacing) implies that this cannot be the hot band, $A^2\Pi_{3/2}$ - $X^2\Sigma^+$(5,1). Though we have no consistent assignment, this band is probably $A^2\Pi_{1/2}$ - $X^2\Sigma^+$(7,0) which is predicted by a crude long range analysis to be red degraded, occurring ⌄12.8 cm^{-1} red of the D_2 line.

C. <u>LONG RANGE ANALYSIS AND VIBRATIONAL ASSIGNMENT</u>

NaNe and NaAr are appropriate systems for studying long

range forces. Because the ground Σ state equilibrium inter-nuclear separation is approximately twice that of the exicted Π state, Franck-Condon factors favor excitation of high $A^2\Pi_r$ vibrational levels - some within 3 cm^{-1} of disso-ciation. Consequently, the term values obtained are better analyzed with long range theories (LEB 70) than with a Dun-ham expansion (DUN 32), which is based on an expansion of the potential about its minimum.

The long range analysis (LRA) method (LER 73) is based on two assumptions: (1) the long range [V(R) for large R] part of the interatomic potential predominately determines the distribution of levels near the dissociation limit of a diatomic molecule; and (2) this portion of the potential has the form $V(R) = C_n R^{-n}$. This approximation is justified by the fact that the inner wall of the potential is quite steep and therefore the wavefunctions and radial probabilities are large only at large internuclear distances corresponding to v' near dissociation. Application of the long range analysis to NaNe and NaAr is appropriate, not only because levels close to dissociation are accessed in the experiment, but also because these are van der Waals molecules bound by long range electro-static forces (which obey a power law).

If two neutral atoms with a least one in an S-state, are sufficiently far apart that their electron cloud overlap

is negligible, the interaction potential in the long-range

region can be written as $V(R) = D-C_6/R^6-C_8/R^8-C_{10}/R^{10}$

+ ...., where D is the dissociation energy relative to the

well minimum. At long range one power of R will usually

dominate and the potential can be approximated as $V(R) = D -$

C_n/R^n, where n is non integral in general, but approximately

equal to six. The asymptotic rotationless vibrational

eigenvalues, $G(v, J=0)$, corresponding to integer values of

v, and the rotational constant, B_v, for the above potential

(LER 73) are given by

(4.8) $G(v) = D-[(v_D-v)H_n]^{2n/n-2}$, and

(4.9) $B_v = Q_n(v_D-v)^{4/n-2}$.

H_n and Q_n are constants depending only on the molecular

reduced mass μ, and the potential energy expansion coeffi-

cients C_n. v_D is the non-integral vibrational quantum

number at dissociation.

For n = 6, the eigenvalues G(v) and the rotational con-

stant B_v can be represented by

(4.10) $G(v) = D-[(v_D-v) H_6]^3$

(4.11) $B_v = Q_6 [v_D - v]$

where $H_6 = (19.95336) \mu^{-1/2} C_6^{-1/6}, Q_6 = 546.658 \mu^{-3/2} C_6^{1/2}$. [Units of energy, length, and mass are taken to be cm^{-1}, Å and a.m.u. respectively.]

Effective utilization of the long range formulae (Eqs.(4.10) and (4.11) requires a knowledge of the absolute vibrational numbering. Without such knowledge, incorrect vibrational assignments, $v \pm n$ (for n integer), change the v_D to $v_D \pm n$ and hence change other predictions made by the formulae. For NaAr the vibrational numbering has been established by a dispersed fluorescence experiment (TRK 79). However, no such experiment has been done on NaNe and the correct vibrational numbering of the observed spectra is achieved by utilizing these asymptotic formulae for the vibrational energy near dissociation (long range formulae, LEB 70) and observed isotopic bands.

Equation (4.10) can be expressed in terms of the observed molecular band origins, v_{vo}, of $A^2\Pi_{3/2} - X^2\Sigma^+$ (v, 0) measured relative to the atomic sodium transition $v(^2S_{1/2} \rightarrow {}^2P_{3/2})$, and the X-state dissociation energy, D_{oX} (see Fig.d.3)

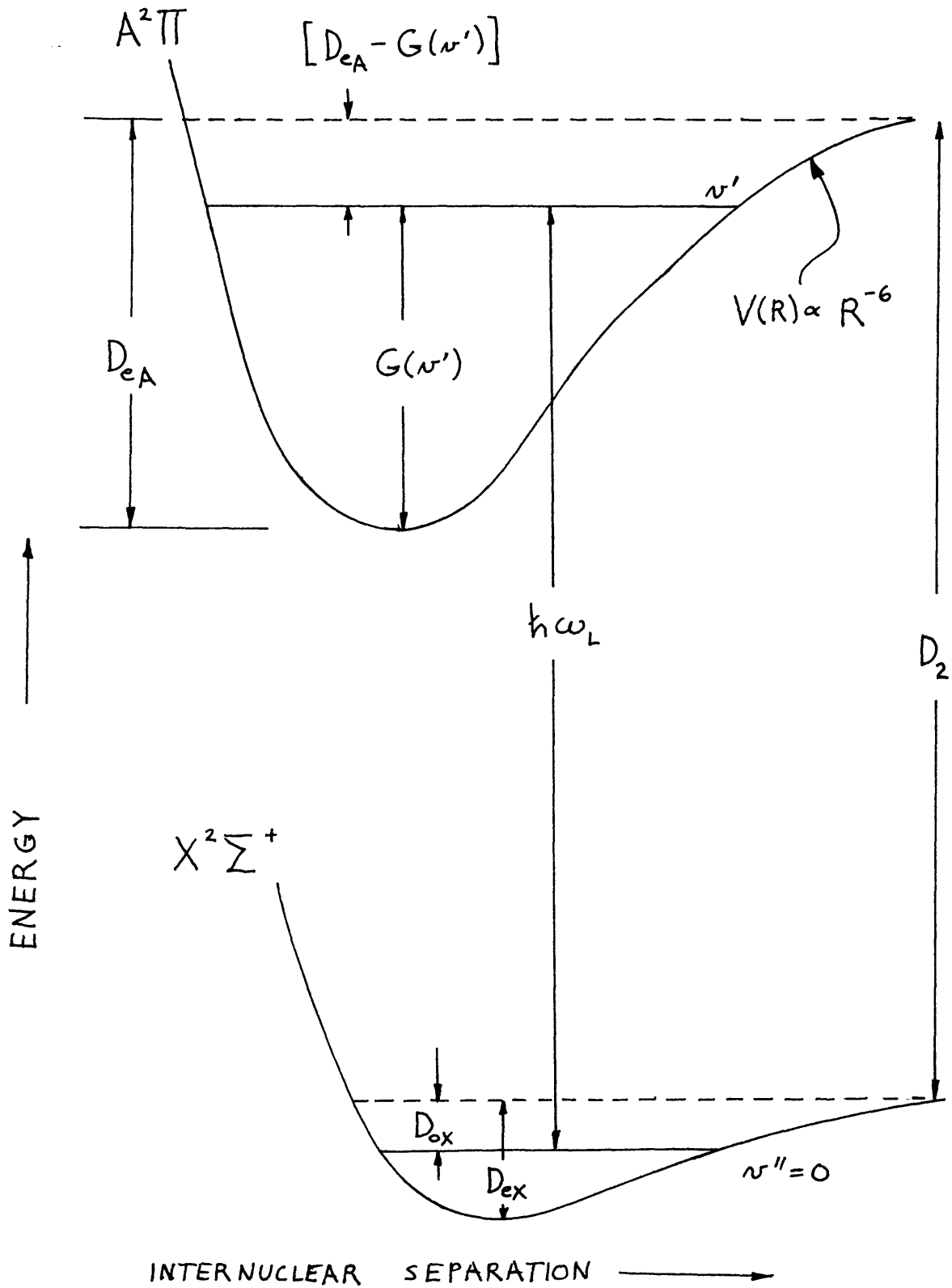(4.12) $[D_{oX} - v_{vo}]^{1/3} = H_6 [v_D - v]$

Figure d.3. Schematic illustrating the parameters
used in the long range analysis.

The band origins used in Eq.(4.12) are rotationless band origins. These are derived from observed rotational transitions by addition or subtraction of appropriate ground and excited state differences:

$$(4.13a) \qquad \nu_o = R_2^f(\emptyset.5) + 2(B" - B'_{eff}) \text{ for } \pi_{3/2}$$

$$(4.13b) \qquad \nu_o = Q_{21}^{fe}(\ell.5) - B'_{eff} \text{ for } \pi_{1/2}$$

where $B'_{eff} = B'(1 \pm B'/A)$. $B"$ and B' are the rotational constants for the ground and excited states respectively, A is the spin orbit splitting, and the $+(-)$ sign is taken for the $\pi_{3/2}(\pi_{1/2})$ component.

Fitting the data to these long range formula (Eq.(4.12) and (4.11) allows determination of the excited A-state well depth, D_{eA}, the dissociation energy of the ground state, D_{oX}, and estimates for C_6, the van der Waals coefficients. The long range analysis may also be applied to the $B^2\Sigma^+$ state if D_{oX} is held fixed at the value determined from the LRA of the $A\pi$ state.

The long range analysis as applied to NaNe has been discussed thoroughly in the literature (AHB 77, ALP 77, LAM 8$\emptyset$). The results are shown in Fig.d.4 and summarized in
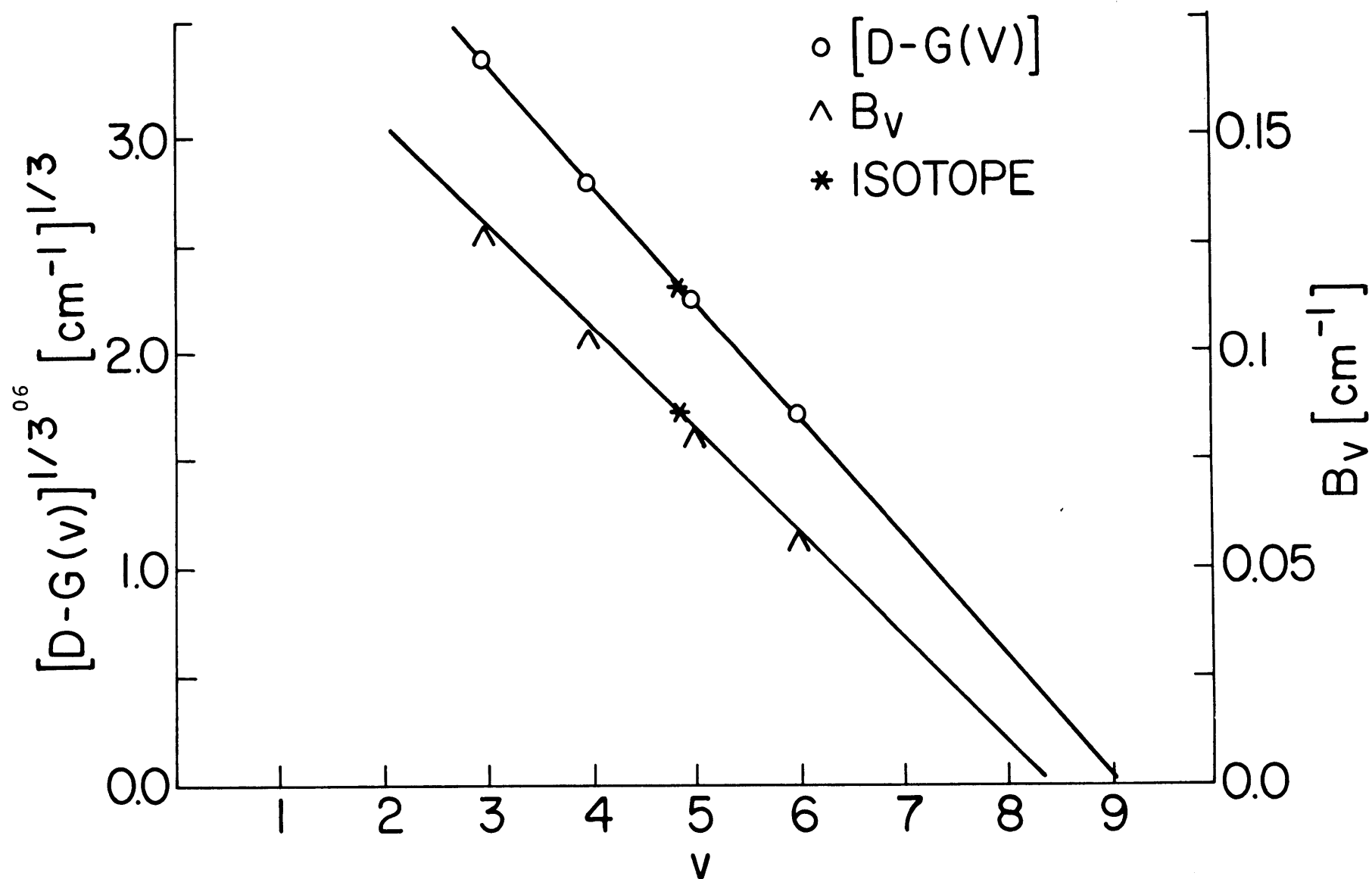
Figure d.4

Long range analysis of NaNe

Table IV.6.

The vibrational numbering of NaNe (ALP 77) has been questioned (TRK 79), and recent re-analysis by Bitar (AHB 79) of a portion of the NaNe spectrum revealed a second isotopic band, $A^2\Pi_{1/2} - X^2\Sigma^+$ (4*,∅) 12.298(3) cm^{-1} red of the D_1 line. This band, and the previously known isotopic band, $A^2\Pi_{3/2} - X^2\Sigma^+$ (5*,∅), permits unambiguous confirmation of the previous vibrational assignment using the following technique.

Assuming the spin orbit constant is isotopically independent, the position of $A^2\Pi_{3/2} - X^2\Sigma^+$(4*,∅) can be predicted.

$$(4.14) \qquad ^{22}\nu_{4,\varnothing}^{3/2} = {}^{22}\nu_{4,\varnothing}^{1/2} + ({}^{2\varnothing}\nu_{4,\varnothing}^{3/2} - {}^{2\varnothing}\nu_{4,\varnothing}^{1/2})$$

$$= 16955.914 \text{ cm}^{-1}$$

This band is not observed because of the much stronger overlapping $A^2\Pi_{3/2} - X^2\Sigma^+$(5,∅), $A^2\Pi_{1/2} - X^2\Sigma^+$(4,∅), and D_1 line. Equation (4.12) may be written,

$$(4.15) \qquad [^iD_{ox} - {}^i\nu_v] = [^iH_6({}^i\nu_D - \nu)]^3$$

for any ν, and where i indicates either isotope, with $\nu'' = ∅$

understood. Equation (4.15), and a similar equality where v

→ v + 1 gives two equations which can be subtracted to give

$$(4.16) \qquad \frac{{}^i\nu_{v+1} - {}^i\nu_v}{{}^iH_6^3} = 3({}^i\nu_D - v)^2 - 3({}^i\nu_D - v) + 1$$

By inserting the band origins ${}^{22}\nu_{4,0}{}^{1/2}$, ${}^{20}\nu_{4,0}{}^{3/2}$,
${}^{22}\nu_{5,0}{}^{3/2}$, and ${}^{20}\nu_{5,0}{}^{3/2}$ and ${}^{20}H_6 = 0.5446$ from the long
range fit, two equations are obtained

$$(4.17a) \qquad 63.124 = 3x^2 - 3x + 1$$

$$(4.17b) \qquad 70.031 = 3y^2 - 3y + 1$$

where $x = {}^{20}\nu_D - v$ and $y = {}^{22}\nu_D - v$. These two equations
can be solved for x and y; and, since ${}^{22}\nu_D$ is related to
${}^{20}\nu_D$ (LER 70),

$$(4.18) \qquad {}^{22}\nu_D = \rho^{-1} ({}^{20}\nu_D + 0.5) - 0.5; \ \rho = \sqrt{\mu/\mu_i}$$

Two linear equations in two unknowns v and v_D result

$$(4.19a) \qquad 5.078 = {}^{20}\nu_D - v$$

$$(4.19b) \qquad 5.323 = {}^{20}\nu_D/\rho + 0.5(\rho^{-1}-1) - v$$

The solution of this system of linear equations is $v = 4.128$ and $^{20}v_D = 9.206$. This agrees well with the previous assignment $v_o+1=4$ and $v_o+2=5$, (ALP 77).

The long range fit to the NaAr $A^2\Pi_{3/2}$ data is simplified since the vibrational numbering is known. D_{oX}, in Eq.(4.12), is varied to obtain the best (minimum Chi-squared) straight line fit of $[D_{oX} - \nu_{vo}]^{1/3}$ versus v (Fig.d.5). The value determined in this way is $D_{oX} = 37.3$ cm^{-1}. The straight line fit to the data intersects the v axis, predicting the non-integral dissociation quantum number of $v_D = 20.53$. If the fit is extrapolated back to $v = -1/2$, the $A^2\Pi$ well depth is obtained, $D_{eA} = 556.9(1.2)$ cm^{-1}. The slope of the line (H_6) is related to the C_6 coefficient

$$(4.19) \qquad H_6 = \frac{19.94336}{\mu^{1/2}C_6^{1/6}}$$

where $\mu = 14.5921$ a.m.u. (NaAr-CRC 72) the reduced mass, and the numerical constant is the ratio of some Gamma functions (LER 70). In this case, the van der Waals coefficient for the $A^2\Pi$ state is $C_6 = 5.594 \times 10^6 cm^{-1} \text{Å}^6$. Included in this fit were all available $\Pi_{3/2}$ levels, namely $v' = 7, 8, 9, 10, 11, 12$. The convergence parameter for the fit is $r^2 =$
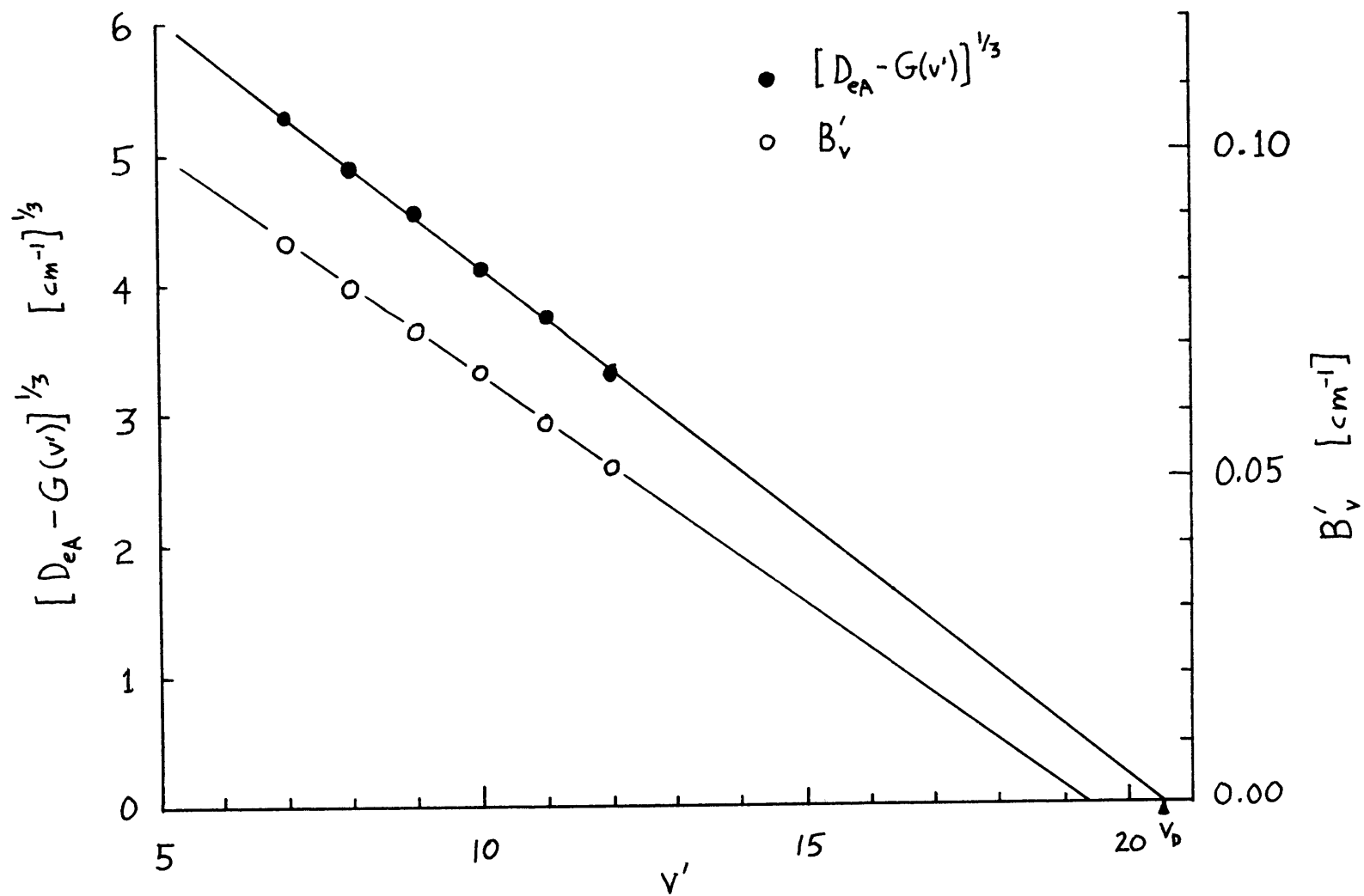
Figure d.5. Long range analysis of NaAr.

0.999998.

A fit to all the rotational constants for $A^2\Pi_{3/2}$ levels
$v' = 7$ through 12 according to Eq.(4.11) was also done (see
Fig.d.5). This plot is also extrapolated to $v' = - 1/2$ and
yields a value for the equilibrium rotational constant, $B_e =$
$0.13897(57)$ cm^{-1}. This molecular constant is related to the
internuclear equilibrium separation R_e,

$$(4.20) \qquad B_e = \frac{\hbar}{4\pi c \mu R_e^2} \rightarrow R_e = \frac{7.758}{\sqrt{\mu B_e}} [a_0]$$

with B_e in cm^{-1}, $\hbar$ is Plancks constant and c is the speed of
light. Hence, $R_{eA} = 5.448(22)$ a_0.

As a comparison, a traditional Birge Sponer plot (HER
50) for the NaAr $\Pi_{3/2}$ data was done (Fig.d.6), and the dis-
sociation energy estimated by summing over the straight line
extrapolated vibrational intervals.

$$D_{eA} \simeq \sum_{v'} \Delta G_{v'+1/2} = \sum_{v'} G(v'+1) - G(v') = 5 \ 17 \text{cm}^{-1}$$

The extended straight line fit also predicts a dissociation
quantum number $v_D = 15.05$.

It is not possible to identify transitions to the $B^2\Sigma^+$
states solely by the presence of weak Q branches. Because
$B^2\Sigma^+$ mixes so strongly with $A^2\Pi_{1/2}$, $B^2\Sigma^+ - X^2\Sigma^+$ frequently
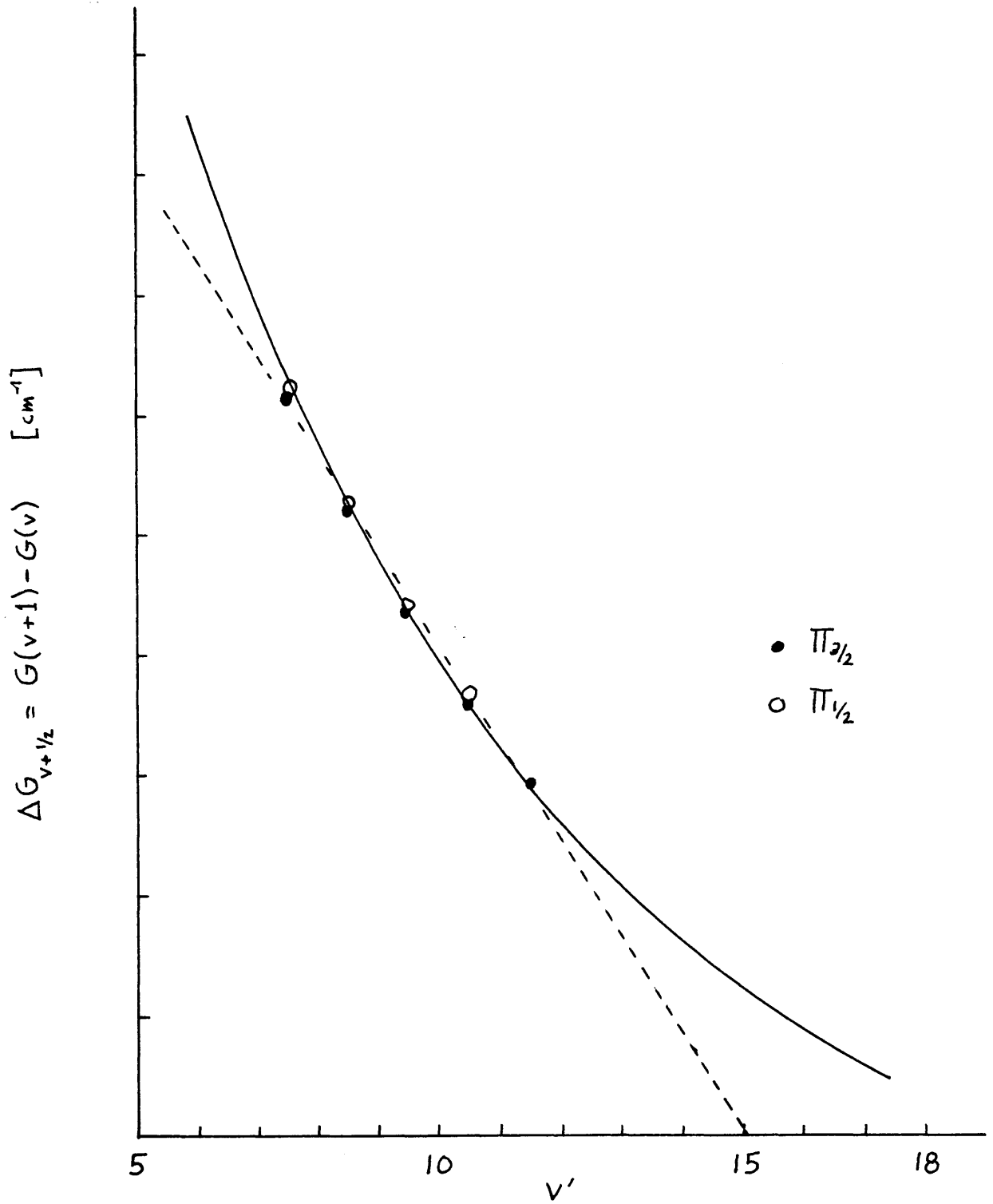
$$\Delta G_{v+\frac{1}{2}} = G(v+1) - G(v) \quad [\text{cm}^{-1}]$$

$\bullet \quad \Pi_{3/2}$

$\circ \quad \Pi_{1/2}$

v'

Figure d.6. Traditional Birge Sponer plot: NaAr.

96

looks like $A^2\Pi_{1/2} - X^2\Sigma^+$ (see Fig.b.6). Further, in the long range region (large R), near the $B^2\Sigma^+$ well minimum (where any bound states must be located) the spin orbit operator is larger than the likely binding energy so that a $|J_\alpha = \frac{3}{2}, \Omega = \frac{1}{2}\rangle$ designation is probably more appropriate. Nevertheless, it is possible to identify these transitions by long range analysis where two characteristics are apparent: the values of $G(v)$ for high vibrational $A^2\Pi_{3/2}$ levels will not correspond generally to the observed $G(b)$ of the $B^2\Sigma^+$ levels; and, the value of the rotational constant for a $B^2\Sigma^+$ level with a particular $G(b)$ will be smaller than the value expected if the level were bound by the $A^2\Pi_{3/2}$ potential.

Combining Equations (4.10) and (4.11) gives

$$(4.21) \qquad [D - G(v)]^{1/3} = \frac{H^6}{Q_6} B_v$$

which can be used to plot the band origins versus rotational constants, without knowing the absolute vibrational numbering. A plot of Eq.(4.21) for data corresponding to the $\Pi_{3/2}$ manifold in NaNe and NaAr is shown in Figs.d.7 and d.8. The observed $B^2\Sigma^+ - X^2\Sigma^+$ bands provide points that do not lie on the line as would be expected if these bands were $A^2\Pi_{3/2}$ –
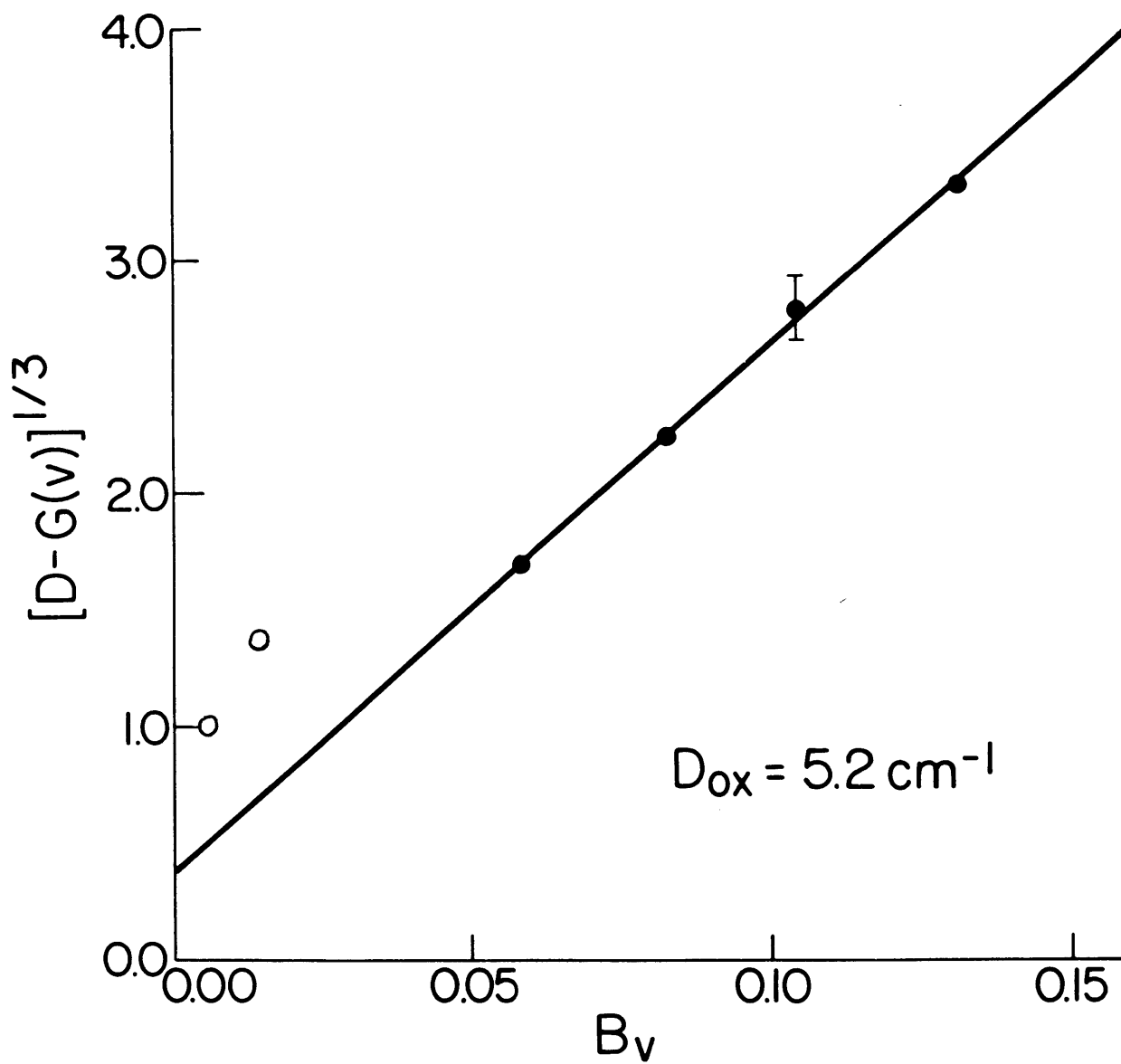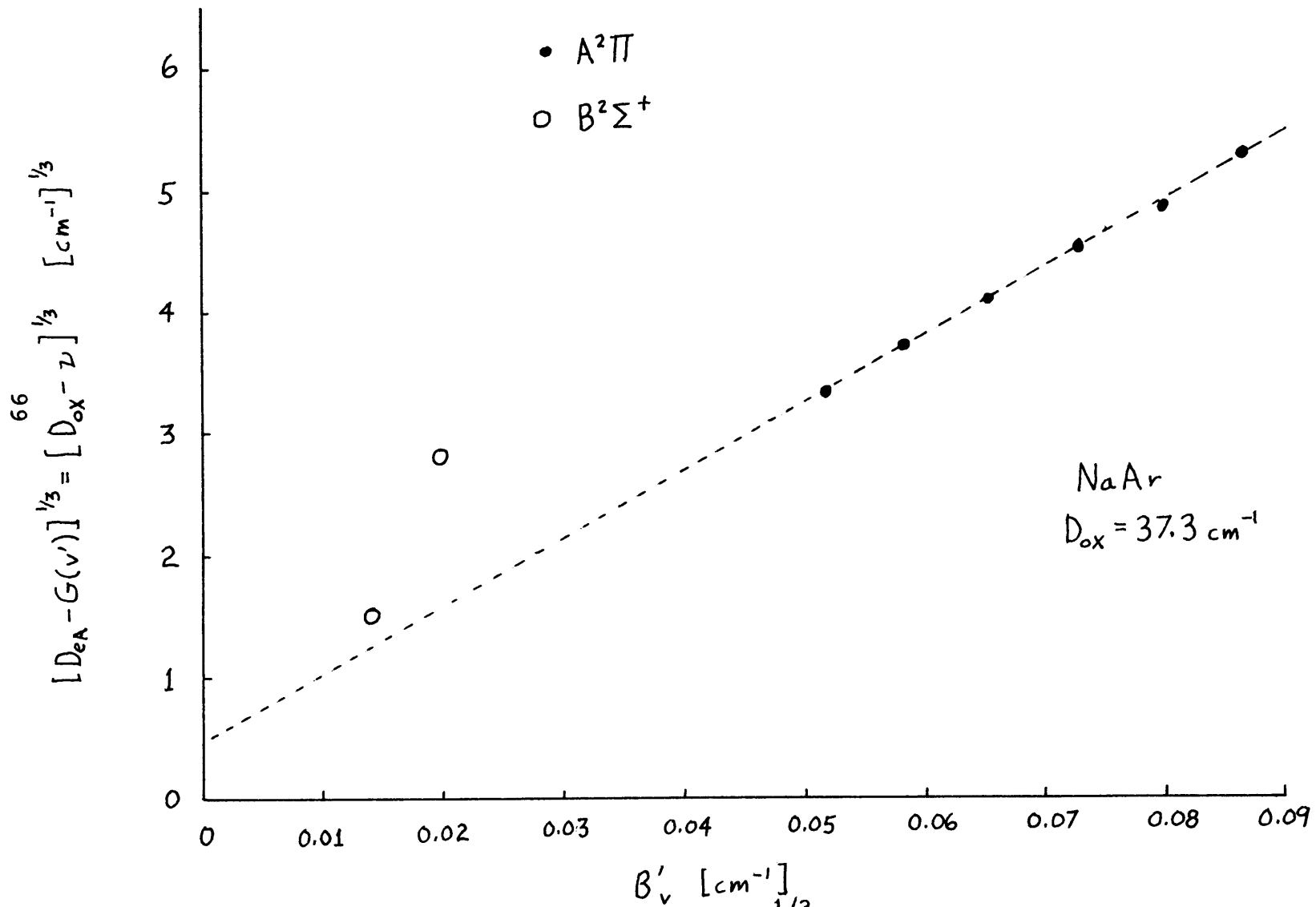
Figure d.7

B' vs. (D-G)$^{1/3}$ for NaNe

Figure d.8. B' vs. (D-G)$^{1/3}$ for NaAr.

$X^2\Sigma^+$.

Equations (4.10) and (4.11) are used to predict values
of the rotational constant and band origin for NaNe
$A^2\Pi_{3/2} - X^2\Sigma^+(7,0)$. We estimated $B_7 = 0.03432$ cm^{-1} and the
band origin, $^{20}\nu_{07} = 3.66$ cm^{-1}. This predicted rotational
constant is 0.021 cm^{-1} larger than B_v observed for the
$B^2\Sigma^+ - X^2\Sigma^+(b,0)$.

The absolute vibrational numbering of the observed
$B^2\Sigma^+ - X^2\Sigma^+$ transitions is uncertain, however these bands
originate from $v'' = 0$ because ground state difference match
(see rotational analysis section).

In NaNe, a long range analysis performed for different
guesses for the value of b, yielded reasonable results for a
value, $b = 0$: $D_{eB} = 3.575$ cm^{-1} at $R_{eB} = 18.5(5)a_o$. An
attempt to scale the $B^2\Sigma^+$ well depth in NaNe (knowing D_{eA}
and D_{eX}) to the calculated D_{eB} in NaAr (SOL 77, assuming
D_{eB}/D_{eA} is the same in both systems) yielded $D_{eB} \simeq 4.65$cm^{-1}.
Comparison of calculations with experimental predissociation
linewidths (GLF 80) affirms the $b = 0$ assignment. The $B^2\Sigma^+$
well depth is therefore estimated to be $D_{eB} = 3.6(7)$ cm^{-1} at
$R_{eB} = 18.5(5)a_o$, assuming the bands seen are $B^2\Sigma^+ - X^2\Sigma^+$
(0,0) and (0,1).

The $B^2\Sigma^+ - X^2\Sigma^+$ transition of NaAr nearest the D_2 line
is assumed to be the (0,0) band, since it is more intense

TABLE IV.5. Long range analysis of $B^2\Sigma^+$. The ground state dissociation energy is fixed at $D_{OX} = 37.3$ cm^{-1} (determined from $A^2\Pi_{3/2}$ LRA). The results below are calculated assuming the first level seen is b' = 0. The vibrational numbering indicated refers to the second observed level (1 a_o = .529Å)

vibrational numbering	D_{eB} [cm^{-1}]	R_e [a_o]	C_6 [cm^{-1} a_o^6]
1	41.1	13.1	2.025×10^5
2	30.6	13.6	1.296×10^7
3	27.6	13.7	1.476×10^8
4	26.2	13.8	8.298×10^8
5	25.3	13.9	3.164×10^9

than any of the other spectral features in the area – in agreement with the expected large Franck Condon factor for this transition. A long range analysis has been done on the $B^2\Sigma^+$ (fixing D_{oX} at its predetermined value), and the results for various vibrational numberings of the second band are presented in Table IV.5. A vibrational numbering of b = 1 indicates a deeper well than expected, and a smaller C_6. An assignment of b = 2 is reasonable from qualitative consideration of Franck Condon factors, but again produces a small C_6. The assignment which looks most reasonable is b = 4 or 5. This predicts a well depth such that $D_{eB} < D_{eX}$, as in NaNe, and a reasonable C_6. Further, the three observed, but unanalyzable bands (overlapped with dimers) between the (0,0) and (b,0) band (see section B), are probably $B^2\Sigma^+ - X^2\Sigma^+$ as $\Pi_{1/2}$ bands are not allowed energetically in this spectral region. The listing in Tables IV.7 and IV.6 is for an assignment of b = 4.

D.   DEPERTURBATION ANALYSIS

The deperturbation analysis is a non-traditional fitting of the data to a model Hamiltonian in order to extract molecular parameters which provide consistent, meaningful constants within the context of the model. The model Hamiltonian is described in Appendix B and the literature (FIE

102

TABLE IV.6 Molecular potential parameters. Well depths
(D_e's) are given in [cm^{-1}] and equilibrium
separation (R_e's) in [a$_o$]. Errors in last
significant digits are quoted in parenthesis.

MOLECULE	PARAMETER	THEORY	EXPERIMENTAL		
NaNe		MPV 78	ALP 77	LAG 80	
	D_{eX}	7.8	8.1(9)	8.1(9)	
	R_{eX}	10.	10.0(2)	10.0(1)	
	D_{eX}	132	140(3)	145(5)	
	R_{eA}	5	5.1(1)	5.1(1)	
	D_{eB}			3.6(7)	
	R_{eA}			18.5(5)	
NaAr		SOL 77	SAF77	TRK 79	This Work
	D_{eX}	51.8	39(2)	40.4(1.0)	43.8(2.0)
	R_{eX}	10.0	9.435(4)	9.435(4)	9.43
	D_{eA}	484.3		558.6	556.9(1.2)
	R_{eA}	5.75		5.495	5.448(22)
	D_{eB}	31.5			26(3)
	R_{eB}	13.0			13.8(2)

TABLE IV.7.   Tablulation of C_6 coefficients. The experimentally determined values are indicated under LRA (long range analysis). Other values reported in the references indicated are theoretically determined. Values calculated from equations (2-14) are also reported. Units are $[cm^{-1} \, a_0^{\,6}]$, errors (in the last significant digits) where available are quoted in parenthesis.

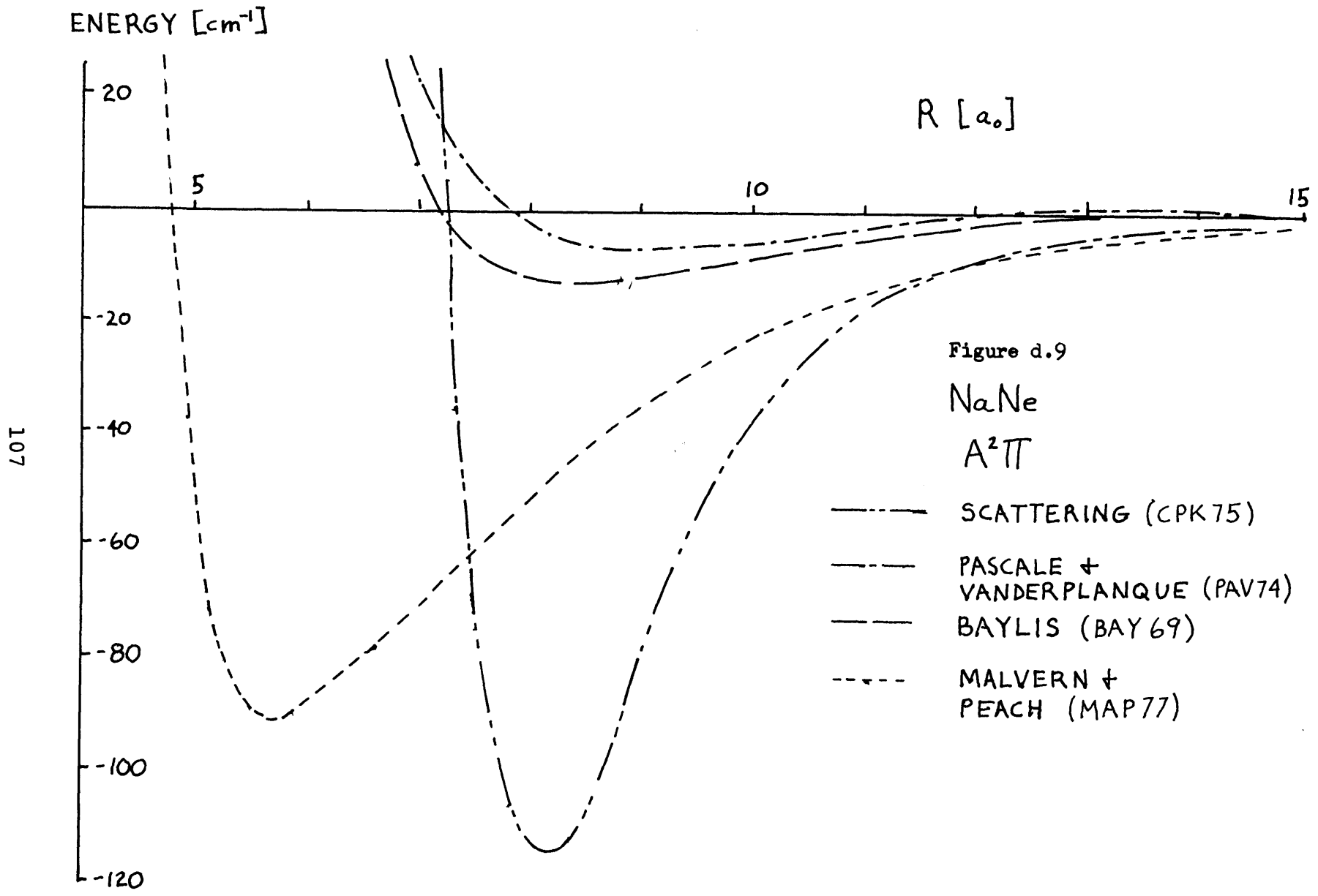| MOLECULAR STATE	LRA	TAT 77	PRS 77	EQ(2-14)
NaNe: $X^2\Sigma^+$		1.030×10^7	$1.015(12) \times 10^7$	1.036×10^7
$A^2\Pi_r$	8.989×10^7			
$B^2\Sigma^+$	1.520×10^9			
NaAr: $X^2\Sigma^+$	1.546×10^8	4.082×10^7	$4.08(12) \times 10^7$	4.170×10^7
$A^2\Pi_r$	2.553×10^8			
$B^2\Sigma^+$	8.298×10^8			

76, GOT 79).

Two bands $A^2\Pi_{3/2}$ - $X^2\Sigma^+$(11,0) and (12,0), in the newly seen NaAr spectra have been fit. The results of the computer fit are compared to experimentally determined constants in Table IV.3. The matrix size (rank) was 4 x 4, eight parameters were varied to fit 83 lines, and the variance of the fit was 0.7 indicating the data fit the model better than our experimental precision (0.003 cm^{-1}).

Fitting the other observed bands in NaAr requires modification of the computer programs to increase the dimension of the Hamiltonian. These fits are in progress, and a complete deperturbation analysis of NaAr will be published when it is available.

Additional computer programs (GOT 79) were used to generate RKR potential energy curves for the $A^2\Pi_r$ states in both molecules. The $X^2\Sigma^+$ potentials in NaAr and NaNe were constructed using model potentials (ALP 79, SAF 77) which reproduced the ground state energy level structure, and the data. In addition, Franck Condon factors were computed using these potentials (see Appendix E and GLP 80).

Comparison of the potential energy curves derived from the data, and various theories and experiments are presented graphically in Figs.d.9 through d.13. The well depths and equilibrium separations are tabulated in Table IV.6. Also,

a comparison of the C_6 coefficients, theoretical and extracted from the data, is presented in Table IV.7.

ENERGY [cm⁻¹]

R [a₀]

Figure d.9

NaNe

A²Π

—··— SCATTERING (CPK75)

—·— PASCALE + VANDERPLANQUE (PAV74)

—— BAYLIS (BAY69)

---- MALVERN + PEACH (MAP77)

107

Figure d.10
Na Ne
A²π

RKR
THEORY (MPV78)
+ LRA

ENERGY [cm^{-1}]

R [a$_o$]

Na Ne
X$^2\Sigma^+$

―――― SPECTROSCOPY (ALP77, LAG80)

― ― ― SCATTERING (CPK75)

―・― PASCALE +
VANDERPLANQUE (PAV74)

------- MALVERN +
PEACH (MAP77)

Figure d.11

109

Figure d.12

NaAr $A^2\Pi$

△ BAY 69

o PAV 74

• SOL 77

+ LRA

---- RKR

Figure d.13

NaAr $X^2\Sigma^+$

△ BAY 69   ✳ SAF 77

○ PAV 74   ⊘ TRK 79

• SOL 77

+ LRA
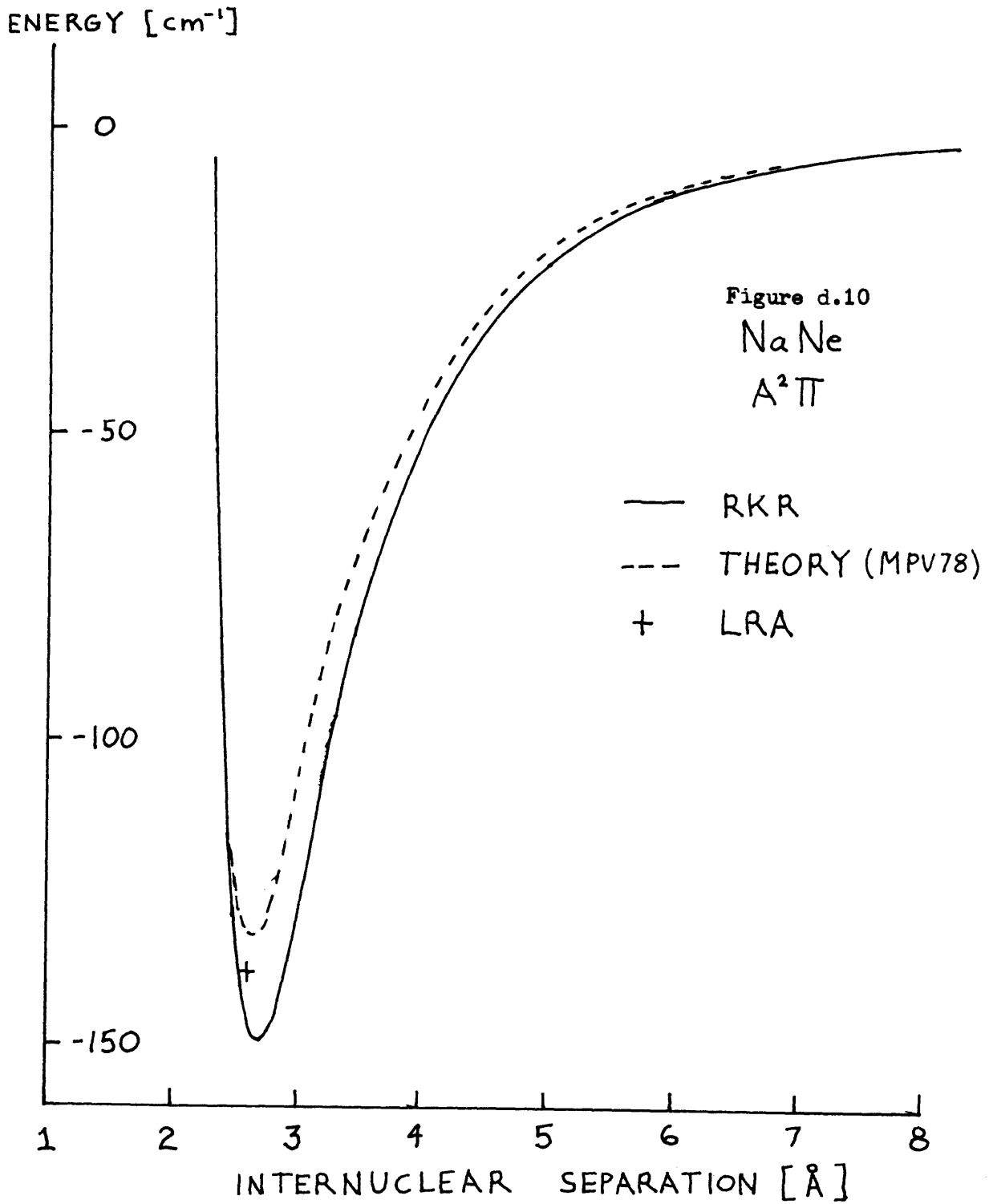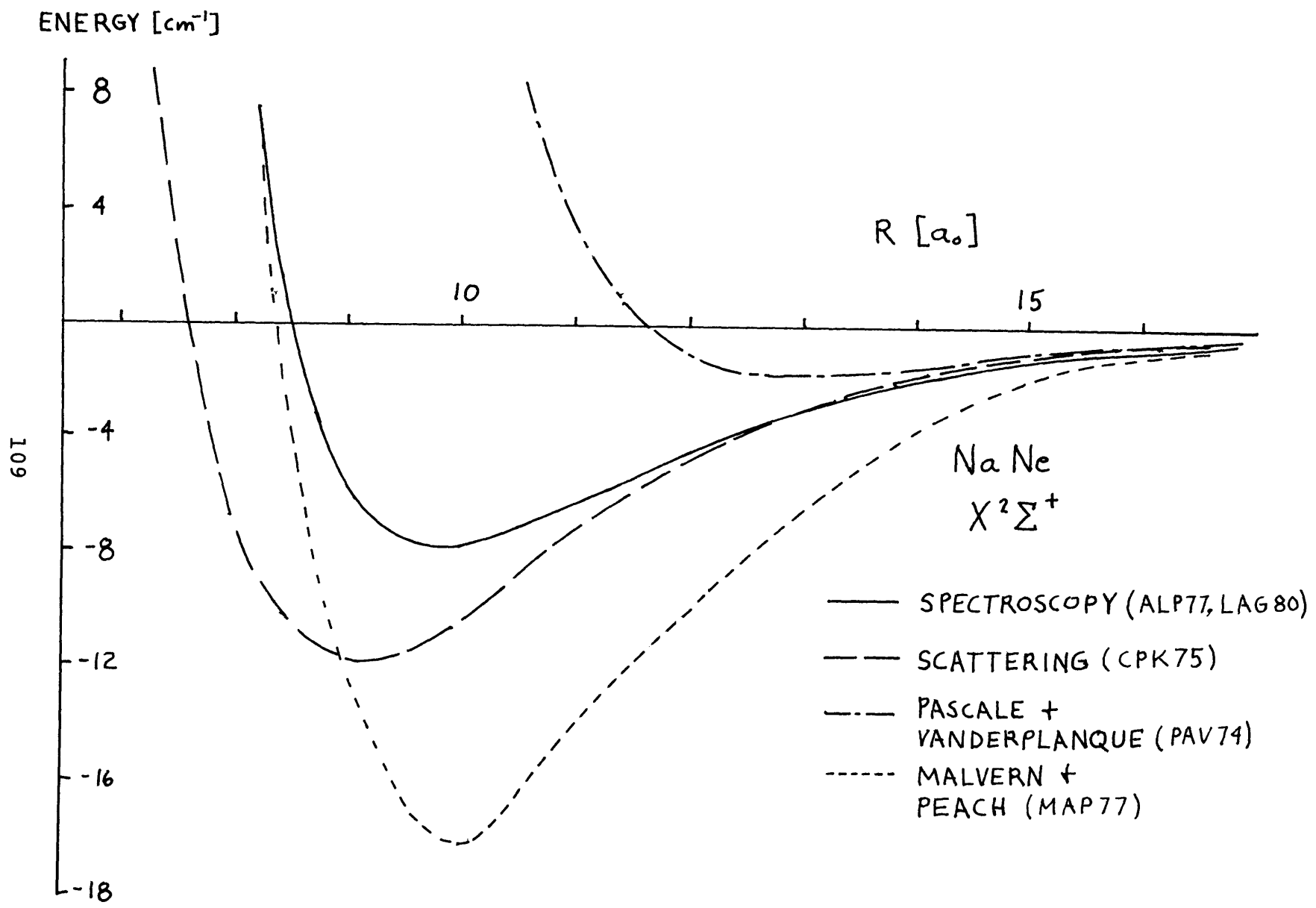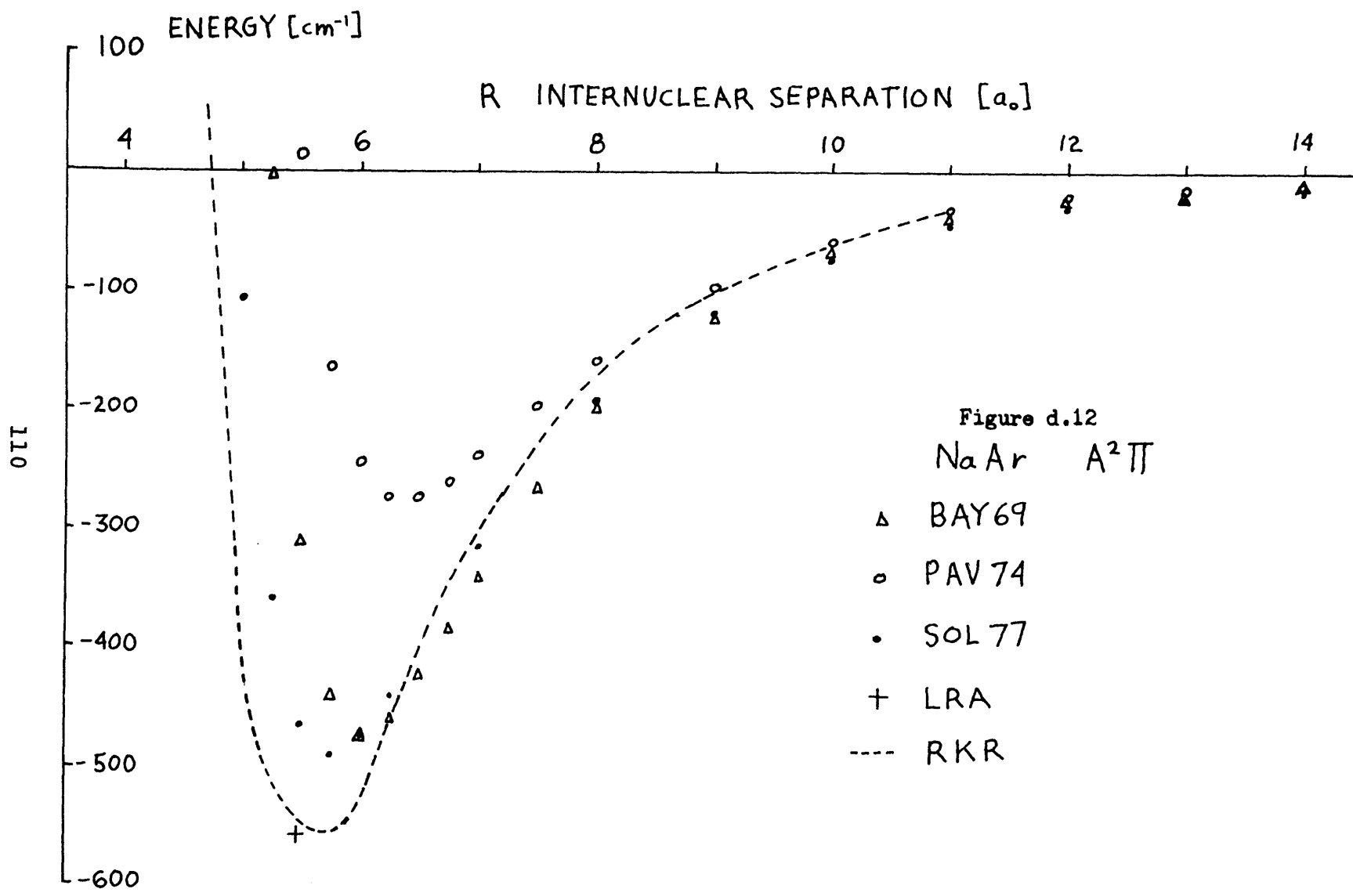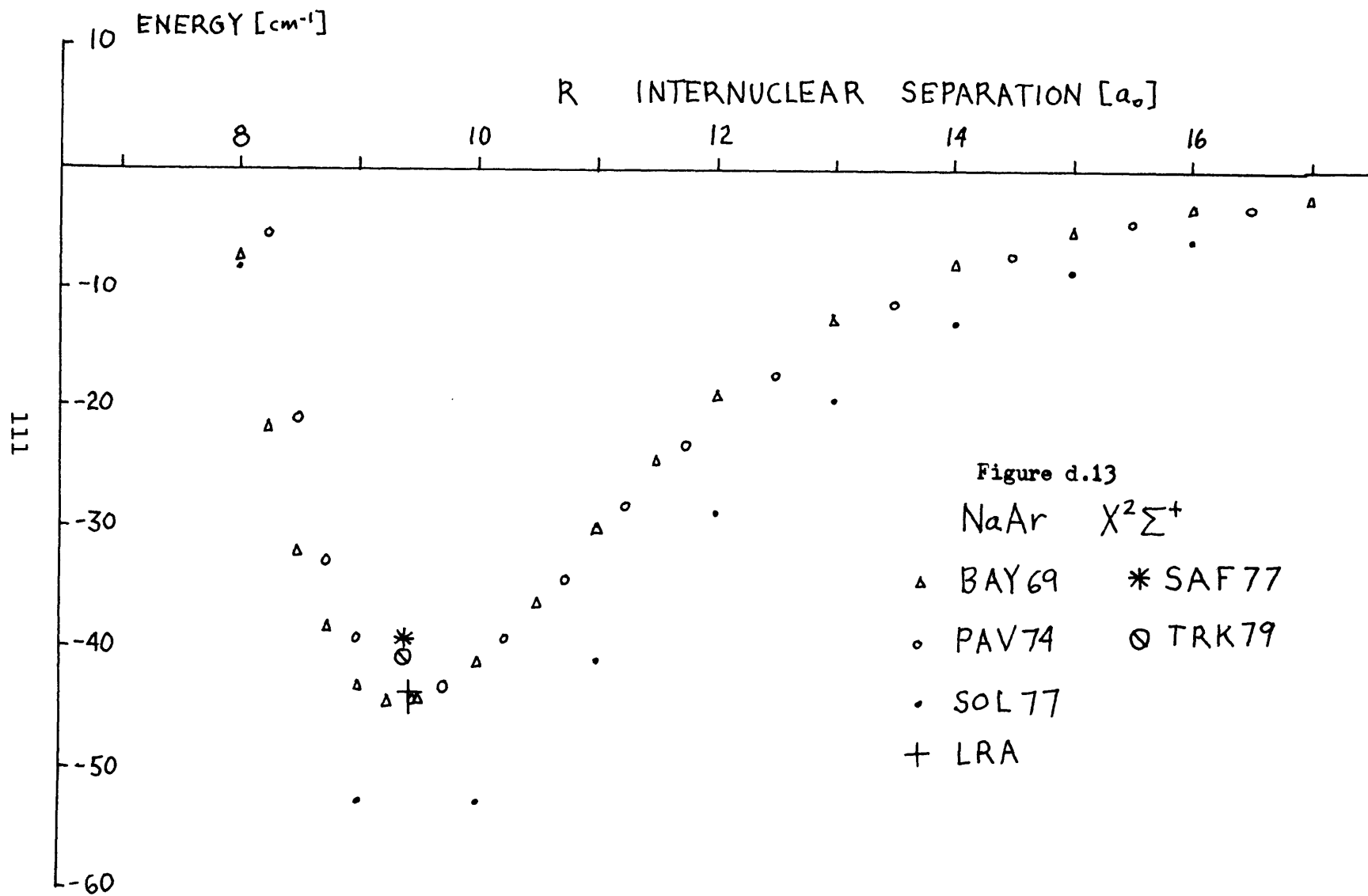
TABLE II.1. Parameters used to evaluate van der Waals coefficients
(eqn. 2-14) for NaNe and Na Ar systems (MAR 69). The
oscillator strengths connect the ground and first excited
states of the atoms indicated

Atom	Polarizability α $[a_o]^3$	Excitation energy E [eV]	Oscillator strength f
Na	167.53	2.12	0.975
Ne	2.671	21.559	2.37
Ar	11.101	15.755	4.58

Figure d.14

NaAr $B^2\Sigma^+$

△   BAY 69

○   PAV 74

•   SOL 77

+   LRA
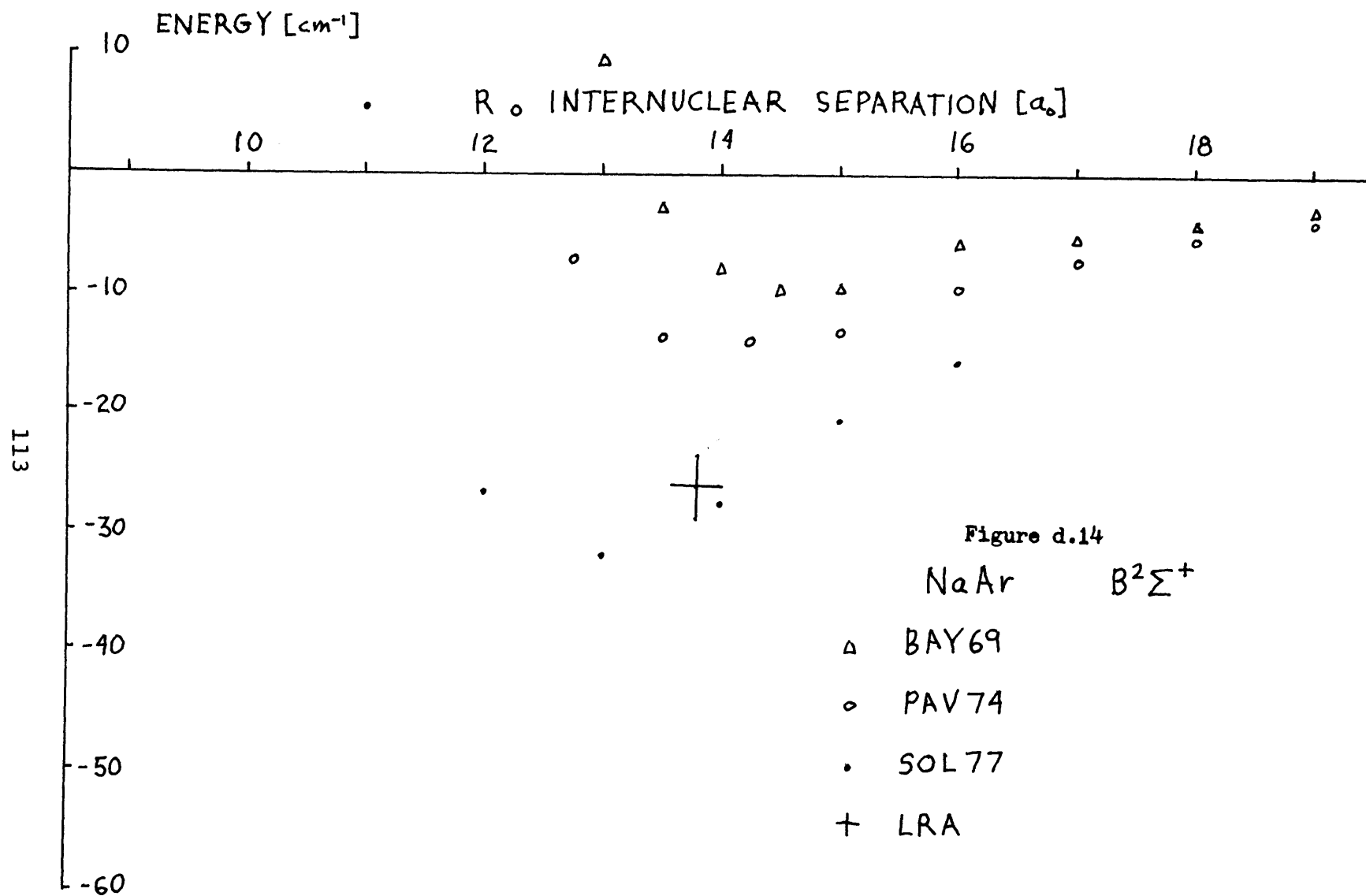
CHAPTER V

CONCLUSIONS

The experiments described here and elsewhere (ALP 77, SAF 77) deomonstrate that it is possible to do high resolution, bound-bound spectroscopy on van der Waals molecules (NaNe, NaAr). NaNe is the weakest bound diatomic known, and its study, as well as the NaAr investigations, have led to a convergence of theoretical predictions and empirical determinations of the molecular potentials.

Traditional analysis of the spectra is a convenient way to assign rotational quantum numbers, and deduce unrefined estimates for the molecular constants. It is clear, however, that the Birge Sponer plot cannot accurately predict the excited state well depth to better than 10-15%, and the vibrational dissociation quantum, v_D, to about 25%.

Novel techniques, such as the long range analysis, and computer fitting to a model Hamiltonian greatly improve the accuracy with which molecular constants are determined (<5%). In addition, these techniques furnish an estimate for the van der Waals interaction strength, C_6, which is not forthcoming from a traditional analysis. The long range analysis technique also proves to be a useful tool for

vibrational analysis if isotopic bonds are seen.

Finally, these experiments have yielded _viable_ bounds on both the binding energy and equilibrium separation of the $B^2\Sigma^+$ state in both NaNe and NaAr.

APPENDIX A

CLASSICAL CALCULATION OF THE VAN DER WAALS INTERACTION

A polarizable atom (atomic number Z) placed in an electric field, $\hat{E}$, experiences a charge center separation ($-d\hat{Z}$) producing an induced dipole moment $\hat{p}$ (see Fig.b.1)

$$(A.1) \qquad \hat{p} = \alpha\hat{E} \equiv -Zqd\hat{Z}$$

Here α is the polarizability and q the electronic charge.

If the electric field is not so strong as to ionize the atom, an equilibrium is estabilished such that a restoring force (the nuclear attraction for the electron) balances the effect of the applied field.

$$(A.2) \qquad \hat{F}_{restoring} = \hat{F}_{field}$$

$$-kd\hat{Z} = Zq\hat{E}$$

Here k is the restoring force constant. Eq.(A.2) can be solved for $\hat{E}(k,d)$ which is then substituted into Eq.(A.1) yielding a relation between the polarizability and the restoring force constant.

$$(A.3) \qquad \alpha = \frac{(Zq)^2}{k}$$

The energy of interaction between two atoms (now taken identical for simplicity), whose electrons are assumed to be bound harmonically, can be calculated classically. The electrons have mass m, charge q, resonant frequency ω_0 and experience the force constant, $k = \omega_0^2 m$. The non-interacting system consists of two identical oscillators each with zero point energy $\hbar\omega_0/2$ so the system's total zero point energy is $\hbar\omega_0$. The interaction between oscillators lowers the zero point energy of the system, that is the atoms bond and form a diatomic molecule.

The Lagrangian for the system is

$$(A.4) \qquad L = \frac{1}{2} m(\dot{r}_1^2 + \dot{r}_2^2) - \frac{1}{2} k(r_1^2 + r_2^2)$$

$$- \frac{q^2}{R} \left[1 + \frac{R}{R-r_2+r_1} - \frac{R}{R-r_2} - \frac{R}{R+r_1} \right]$$

where R is the internuclear separation (assumed constant) and r_1 and r_2 are illustrated in Fig.b.2. The interaction term

$$(A.5) \qquad V(R) = \frac{q^2}{R} \left[1 + \frac{R}{R-r_2+r_1} - \frac{R}{R-r_2} - \frac{R}{R+r_1} \right]$$

may be re-arranged to give

(A.6) $V(R) = \dfrac{q^2}{R} \times$

$$\left[1 + \frac{R[R^2+r(r_1-r_2)-r_1r_2]-R(R-r_2+r_1)(2R+r_1-r_2)}{[R^2+R(r_1-r_2)-r_1r_2](R+r_1-r_2)} \right]$$

Since $r_1, r_2 << R$, $r_1-r_2 \approx 0$, and r_1r_2 is also small compared to r_1R, r_2R or R^2, Eq.(A.6) may be written

(A.7) $V(R) \simeq \dfrac{q^2}{R} \left[\dfrac{2r_1r_2}{R^2-r_1r_2} \right]$

which is a small interaction since it is proportional to r_1r_2 (a perturbation approach to this problem may be found in KIT 53). Factoring out an R^2 from the denominator and using a binomial expansion (MAR 70) in the small parameter r_1r_2/R^2 gives

(A.8) $V(R) = \dfrac{q^2}{R^3} \left[-2r_1r_2 + 2 \left[\dfrac{r_1r_2}{R^2} \right]^2 + \dots \right]$

$\simeq - \dfrac{2q^2r_1r_2}{R^3}$

The Lagrangian may now be re-written

(A.9) $L = \dfrac{m}{2}(\dot{r}_1^2+\dot{r}_2^2) - \dfrac{k}{2}(r_1^2+r_2^2) + \dfrac{2q^2r_1r_2}{R^3}$

118

and the equations of motion are easily obtained (MAR 70).

$$(A.10a) \qquad m\ddot{r}_1 + kr_1 - 2q^2r_2/R^3 = 0$$

$$(A.10b) \qquad m\ddot{r}_2 + kr_2 - 2q^2r_1/R^3 = 0$$

These equations are added together, then subtracted to yield two other equations

$$(A.11a) \qquad m\left[\frac{\ddot{r}_1+\ddot{r}_2}{\sqrt{2}}\right] + k\left[\frac{r_1+r_2}{\sqrt{2}}\right] - \frac{2q^2}{R^3}\left[\frac{r_1+r_2}{\sqrt{2}}\right] = 0$$

$$(A.11b) \qquad m\left[\frac{\ddot{r}_1-\ddot{r}_2}{\sqrt{2}}\right] + k\left[\frac{r_1-r_2}{\sqrt{2}}\right] + \frac{2q^2}{R^3}\left[\frac{r_1-r_2}{\sqrt{2}}\right] = 0$$

An appropriate change of variables,

$$(A.12a) \qquad \psi_s = (r_1+r_2)/\sqrt{2}$$

$$(A.12b) \qquad \psi_a = (r_1-r^2)/\sqrt{2}$$

yields familiar harmonic oscillator equations with frequencies

$$(A.13) \qquad \omega_{a,s} = \left\{\frac{k}{m}\left[1\pm\frac{2q^2}{kR^3}\right]\right\}^{1/2}$$

119

$$\simeq \omega_0 \left[1 \pm \frac{2q^2}{kR^3} \right]^{1/2}$$

where a(s) goes with the +(-) sign. Again using the binomial expansion the frequency becomes

$$(A.14) \qquad \omega_{a,s} \simeq \omega_0 \left[1 \pm \frac{q^2}{kR^3} - \frac{1}{8} \left[\frac{2q^2}{kR^3} \right]^2 + \dots \right]$$

Now the zero point energy of the system with the interaction is $\hbar(\omega_a + \omega_s)/2$. The difference between this and $h\omega_0$ is the energy of interaction.

$$(A.15) \qquad \Delta V = \frac{\hbar}{2}(\omega_a + \omega_s) - \hbar\omega_0$$

$$= -\frac{\hbar\omega_0}{2} \left[\frac{q^2}{kR^3} \right]^2$$

Finally using equation (A.3) with Z = 1 the potential energy of interaction is

$$(A.16) \qquad \Delta V = - \left[\frac{\alpha}{R^3} \right]^2 \frac{\hbar\omega_0}{2}$$

This is an attractive potential varying as R^{-6}, a characteristic of van der Waals potentials.

The simple calculation presented here is intended to provide a physical "feel" for the van der Waals interaction.

120

With some difficulty the calculations could be extended to
the case of non-identical ($\omega_1 \neq \omega_2$) oscillators. No new phys-
ics is introduced in this calculation and therefore it is
omitted. The result, however, may be anticipated.

(A.17) $$\Delta V \sim -\frac{\alpha_1 \alpha_2}{R^6} \frac{\hbar}{4}(\omega_1 + \omega_2)$$

APPENDIX B

MOLECULAR HAMILTONIAN

The molecular Hamiltonian for a diatomic molecule within the context of the Born Oppenheimer approximation may be written (HOU 70, FIE 76)

$$(B.1) \qquad H = H_{ev} + H_r + H_{s.o}$$

Where H_{ev} is the electronic-vibrational part containing the electronic energy, E_Λ, and the interatomic potential energy, $V(R)$ (R is the internuclear separation taken along the Z axis). The spin orbit part, $H_{s.o.}$, can be written (for $\Delta S = 0$),

$$(B.2) \qquad H_{s.o} = A\vec{L}\cdot\vec{S} = A[L_z S_z + \frac{1}{2}(L_+ S_- + L_- S_+)]$$

where A is the spin orbit radial integral, $\vec{L}$ and $\vec{S}$ represent electronic and spin angular momentum respectively. L_+, etc, are the familiar ladder operation, $L_\pm = L_x \pm iL_y$. Finally, the rotational part H_r may be written

$$(B.3) \qquad H_r = B\left\{(J^2 - J_z^2) + (L^2 - L_z^2) + (S^2 - S_z^2)\right.$$

$$+ L_+S_- + L_-S_+ - J_+L_- - J_-L_+ - J_+S_- - J_-S_+ \Big\}$$

where $\vec{J}$ is the total angular momentum, and the term $B(L^2-L_z^2) = BL^2$ is extracted from H_r and lumped into, H_{eV}. B is the rotational constant, $B = h/8\pi^2 c\mu R^2$, where μ is the molecular reduced mass.

The matrix elements are computed using a case (a) basis set, $|v\rangle|\Lambda S\Sigma\rangle|\Omega JM\rangle$, where v indicates the vibrational quantum number; Λ,Σ,Ω are projections of the electronic, spin and total angular momenta onto the internculear axis R; and M is the projection of $\vec{J}$ along some laboratory fixed axis. The basis functions used are states of definite parity (with respect to a reflection in a plane containing the molecule $-\sigma_v$ is the parity operator). The states are designated e(f) partity if $\sigma_v\psi = \pm(-1)^{J-0.5}\psi$, for half integral spins. The basis functions are abbreviated $|^2\Sigma^+\rangle$, $|^2\Pi_{1/2}\rangle$, $|^2\Pi_{3/2}\rangle$ where for example $|^2\Pi_{3/2}{}^e_f\rangle = 1/\sqrt{2} \; [|^2\Pi_{3/2}\rangle \pm |^2\Pi_{-3/2}\rangle]$, the +(-) sign going with e(f) levels. The vibrational quanta have been surpressed for brevity.

The matrix elements are presented in Table B.I. Some second order corrections, notably centrifugal distortion and Λ doubling have been included.

A calculation of one of the off diagonal elements tabulated proceeds as follows:

TABLE B.I. Matrix elements of H. Upper (lower) signs refere to e(f) parity levels (see text).

$$\langle ^2\Sigma^+|H|^2\Sigma^+\rangle = E_\Sigma + G_\Sigma(v'') + B_\Sigma x(x \mp 1) - D_\Sigma x^2(x \mp 1)^2 - (\gamma_\Sigma/2)(1 \mp x)$$

$$\langle ^2\Pi_{1/2}|H|^2\Pi_{1/2}\rangle = E_\Pi + G_\Pi(v') + B_\Pi x^2 - A_\Pi/2 - D_\Pi(x^4 + x^2 - 1) + (p_\Pi/2)(1 \mp x) + (q_\Pi/2)(1 \mp x)^2$$

$$\langle ^2\Pi_{3/2}|H|^2\Pi_{3/2}\rangle = E_\Pi + G_\Pi(v') + B_\Pi(x^2 - 2) + A_\Pi/2 - D_\Pi(x^4 - 3x^2 + 3) + (q_\Pi/2)(x^2 - 1)$$

$$\langle ^2\Sigma^+|H|^2\Pi_{1/2}\rangle = \xi + 2\eta(1 \mp x)$$

$$\langle ^2\Sigma^+|H|^2\Pi_{3/2}\rangle = -2\eta(x^2 - 1)^{1/2}$$

$$\langle ^2\Pi_{1/2}|H|^2\Pi_{3/2}\rangle = -B_\Pi(x^2-1)^{1/2} + 2D_\Pi(x^2-1)^{3/2} - \left[\frac{p_\Pi}{4}\right](x^2-1)^{1/2} - \left[\frac{q_\Pi}{2}\right](x^2-1)(1 \mp x)$$

where; $G_\Lambda(v)$ = vibrational energy of state, v

$x = J + 1/2$

$\eta = 1/2\langle\Pi|BL_+|\Sigma\rangle$

$\xi = 1/2\langle\Pi|AL_+|\Sigma\rangle$

A_Π = spin orbit constant

B_Π = rotational constant

γ_Σ = spin rotation constant (small)

D = centrifugal distortion constant

p = Λ-doubling constant

q = Λ-doubling constant

(B.4) $\langle {}^2\Sigma^+_f e|H|{}^2\Pi_{1/2f}e\rangle = \langle {}^2\Sigma^+_f e|H_{ev}|{}^2\Pi_{1/2f}e\rangle$

$+ \langle {}^2\Sigma^+_f e|H_r|{}^2\Pi_{1/2f}e\rangle + \langle {}^2\Sigma^+_f e|H_{s.o}|{}^2\Pi_{1/2f}e\rangle$

$\langle {}^2\Sigma^+|H_{ev}|{}^2\Pi_{1/2}\rangle = 0$, as the operator H_{ev} has only diagonal matrix elements. Similarly, $L_z S_z$ has only diagonal elements, so

(B.5) $\langle {}^2\Sigma^+_f e|H_{s.o}|{}^2\Pi_{1/2f}e\rangle$

$= \frac{1}{4}\langle[\langle {}^2\Sigma^+_{1/2}| \pm \langle {}^2\Sigma^+_{-1/2}|]|A(L_+S_- + L_-S_+)$

$|[|{}^2\Pi_{1/2}\rangle \pm |{}^2\Pi_{-1/2}\rangle]\rangle$

This caluclation involves eight matrix elements most of which are zero. For example,

$\langle {}^2\Sigma^+_{1/2}| A L_+S_-|{}^2\Pi_{1/2}\rangle = \langle {}^2\Sigma^+_{-1/2}|A L_+S_-|{}^2\Pi_{1/2}\rangle = 0$

because $|{}^2\Pi_{1/2}\rangle$ has $\Lambda = + 1$, $\Sigma = - 1/2$ and the ladder operator $S_-(L_+)$ cannot lower Σ (or raise Λ) further for a doublet state, so $S_-|{}^2\Pi_{1/2}\rangle = 0$. $\langle {}^2\Sigma^+_{1/2}|AL_+S_-|{}^2\Pi_{-1/2}\rangle = 0$, because the $L_+S_-|{}^2\Pi_{-1/2}\rangle$ gives $|{}^2\Sigma^+_{-1/2}\rangle$. Finally,

125

$$\langle {}^2\Sigma^+_{-1/2} | AL_+S_- | {}^2\Pi_{-1/2} \rangle \equiv \langle \Sigma | AL_+ | \Pi \rangle \equiv 2\xi$$

which cannot be evaluated further by analytical methods because L is not a good quantum number.

The second operator in Eq.(B.5) is calculated in a similar fashion.

$$\langle {}^2\Sigma^+_{1/2} | AL_-S_+ | {}^2\Pi_{-1/2} \rangle = \langle {}^2\Sigma^+_{-1/2} | AL_-S_+ | {}^2\Pi_{-1/2} \rangle = \emptyset$$

because S_+ cannot raise $\Sigma = 1/2$ for doublet states.

$$\langle {}^2\Sigma^+_{-1/2} | AL_-S_+ | {}^2\Pi_{1/2} \rangle = \emptyset \quad \text{since}$$

$$L_-S_+ | {}^2\Pi_{1/2} \rangle \text{ gives } | {}^2\Sigma_{1/2} \rangle. \quad \text{Again,}$$

$$\langle {}^2\Sigma^+_{1/2} | AL_-S_+ | {}^2\Pi_{1/2} \rangle = \langle \Sigma | AL_- | \Pi \rangle = \langle \Pi | AL_+ | \Sigma \rangle = 2\xi$$

The rotational part is calculaated first by noting that terms in Eq.(B.3) like $(J^2 - J_z^2)$ have only diagonal elements. Hence

$$(B.6) \quad \langle {}^2\Sigma^+_{1/2f} {}^e | H_r | {}^2\Pi_{1/2f} {}^e \rangle = \langle {}^2\Sigma^+_{1/2f} {}^e | B \left\{ (L_+S_- + L_-S_+) \right.$$

$$\left. - (J_+L_- - J_-L_+) - (J_+S_- + J_-S_+) \right\} | {}^2\Pi_{1/2f} {}^e \rangle$$

126

Again, using arguments similar to those for the $\langle H_{s.o}\rangle$ calculation, most of these matrix elements are zero. The non-vanishing elements are from the $L_\pm S_\mp$ operators;

$$\langle {}^2\Sigma_{1/2}|BL_-S_+|{}^2\Pi_{1/2}\rangle = \langle \Sigma|BL_-|\Pi\rangle = \eta$$

$$\langle {}^2\Sigma_{-1/2}|BL_+S_-|{}^2\Pi_{-1/2}\rangle = \langle \Sigma|BL_+|\Pi\rangle = \langle \Pi|BL_-|\Sigma\rangle = \eta$$

and from the $J_\pm L_\mp$ operators

$$\langle {}^2\Sigma_{-1/2}|BJ_+L_-|{}^2\Pi_{+1/2}\rangle = \mp \langle \Sigma|BL_-|\Pi\rangle (J+\tfrac{1}{2}) = \mp \eta x$$

$$\langle {}^2\Sigma_{+1/2}|BJ_-L_+|{}^2\Pi_{-1/2}\rangle = \mp \langle \Sigma|BL_+|\Pi\rangle (J+\tfrac{1}{2}) = \mp \eta x$$

where $x = J + 1/2$. The J dependence arises from the factorization of the basis states, viz. $|v\rangle|\Lambda S\Sigma\rangle|\Omega JM\rangle$, so that $\langle \Omega+1,JM|J_\pm|\Omega JM\rangle = [(J\pm\Omega)(J\mp\Omega+1)]^{1/2} = (J+1/2)$. For the two elements considered, $\Omega = 1/2$ and $-1/2$ respectively. The elements $\langle {}^2\Sigma_f^e|BJ_\pm S_\mp|{}^2\Pi_{1/2f}^e\rangle = 0$ because $J_\pm S_\mp$ decreases Ω and Σ by 1, hence the operator only connects states with the same Λ.

Combining these results, we obtain,

(B.7) $$\langle {}^2\Sigma_{1/2f}^e|H|{}^2\Pi_{1/2f}^e\rangle = \tfrac{1}{4}\,[4\xi] \mp 2\eta x + 2\eta = \xi + 2\eta(1\mp x)$$

The other matrix elements listed in Table B.I are calculated
in a similar way. Higher order corrections (centrifugal
distortion, Λ-doubling) have been calculated using second
order perturbation theory (FIE 76).

The deperturbation analysis consists of fitting the
data to the Hamiltonian constructed from the matrix elements
in Table B.I. Initial values for some constants are
obtained from the rotational analysis of the spectrum. The
computer program numerically diagonalizes the Hamiltonian
and varies the initial parameters (and others for which
guesses are not available) until the computer generated
spectrum matches the input (i.e. observed spectral lines).
A match of fit is considered good when the deviation between
observed and calculated lines is random and not greater than
the experimental error. The output consists of a list of
parameters (B's, D's, etc.) which best reproduces the data.

A complete discussion of deperturbation of diatomic
spectra, as well as documentation of the computer programs
used has been given by Gottscho (GOT 79).

APPENDIX C

SCHEMATIC DIAGRAM OF DIODE PUMP

(FREQUENCY TO VOLTAGE CONVERTER)

INPUT

POS

NEG

100 Ω

V+

741

OFFSET

12 K

OFFSET ADJ.

V-

500 K

GAIN MULTIPLIER

MIXER

OUTPUT

MARKER INPUT

GAIN   Hz/mV

5K

10^4 10^3

10^2

500K

10K

0.5   0.2   0.1   0.005   0.02   TIME   CONSTANT
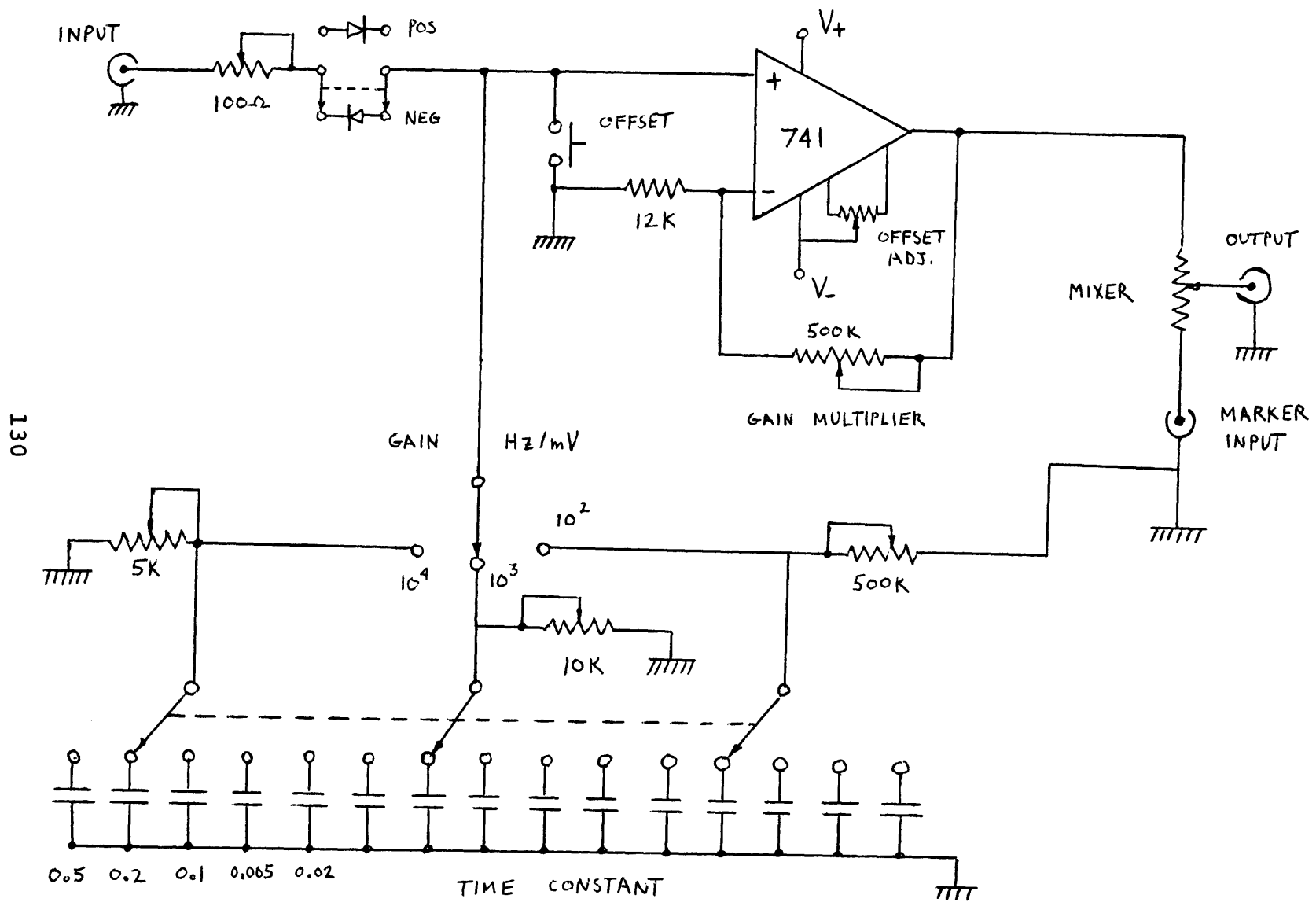
130

APPENDIX D

INITIAL INVESTIGATION OF NaNe

Laser Spectroscopy of Bound NaNe Molecules

Riad Ahmad-Bitar,[a] Walter P. Lapatovich, and David E. Pritchard

Physics Department and Research Laboratory of Electronics, Massachusetts Institute of Technology,
Cambridge, Massachusetts 02139

and

Ingemar Renhorn

Chemistry Department, Massachusetts Institute of Technology, Cambridge, Massachusetts 02139

(Received 26 July 1977)

We have produced the van der Waals molecule NaNe in a supersonic expansion, and have studied the $A^2\Pi \leftarrow X^2\Sigma$ transition using a single-mode cw dye laser. Using analysis based on isotope shifts and the long-range R^{-6} behavior of the excited-state $A^2\Pi$ potential, we find its well depth and location to be $D_{eA} = 140 \pm 3$ cm^{-1} at $r_{eA} = (5.1 \pm 0.1)a_0$ and for the $X^2\Sigma$ ground state, $D_{eX} = 8.1 \pm 0.9$ cm^{-1} at $r_{eX} = (10.0 \pm 0.2)a_0$. These results are compared with pseudopotential calculations and several recent line-broadening and collisions experiments.

We report here the formation of the molecule NaNe in a supersonic molecular beam and the sub-Doppler spectroscopic study of its $A^2\Pi - X^2\Sigma$ transitions using a tunable single-mode cw dye laser. The spectra have been analyzed to yield values for the well depth and location of the $X^2\Sigma$ and $A^2\Pi$ molecular potentials.

The interatomic potentials of NaNe—particularly the $A^2\Pi$ states—have been the subjects of several recent and contradictory theoretical investigations.[1-4] They are relevant to experiments involving scattering of Na in the $3p$ state from Ne,[5-8] and also to the determination of the perturbed line shape of the Na resonance radiation (the D lines) in Ne buffer gas.[9,10] While all of the above experiments have been compared with calculations based on the theoretical potentials (or else have been used to deduce these potentials) no definitive test of the theoretical potentials has yet been possible, partly because of questions concerning the methods used to interpret the experiments.[11,12] Because high-resolution diatomic molecular spectroscopy is the definitive method for determining the bound part of molecular potentials, the present experiment is a major step in cutting the preceding dilemma into two independent problems of manageable proportions: Are the theoretical potentials correct? Are the theories used to deduce potentials in the collision and line-broadening experiments adequate?

The present work also represents a major advance in the spectroscopy of weakly bound diatomic molecules. It is, to begin, by far the most weakly bound molecule studied with high-resolution spectroscopy—the dissociation energy of the $X^2\Sigma$ ground state of NaNe is 5.2 ± 0.8 cm^{-1} (~ 7 K

or <1 meV). Even NaAr, which was recently studied by Smalley et al.,[13] is bound almost an order of magnitude more strongly. Furthermore, this study shows evidence of electronic predissociation in the upper $A^2\Pi_{1/2}$ and $A^2\Pi_{3/2}$ substates belonging to different vibrational levels, and striking intensity anomalies which indicate passage from Hund's case (a) to a more atomlike coupling scheme for the highest vibrational levels of the excited state. None of this structure has been reported in NaAr.[13]

The supersonic beam used to produce NaNe for this study follows the philosophy of Campargue,[14] who demonstrated that Mach numbers (speed ratios) > 100—and therefore temperatures < 1 K—can be produced in systems with moderate pumping speeds by using pressures of ~ 100 atm behind the nozzle. In our experiment a 70%-30% neon-helium gas mixture is introduced into a sodium-containing oven at ~ 100 atm, and ~ 0.1 Torr of Na is mixed in by heating it to (300–400)°C. The vacuum system and light-baffling system is similar to the one used by Smalley, Wharton, and Levy in their study of HeI$_2$.[15]

The molecular beam was probed at right angles with a well-baffled laser beam generated by a Spectra Physics Model No. 580 tunable cw dye laser whose etalon was locked to the cavity as described earlier.[7] Laser-induced transitions from the bound ground state of the molecules (both Na$_2$ and NaNe) to higher bound levels produced fluorescence which was detected by a cooled photomultiplier. Typically 10 mW of laser power was focused approximately 5 mm from the oven. The principal background in the experiment arose from near-resonant scattering from Na in the

1657

beam; stray scattered light was ≤ 200 Hz.

As the dye laser is swept in frequency, the frequency of the laser is established by passing a portion of the laser beam through two air-spaced Fabry-Perot etalons with free spectral ranges of 0.5254 cm^{-1} and 0.063 cm^{-1} (as determined from the separation of the D lines of sodium). The transmitted light is detected and electronically processed to record frequency reference marks simultaneously with the fluorescence spectrum. These marks permit determination of any observed spectral feature to ± 0.002 cm^{-1} relative to the atomic Na D lines.

The molecular spectrum which is detected in the domain from 16 930 to 16 975 cm^{-1} is a mixture of both $A^2\Pi - X^2\Sigma$ of NaNe and $A^1\Sigma_u - X^1\Sigma_g$ of Na$_2$ in addition to the D lines. The NaNe lines are distinguished from the rest by their doublet hyperfine structure[13] and because increases in neon pressure suppress nearly all of the Na$_2$ lines while dramatically enhancing the strength of NaNe lines. The entire NaNe spectrum consisted of about 380 hyperfine doublets with intensities from 4×10^5 to 2×10^3 photons/sec. (Roughly 20% of the doublets had one component overlapped by other lines.)

A $\Pi - \Sigma$ molecular transition has the selection rule for the total angular momentum, $\Delta J = -1$, $0, +1$ (the P, Q, R branches, respectively). The effect of the electron spin in the $^2\Pi - {}^2\Sigma$ transition in NaNe is different for the upper and lower states: The $^2\Pi$ is Hund's case (a) and is separated into $^2\Pi_{3/2}$ and $^2\Pi_{1/2}$, whereas the $^2\Sigma$ is Hund's case (b) and each j level is split into two components, as is each of the P, Q, and R branches (now denoted by P_1, P_{12}, etc.).[16] In our data we observed at most four branches in any band, the
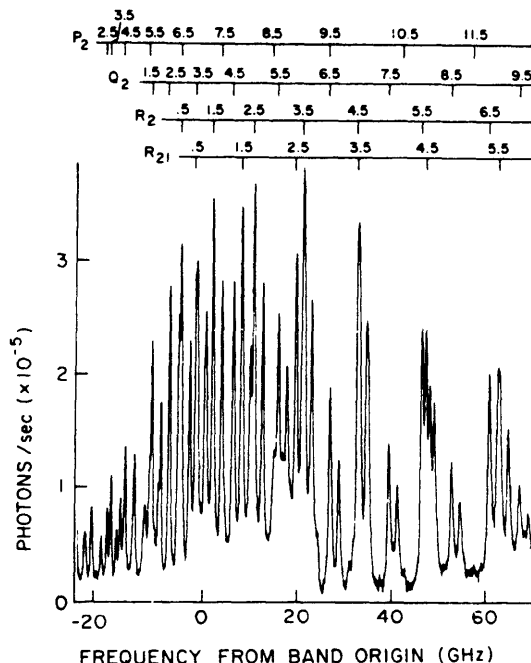

FIG. 1. The $A^2\Pi_{3/2}(v = 5) \leftarrow X^2\Sigma^+ (v = 0)$, measured from the band origin at 16 967.32 cm^{-1}. The weak lines at the low side of the bandhead are from ^{23}Na^{22}Ne. The branch and the quantum number J of the lower level are shown over each identified line.

P_1 and Q_1 branches being degenerate with the Q_{12} and R_{12} branches because of the absence of significant spin-rotational interaction in the $X\Sigma$ state. Figure 1 shows an assignment of one such band made using standard techniques.[16] The observed eigenvalues were least-squares fitted using the appropriate rotational eigenvalue equations.[13,17] Table I shows the resulting constants; they reproduce the data to within ± 0.003 cm^{-1} except near

TABLE I. Long-range fits to band origins and rotational constants of $A^2\Pi_{3/2}$ using Eqs. (9) and (33) in Ref. 18. The 5* is for ^{23}Na^{22}Ne; appropriate fits were obtained using formulas in Ref. 19. The band origins are measured from $3^2S_{1/2} \rightarrow 3^2P_{3/2}$ of Na and all units are cm^{-1}. The rotational energy is given by $B_v J(J + 1) + D_v [J(J + 1)]^2$.

v	Band origin	Fit	Splitting from $A^2\Pi_{1/2}$	$B_v \times 10^5$	Fit	$D_v \times 10^8$
3	-31.64	-31.68	11.86	13 068	13 067	5684
4	-16.31	-16.32	11.81	10 480	10 649	4605
5*	-7.14	-7.07	$\Pi_{1/2}$ not seen	07 939	07 916	5711
5	-6.06	-6.06	12.8(1)	08 230	08 231	6325
6	0.31	0.28	15.02	05 826	05 829	6652
v_D	$\cdots$	5.23	$\cdots$	$\cdots$	∞	$\cdots$
$-1/2$	$\cdots$	-143.0	$\cdots$	$\cdots$	21 530	$\cdots$

perturbations. These constants are effective constants for the $^2\Pi_{3/2}$ component. A more accurate nonlinear least-square fit including self-perturbation and interaction with $B^2\Sigma$ is in progress.

In all, nine bands were analyzed in this manner. We observed transitions only from the $v'' = 0$ level of the $X^2\Sigma$ ground state (which should have a bound $v'' = 1$ level). Two weak bands slightly to the red of similar strong bands were identified as $^{23}Na^{22}Ne$ (neon contains 9% ^{22}Ne) by their position and rotational constants. A band which we identify as $B^2\Sigma - X^2\Sigma$ was observed whose origin was 2.82 cm^{-1} above the $3^2P_{3/2}$ transition in Na. It has small rotational constant $B = 0.018$ cm^{-1} and prominent P and R branches. The $v' = 6$ band of $^2\Pi_{1/2}$ had only P_1 and R_1 branches. We attribute these intensity anomalies (a weak extra branch in the $B^2\Sigma$ band and the missing branches in the $^2\Pi_{1/2}$) to interaction of the two states caused by spin-orbit coupling in Na. This may indicate the use of a more atomic basis for these levels [e.g., Hund's case (e)[16]].

The recently developed methods of long-range analysis[18&19] extracted more information from our data than analysis based on the traditional Dunham expansion.[16] For NaNe, in which the interatomic potential varies as R^{-6} at large internuclear separation, this analysis predicts that both the rotational constant $B_{v'}$ and the quantity $[G(v_D') - G(v')]^{1/3}$ [where $G(v_D')$ is the dissociation limit] should decrease linearly with v', reaching 0 at v_D'.[18] Long-range analysis also permitted comparison of our data for the two isotopes, yielding the fits and absolute numbering for v' shown in Table I, as well as the dissociation limit $G(v_D')$.

The long-range expressions for $B_{v'}$ and $G(v')$ provide means for determining the well depths and locations of the $A^2\Pi$ and $X^2\Sigma$ potentials. The dissociation energy of the $^2\Pi_{3/2}$ state, $G(v_D')$, is measured with reference to the $v'' = 0$ level of the $^2\Sigma$ ground-state potential. After subtraction of the atomic transition energy of Na (done in Table I) it equals the binding energy of this $v'' = 0$ level, $D_{0X} = 5.2 \pm 0.9$ cm^{-1}. [The uncertainty reflects the departure from linearity of similar analyses of computer-generated eigenvalues, $G(v')$, for plausible potential forms.] The measured ground-state rotational constant $B_{0X} = 0.0489$ cm^{-1} and its distortion constant $D_{v''=0} = 3 \times 10^{-5}$ cm^{-1} were reproduced, along with D_{0X}, using a Morse potential whose depth was $D_{eX} = 8.1(9)$ cm^{-1} located at $r_{eX} = (10.0 \pm 0.2)a_0$. This potential had a vibrational constant $\omega_{eX} = 6.2(3)$ cm^{-1}, consistent with the observed isotope shift in D_{0X} of 0.064(16) cm^{-1}.

Finally, an extrapolation of $G(v')$ to $v' = -\frac{1}{2}$ yields an estimate of the well depth of the $A^2\Pi_{3/2}$ potential, $D_{eA} = 140 \pm 3$ cm^{-1}, and its location can be determined from the extrapolated $B_{v'}$, $r_{eA} = (5.1 \pm 0.1)a_0$.

The X-state parameters found from earlier scattering data from our lab[8] are in reasonable accord with this more definitive work. D_{eX} agrees within error, and the small discrepancy in r_{eX} probably reflects the departure of the true potential from the Morse-spline van der Waals shape assumed in Ref. 8. The excited-state well depth determined from the scattering agrees with the result reported here but r_{eA} definitely does not. We feel that this discrepancy most probably arises from failure of the elastic approximation used in the scattering analysis. Although Saxon, Olson, and Liu[20] have shown that this approximation works well for the $A^2\Pi$ state of NaAr (with $D_{eA} \approx 500$ cm^{-1}), Reid[12] has shown that it fails miserably for NaHe (using $D_{eA} = 38$ cm^{-1}). Apparently NaNe is an intermediate case; close-coupling calculations using the potential parameters proposed here would be valuable, and might also resolve discrepancies in the velocity dependence of Na-Ne fine-structure-state—changing collisions.[7,8]

Our results show that the recent pseudopotential calculations of Malvern and Peach[4] are much better able to predict the excited-state interaction potential for NaNe than earlier pseudopotential calculations[1-3] (see Table II).

The present experiment calls into question the ability of spectral line-shape data to yield useful information on interatomic potentials for weakly bound systems. The conclusion of Lwin, McCartan, and Lewis[21] based on line shifts and broadening that the NaNe potentials are more repulsive than those calculated by Baylis[1] or Pascale and Vandeplanque[2] is incorrect and the con-

TABLE II. Depth and location of minima for $A^2\Pi_{3/2}$ and $X^2\Sigma^+$ potential curves of NaNe.

Method	$X^2\Sigma^+$		$A^2\Pi_{3/2}$	
	D_e (cm^{-1})	r_e (a_0)	D_e (cm^{-1})	r_e (a_0)
Ref. 1	1.8	12.9	13.7	8.5
Ref. 2	1.8	13.13(12)	6.2	9.00
Ref. 3	< 40	> 9.45		
Ref. 4	17.8	10	89.5	6.0
This work	8.1 ± 1	10.0 ± 0.2	140 ± 3	5.1 ± 0.1
Scattering	11^{+3}_{-4}	9.1 ± 0.4	120 ± 15	8.0 ± 0.3

clusion of McCartan and Farr[10] that the $B^2\Sigma$ well depth is 0.5 cm^{-1} is inconsistent with our observation of a level bound by 2.4±0.8 cm^{-1} in the $B^2\Sigma$ potential. The failure of York, Scheps, and Gallagher[9] to observe a pressure dependence of the far red wing fluorescence of Na-Ne suggests to us that their lowest pressure (40 Torr) was not low enough to avoid three-body collisions which formed bound NaNe*. This implies that the systems NaHe, LiNe, and LiHe may also have D_{eA}'s, which are a larger fraction of kT than concluded by Gallagher and co-workers.[9,22] It remains to be seen if more sophisticated theories of line broadening can explain the line shapes observed by the preceding workers using potentials consistent with the findings of this work.

---

[a]Present address: University of Jordan, Physics Department, Amman, Jordan.

[1]W. E. Baylis, J. Chem. Phys. 66, 3778 (1977).

[2]J. Pascale and J. Vandeplanque, J. Chem. Phys. 60, 2278 (1974).

[3]C. Bottcher, A. Dalgarno, and E. L. Wright, Phys. Rev. A 7, 1606 (1973).

[4]R. Malvern and G. Peach, private communication.

[5]J. Pitre and L. Krause, Can. J. Phys. 45, 2671 (1967).

[6]G. M. Carter, D. E. Pritchard, M. Kaplan, and T. W. Ducas, Phys. Rev. Lett. 35, 1144 (1975).

[7]J. Apt and D. E. Pritchard, Phys. Rev. Lett. 37, 91 (1976).

[8]W. D. Phillips, C. L. Glaser, and D. Kleppner, Phys. Rev. Lett. 38, 1018 (1977).

[9]G. York, R. Scheps, and A. Gallagher, J. Chem. Phys. 63, 1052 (1975).

[10]D. G. McCartan and J. M. Farr, J. Phys. B 9, 985 (1976).

[11]R. Bienick, Phys. Rev. A 15, 1513 (1977).

[12]R. H. G. Reid, J. Phys. B 8, L493 (1975).

[13]R. E. Smalley, D. A. Auerbach, P. S. H. Fitch, D. H. Levy, and L. Wharton, J. Chem. Phys. 66, 3778 (1977).

[14]R. Campargue, J. Chem. Phys. 52, 1795 (1970).

[15]R. E. Smalley, D. H. Levy, and L. Wharton, J. Chem. Phys. 64, 3266 (1976), see especially Figs. 2 and 3.

[16]G. Herzberg, Spectra of Diatomic Molecules (Van Nostrand, New York, 1950).

[17]R. Mulliken, Rev. Mod. Phys. 3, 89 (1931).

[18]R. J. LeRoy, Molecular Spectroscopy (The Chemical Society, Burlington House, London, 1973), Vol. 1.

[19]W. C. Stwalley, J. Chem. Phys. 63, 3062 (1975).

[20]R. P. Saxon, R. E. Olson, and B. Liu, to be published.

[21]N. Lwin, D. G. McCartan, and G. L. Lewis, J. Phys. B 9, L161 (1976).

[22]R. Scheps, C. N. Ottinger, G. York, and A. Gallagher, J. Chem. Phys. 63, 2581 (1975).

135

APPENDIX E

ESTIMATE OF VIBRATIONAL TEMPERATURE

The vibrational temperature of NaAr formed in the molecular beam can be estimated from vibrational band intensities.

The absorption of laser light by van der Waals molecules (monitored via fluorescence) may be expressed as

$$(E.1) \qquad I_{v'v''} \propto N_{v''} q^2_{v'v''}$$

where $I_{v'v''}$ is the signal strength, $N_{v''}$ is the ground state population of NaAr in level v'', and $q^2_{v'v''}$ in the Franck Condon factor for a $v'v''$ transition. Franck Condon factors for $A^2\Pi_{3/2}-X^2\Sigma^+$ in NaAr have been calculated using a model potential for the $X^2\Sigma^+$ state (SAF 77, TRK 79) and the RKR potential derived from observed levels in the $A\Pi$ state. These factors are presented in Table E.I.

Assuming a Boltzmann distribution for the population in the ground state, the relative vibrational level populations may be written,

$$(E.2) \qquad N_{v''} = N_o e^{-\Delta E/kT} = N_o e^{-\Delta E/T_v}$$

TABLE E.I.   Franck Condon Factors: NaAr $A^2\Pi_{3/2} \to X^2\Sigma$

v' \\ v''	0	1	2	3	4
0	1.3×10^{-12}	8.2×10^{-12}	2.5×10^{-11}	4.3×10^{-11}	3.9×10^{-11}
1	2.2×10^{-10}	1.3×10^{-9}	3.8×10^{-9}	6.4×10^{-9}	5.7×10^{-9}
2	1.6×10^{-8}	8.9×10^{-8}	2.4×10^{-7}	3.8×10^{-7}	3.3×10^{-7}
3	6.4×10^{-7}	3.2×10^{-6}	8.0×10^{-6}	1.2×10^{-5}	1.0×10^{-5}
4	1.6×10^{-5}	7.0×10^{-5}	1.6×10^{-4}	2.2×10^{-4}	1.7×10^{-4}
5	2.6×10^{-4}	9.4×10^{-4}	1.8×10^{-3}	2.3×10^{-3}	1.7×10^{-3}
6	2.9×10^{-3}	8.1×10^{-3}	1.3×10^{-2}	1.4×10^{-2}	9.3×10^{-3}
7	2.1×10^{-2}	4.2×10^{-2}	5.0×10^{-2}	4.3×10^{-2}	2.5×10^{-2}
8	9.9×10^{-2}	1.2×10^{-1}	8.4×10^{-2}	4.7×10^{-2}	2.0×10^{-2}
9	2.7×10^{-1}	1.1×10^{-1}	2.3×10^{-2}	1.2×10^{-3}	2.1×10^{-4}
10	3.8×10^{-1}	2.7×10^{-5}	3.9×10^{-2}	4.4×10^{-2}	2.4×10^{-2}
11	2.0×10^{-1}	2.6×10^{-1}	7.9×10^{-2}	6.6×10^{-3}	2.0×10^{-5}
12	2.2×10^{-2}	4.0×10^{-1}	8.3×10^{-2}	8.2×10^{-2}	3.1×10^{-2}
13	3.6×10^{-5}	5.6×10^{-1}	5.3×10^{-1}	7.3×10^{-3}	2.4×10^{-2}
14	9.5×10^{-7}	7.1×10^{-4}	9.2×10^{-2}	6.1×10^{-1}	7.9×10^{-3}
15	1.7×10^{-6}	3.7×10^{-5}	2.8×10^{-3}	1.4×10^{-1}	5.6×10^{-1}
16	8.8×10^{-7}	2.2×10^{-6}	4.5×10^{-4}	3.9×10^{-3}	3.0×10^{-1}
17	3.4×10^{-7}	9.0×10^{-8}	9.9×10^{-5}	9.9×10^{-4}	1.4×10^{-5}

where $E = G(v'') - G(0)$ the vibrational energy gap, $k =$ Boltzmann's constant, $N_{v''}$ in the population in level v'', and T is ^{o}K, whereas T_v is temperature in wavenumbers (1.45K = 1 cm^{-1}). Also note,

$$(E.3) \qquad N_o = N_{v''}\ e^{+\ E/T_v}$$

Expressing Eq.(E.2) and (E.3) in terms of intensities via Eq.(E.1), and taking the ratio of a $v'v''$ transition to a $v'0$ transition we have

$$(E.4) \qquad \frac{I_{v'o}}{I_{v'v''}} = \frac{q^2_{v'o}}{q^2_{v'v''}}e^{E/T_v}$$

Finally Eq.(E.4) is solved for T_v and yields,

$$(E.5) \qquad T_v = \frac{G(v'')-G(0)}{n\ \dfrac{I_{v'o}}{I_{v'v''}}\ \dfrac{q^2_{v'v''}}{q^2_{v'o}}}$$

The ratio of the observed integrated intensities for $\pi_{1/2}(7,1)$ and $\pi_{3/2}(10,0)$ is $I_{10,0}/I_{7,1} = 88.73$. Using the tabulated Franck Condon factors, Eq.(E.5), and $\Delta E = 11.25$ cm^{-1} (TRK 79) the vibrational temperature is calculated, $T_v = 7.1(6)K$. The error is the difference between this calculation and one done using Franck Condon factors calculated

by Tellinghuisen et al (TRK 79).

Further, using Eq.(E-4) and the calculated T_v, the expected intensity for $A^2\Pi_{3/2}-X^2\Sigma^+$(13,2) is calculated. The results indicate count rates of 7 x 10^4 per line (R^e branch).

REFERENCES

AAF 64 J. B. Anderson, R. P. Andres, and J. B. Fenn in
        Advances in Atomic and Molecular Physics, Vol.1,
        (Academic Press, N.Y., p.345, 1965).

AAF 66 J. B. Anderson, R.P. Andres, J. B. Fenn, Adv. in
        Chem. Phys. 10, 275 (1966).

AHB 77 R. Ahmad-Bitar, Ph.D. Thesis, M.I.T. Physics Depart-
        ment, (unpublished, 1977).

AHB 79 R. Ahmad-Bitar, private communication.

ALP 77 R. Ahmad-bitar, W. P. Lapatovich, D. E. Pritchard,
        and I. Renhorn Phys. Rev. Lett. 39, 1657 (1977).

ANF 65 J. B. Anderson and J. B. Fenn, Phys. of Fluids 8,
        780 (1965).

BAY 69 W. E. Baylis, Report No. 100, Joint Institute for
        Laboratory Astrophysics, University of Colorado,
        Boulder (1969).

BAY 76 W. E. Baylis, in Progress in Atomic Spectroscopy, W.
        Hanle and H. Kleinpoppen, eds. (Plenum Publishing
        Co., London, 1976).

BEL 80 T. Bergemann and P. F. Liao, J. Chem. Phys. 72, 886
        (1980).

BIH 63 K. Bier and O. Haena, Rarefied Gas Dynamics 1, 261
        (1963).

BPP 71 V. Buck, H. Pauly, D. Post and T. Schleusener,

Rarefied Gas Dynamics $\underline{1}$, C.10-1 (1971).

CAM 66   R. Compargue, Rarefied Gas Dynamics $\underline{2}$, 279 (1966).

COT 73   E. P. Cohen and B. N. Taylor, J. Phys. Chem. Ref.
Data $\underline{2}$, 663 (1973).

COS 35   E. U. Condon and G. H. Shortley, The Theory of
Atomic Spectra, 1970 ed., Cambridge University
Press, Cambridge, U.K. (1935).

CPK 75   G. M. Carter, D. E. Pritchard, M. Kaplan and T. W.
Ducas, Phys. Rev. Lett. $\underline{35}$, 1144 (1975).

CRC 72   CRC Handbook of Chemistry and Physics, Chemical
Rubber Company, 53rd ed. (1972).

DAV 68   W. D. Davison, J. Phys. B. $\underline{1}$, 597 (1968).

DUN 72   T. M. Dunn, in Molecular Spectroscopy: Modern
Research, Vol.1, K. N. Rao and C. W. Mathews, eds.
(Academic Press, N.Y. 1972).

DUG 79   R. Duren, and W. Gröger, Max Planck Institute, Ber-
icht 125, (unpublished, 1978).

EAR 35   Lester T. Earls, Phys. Rev. $\underline{48}$, 423 (1935).

FED 66   J. B. Fenn and J. Deckers, Rarefied Gas Dynamics $\underline{2}$,
497 (1966).

FIE 76   R. W. Field, Course notes for Chemistry 5.76, M.I.T,
unpublished (1976).

FON 61   P. R. Fontana, Phys. Rev. $\underline{123}$, 1865 (1961).

FRF 52   R. A. Frosch and H. M. Foley, Phys. Rev. $\underline{88}$, 1337

(1952)

GAF 74   R. J. Gallagher and J. B. Fenn, J. Chem. Phys. 60,
         3487 (1974).

GIC 69   D. E. Gilbert and S. Y. Ch'en, Phys. Rev. 188, 40
         (1969).

GLP 80   R. A. Gottscho, W. P. Lapatovich, D. E. Pritchard,
         to be published, J. Chem. Phys. 1980.

GOT 79   R. A. Gottscho, Ph.D. Thesis, M.I.T. Department of
         Chemistry, unpublished (1979).

HAR 72   M. D. Harmony, Introduction to Molecular Energies
         and Spectra, (Holt, Rinehart and Winston, N.Y.,
         1972).

HER 50   G. Herzberg, Molecular Spectra and Molecular
         Structure, Vol.1. Spectra of Diatomic Molecules,
         (Van Nostrand, N.Y., 2nd ed. 1950).

HIN 67   W. R. Hindmarsh, Atomic Spectra, (Pergamon Press,
         London, 1967).

HMV 79   J. Haussen, R. McCarroll, and P. Vailron, J. Phys.
         B: Atom. Molec. Phys. 12, 899 (1979).

HOU 70   J. T. Hougen, NBS Monograph #115, N.B.S. Institute
         for Basic Standards, Washington, D. C. (1970).

KIT 53   C. Kittel, Introduction to Solid State Physics, John
         Wiley and Sons, Inc., New York (1953).

KVD 71   J. Korving, A. G. Visser, B. S. Douma, G. W. T'Hooft

and J. J. M. Beenakker, Rarefied Gas Dynamics 1, C.3-1 (1971).

LAG 80 W. P. Lapatovich, R. Ahmad-Bitar, P. E. Moskowitz, I. Renhorn, R. A. Gottscho and D. E. Pritchard, submitted to J. Chem. Phys. (1980).

LEB 70 R. J. LeRoy and R. B. Bernstein, J. Chem. Phys. <u>52</u>, 3869 (<u>1970</u>).

LER 73 R. J. LeRoy, Energy Levels of a Diatomic near Dissociation," in <u>Molecular</u> <u>Spectroscopy</u>, Vol. 1, The Chemical Society, Burlington House, London (1973).

MAK 69 H. Margenau and N. R. Kester, <u>Theory</u> <u>of</u> <u>Intermolecular</u> <u>Forces</u>, 2nd ed., (Peramon Press, Oxford, U.K. 1969).

MAR 59 H. Margenau, P. Fontana, and L. Klein, Phys. Rev. <u>115</u>, 87 (1959).

MAR 70 J. B. Marion, <u>Classical</u> <u>Dynamics</u> <u>of</u> <u>Particles</u> <u>and</u> <u>Systems</u>, 2nd ed., (Academic Press, N.Y. 1970).

MCF 76 D. G McCartan, and J. M. Farr, J. Phys. B.: Atom. Molec. Phys. <u>9</u>, 985 (1976).

MPR 79 F. Masnou-Seeuws, M. Philipe, E. Roueff and A. Spielfiedel, J. Phys. B: Atom. Molec. Phys. <u>12</u>, 4065 (1979)

MPV 78 F. Masnou-Seeuws, M. Philippe, and P. Valiron, Phys. Rev. Lett. <u>41</u>, 395 (1978).

143

NES 63   A. N. Nesmeyanov, <u>Vapor</u> <u>Pressure</u> <u>of</u> <u>the</u> <u>Elements</u>,
         translated from the Russian, (1963).

PAL 77   D. E. Pritchard, R. Ahmad-Bitar, and W. P. Lapato-
         vich, in <u>Laser</u> <u>Spectroscopy</u>, <u>J</u>. <u>L</u>. <u>Hall</u> <u>and</u> <u>J</u>. <u>L</u>.
         <u>Carlsten</u>, <u>eds</u>. (<u>Springer</u> <u>Series</u> <u>in</u> Optical Sci-
         ences, Vol.7) Springer-Verlag, N.Y., Heidelberg,
         1977.

PAT 65   H. Pauly, and J. P. Toennies in <u>Advances</u> <u>in</u> <u>Atomic</u>
         <u>and</u> <u>Molecular</u> <u>Physics</u>, Academic Press. N.Y., 195
         (1965).

PAT 72   R. K. Pathria, <u>Statistical</u> <u>Mechanics</u>, (Pergamon
         Press, Oxford, 1972).

PAU 64   L. Pauling, <u>College</u> <u>Chemistry</u>, (W. H. Freeman, San
         Francisco, 1964).

PAV 74   J. Pascale and J. Vanderplanque, J. Chem. Phys. <u>60</u>,
         2278 (1974).

PRI 78   D. E. Pritchard, <u>Atomic</u> <u>and</u> <u>Molecular</u> <u>Physics</u>,
         M.I.T. course notes (unpublished, 1978).

PRS 77   T. R. Proctor and W. C. Stwalley, J. Chem. Phys.
         <u>66</u>, 2063 (1977).

RSV 71   G. Rotzoll, R. Viard, and K. Schugerl, Rarefied Gas
         Dynamics I, C.13-1 (1971).

SAF 77   R. E. Smalley, D. A. Auerbach, P. S. H. Fitch, D. H.
         Levy, and L. Wharton, J. Chem. Phys. <u>66</u>, 3778

(1977).

SCH 55   L. Schiff, Quantum Mechanics, McGraw Hill, Inc.,
          N.Y. (1955).

SOL 77   R. P. Saxon, R. E. Olson, and B. Liu, J. Chem. Phys.
          67, 2692 (1977).

STE 74   J. I. Steinfeld, Molecules and Radiation (Harper and
          Row, N.Y. 1974).

SWL 75   R. E. Smalley, L. Wharton, and D. H. Levy, J. Chem.
          Phys. 63, 4977 (1975).

TAT 77   K. T. Tang and J. P. Toennies, J. Chem. Phys. 66,
          1496 (1977).

TMB 76   A. C. Tam, G. Moe, B. R. Bulos, W. Happer, Optics
          Commun. 16, 376 (1976).

TOS 55   C. H. Townes and A. L. Schawlow, Microwave
          Spectroscopy, (Dover ed., Dover Publications, N.Y.,
          1975).

TRK 79   J. Tellinghuisen, A. Ragone, M. S. Kim, D. A. Auer-
          bach, R. E. Smalley, L. Wharton, and D. H. Levy, J.
          Chem. Phys. 71, 1283 (1979).

WAP 80   R. Walkup and D. E. Pritchard, to be published.

ACKNOWLEDGEMENTS

had over the years.

BIBLIOGRAPHICAL NOTE

Walter P. Lapatovich was born and raised in Shenandoah, Pennsylvania and graduated Shenandoah Valley High School. He matriculated at M.I.T. in September 1971, and was graduated with an S.B. in Physics in June of 1975. His bachelor's thesis was entitled "Energy Deposition and Electron Density Measurements in High Pressure Electron Beam Excited Rare Gas Plasmas."*

While at M.I.T., Walter worked as distribution manager for the undergraduate engineering journal Tech Engineering News, and served as an associate freshman advisor.

Pursuing a doctrate, Walter continued graduate studies at M.I.T. in the Atomic Physics and Scattering Group. His research was conducted under the auspices of Professor David E. Pritchard in the field of laser spectroscopy of weakly bound molecules. Walter received his Ph.D. in physics in June of 1980.

* E.Zamir, C. W. Werner, W. P. Lapatovich, E. V. George, Applied Phys. Lett. 27, (1975).